

A Study of Transonic Shock-Wave/Boundary-Layer Interactions using Conservative, Skew-Symmetric Finite-Differences

vorgelegt von
Dipl.-Math.
Jens Brouwer
geb. in Hamburg

von der Fakultät V - Verkehrs- und Maschinensysteme
der Technischen Universität Berlin
zur Erlangung des akademischen Grades

Doktor der Naturwissenschaften
- Dr. rer. nat. -

genehmigte Dissertation

Promotionsausschuss:

Vorsitzender: Prof. Dr. Henning Meyer
Gutachter: Prof. Dr. sc. techn. habil. Jörn Sesterhenn
Gutachter: Prof. Sergio Pirozzoli

Tag der wissenschaftlichen Aussprache: 19.10.2015

Berlin 2016

Eidesstattliche Erklärung

Hier mit erkläre ich an Eides statt, dass die vorliegende Arbeit selbstständig verfasst wurde sowie alle genutzten Hilfsmittel und Quellen aufgeführt sind. Die folgende Darstellung des Eigenanteils gemäß §2 Abs. 4. der Promotionsordnung ist zutreffend.

Jens Brouwer

Berlin, 02.04.2015

Darstellung des Eigenanteils an vorveröffentlichten Forschungsergebnissen gemäß §2 Abs. 4. der Promotionsordnung der TU Berlin

Die folgenden Veröffentlichungen enthalten Forschungsergebnisse welche in diese Arbeit einfließen:

- Jens Brouwer, Julius Reiss, and Jörn Sesterhenn. Fully conservative finite-difference schemes of arbitrary order for compressible flow. *AIP Conference Proceedings*, 1479(1):2290–2293, 2012
- Jens Brouwer, Julius Reiss, and Jörn Sesterhenn. Conservative time integrators of arbitrary order for skew-symmetric finite-difference discretizations of compressible flow. *Computers & Fluids*, 100(0):1 – 12, 2014
- Jens Brouwer, Julius Reiss, and Jörn Sesterhenn. Conservative finite differences as an alternative to finite volume for compressible flows. In Jürgen Fuhrmann, Mario Ohlberger, and Christian Rohde, editors, *Finite Volumes for Complex Applications VII-Methods and Theoretical Aspects*, volume 77 of *Springer Proceedings in Mathematics & Statistics*, pages 169–176. Springer International Publishing, 2014

Alle Veröffentlichungen sind in Co-Autorschaft mit

- Prof. Dr. sc. techn. habil Jörn Sesterhenn
- Dr. Julius Reiss

entstanden.

Hiermit erkläre ich, einen substanziellen Beitrag zu Konzept, Inhalt und Methoden dieser Arbeiten geleistet zu haben.

Jens Brouwer

Berlin, 02.04.2015

Zusammenfassung

Stoß/Grenzschicht-Interaktionen sind in vielen wichtigen technischen Anwendungen präsent. Unter bestimmten Bedingungen treten bei diesen komplexen Interaktionen tieffrequente Oszillationen auf, welche negative Auswirkungen auf Leistung und Effizienz haben können. Die Ursache dieser Schwingungen ist nicht vollständig geklärt und die numerische Behandlung dieser Phänomene ist schwierig. Die Hauptmerkmale der Strömung stellen konkurrierende Anforderungen an die verwendeten numerischen Methoden. Die vorliegende Arbeit erweitert eine, auf der schief-symmetrischen Formulierung der Navier-Stokes Gleichungen basierende, Diskretisierung für die Simulation einer Stoß-Grenzschicht Interaktion. Das so entstehende Finite-Differenzen Verfahren ist vollständig konservativ und erreicht beliebige Ordnung in Raum und Zeit.

Mit Hilfe dieses Verfahrens wird eine direkte numerische Simulation einer transsonischen Stoß/Grenzschicht Interaktionen durchgeführt. Verschiedene Varianten der Modalanalyse, die *dynamic mode decomposition* sowie eine Sensitivitätsanalyse, werden benutzt um die dominanten Strukturen der Strömung zu identifizieren und ihren Einfluss auf den Ursprung der Interaktion zu finden. Diese Untersuchungen verfolgen das Ziel, die tieffrequenten Schwingungen des Stoßsystems zu kontrollieren.

Abstract

Shock-wave/boundary-layer interactions (SBLI) are featured in many important engineering applications. Under certain conditions the complex interaction features a low-frequency unsteadiness that is undesirable for performance and stability reasons and whose origins is not completely understood. Numerical treatment of such SBLIs is difficult as the important flow features place competing demands on the applied numerical algorithms. This work uses and expands a new numerical discretization scheme for the study of SBLI that is based on the skew-symmetric formulation of the Navier-Stokes equations. The resulting finite-difference scheme is fully conservative and of arbitrary order in space and time. Using this scheme, a direct numerical simulation of a transonic shock-wave/boundary-layer interaction is performed. Modal analysis, using dynamic mode decomposition and sensitivity analysis, is used to provide insight into the dominant flow structures and their relation to the origin of the transonic SBLI. This is done with the specific aim to find an ansatz for passive control or damping of the low-frequency unsteadiness.

Acknowledgments

First of all, I would like to take this opportunity to thank Prof. Jörn Sesterhenn and Dr. Julius Reiss for giving me the opportunity to work in the fascinating field of fluid mechanics and for continually providing support and encouragement throughout the years of my PhD studies.

I am deeply grateful towards Sergio Pirozzoli and Matteo Bernardini of the University of Rome - La Sapienza. Both for their hospitality during my visits to Rome and for providing (moral) support during key moments of this undertaking.

This work would not be what it is today without my wonderful colleagues at the FG Numerische Fluidodynamik. Thank you Mathias, Julius, Jan, Flavia, Arne and everybody else that joined us here in the Müller-Breslau Straße. Claus Goetz and Stefan Mosler and Mathias Lemke deserve additional thanks for plowing through early versions of this thesis during very busy periods of their own lives. Naturally, I am beholden to my parents, Marina and Peter, for their ongoing and ceaseless support.

Last, but certainly not least,

Thank You Lätizia!

Contents

Introduction	1
I. Conservative Finite-Differences for Compressible Flow	7
1. The Skew-Symmetric Navier-Stokes Equations	9
1.1. Skew-Symmetry and Conservation	11
1.2. Wall-Bounded Flows	11
1.3. The Rankine-Hugoniot Relations	14
2. FD Discretization of the Skew-Symmetric Navier-Stokes Equations	17
2.1. State of the Art	19
2.2. Conservative Discretization in Space	21
2.3. Conservative Discretization in Time	28
2.4. Boundary Treatment	39
2.5. Distorted Grids	44
2.6. Shock Treatment	46
2.7. Parallel Implementation	50
3. Validation of the Method	53
3.1. Conservation Properties	54
3.2. Lax-Liu Shock Test Cases	58
3.3. Isotropic Turbulence	61
3.4. Turbulent Boundary-Layer Flow	69

II. Transonic Shock-Wave/Boundary-Layer Interactions	89
4. Introduction to Shock-Wave/Boundary-Layer Interactions	91
4.1. Description of a Shock-Wave/Boundary-Layer Interaction . . .	91
4.2. Low-Frequency Unsteadiness in SBLI	96
5. Computation of a Transonic SBLI	101
5.1. Setup and Geometry	101
5.2. Results of the Transonic SBLI Simulation	104
5.3. Conclusion	131
6. Modal Analysis of a Transonic SBLI	133
6.1. Introduction to Dynamic Mode Decomposition	135
6.2. Dynamic Mode Decomposition of a Transonic SBLI	139
6.3. Theory of Sensitivity Analysis	156
6.4. Sensitivity Analysis of a Transonic SBLI	166
7. Conclusion and Outlook	177
A. Discrete 3-dimensional Navier-Stokes Equations	181
B. Finite-Difference Schemes with the SBP Property	183
Bibliography	199

List of Figures

1.1. Comparison of laminar and turbulent BL profiles	12
2.1. Parallelization: Domain decomposition	50
2.2. Parallelization: Domain transformation	51
2.3. Parallelization: Scaling	52
3.1. Validation: Accuracy of spatial and temporal discretization	54
3.2. Validation: Change in conserved quantities	55
3.3. Validation: Comparisons in conservation I	56
3.4. Validation: Comparisons in conservation II	58
3.5. Shocks: Domain for Lax-Liu test cases	59
3.6. Shocks: Contourplot for Lax-Liu case 11	60
3.7. Shocks: Contourplot for Lax-Liu case 15	61
3.8. Isotropic turbulence: Decay of kinetic energy on different grids	62
3.9. Isotropic turbulence: Decay of Mach number and kinetic energy	62
3.10. Isotropic turbulence: Time evolution of S_3	63
3.11. Isotropic turbulence: Enstrophy Decay	63
3.12. Isotropic turbulence: Energy spectrum on different grids	64
3.13. Isotropic turbulence: Change in conserved quantities	64
3.14. Forced isotropic turbulence: Anisotropy stress tensor	65
3.15. Forced isotropic turbulence: Energy spectra	65
3.16. Forced isotropic turbulence: Density contours I	68
3.17. Forced isotropic turbulence: Vorticity contours I	68
3.18. Forced isotropic turbulence: Density contours II	69
3.19. Forced isotropic turbulence: Vorticity contours II	69
3.20. TBL: Mean velocity profile - Precursor simulation	76

3.21. TBL: Recycling/Rescaling vs. digital filter	77
3.22. TBL: Mean VanDriest transformed velocity profile	78
3.23. TBL: Mean VanDriest transformed velocity defect	79
3.24. TBL: Diagnostic function $y^+ dU_{VD}^+/dy^+$	80
3.25. TBL: Scaled turbulence intensities	81
3.26. TBL: Evolution of skin friction	82
3.27. TBL: Wall-normal velocity slices	83
3.28. TBL: Wall-normal temperature slices	85
3.29. TBL: Spanwise slices of velocity and density	86
3.30. TBL: Streamwise slices of velocity and density	87
4.1. Schematic view of a weak SBLI	93
4.2. Wall pressure in a weak SBLI	94
4.3. Schlieren visualization of a λ -shock	95
4.4. Schematic view of a strong SBLI	96
4.5. Wall pressure in a strong SBLI	97
5.1. SBLI: Computational domain for the SBLI	103
5.2. SBLI: Mean pressure and Mach number	105
5.3. SBLI: Instantaneous pressure and Mach number	106
5.4. SBLI: Mean streamwise pressure and Mach number profiles	107
5.5. SBLI: Streamwise velocity and turbulence intensity profiles	108
5.6. SBLI: u^+ and u_{rms} at different locations	109
5.7. SBLI: Contours of mean turbulence intensities	110
5.8. SBLI: Streamwise velocity fluctuations at $y^+ \approx 5$	111
5.9. SBLI: Velocity fluctuations on the upstream part of the bump	112
5.10. SBLI: Turbulence intensities on the upstream part of the bump	113
5.11. SBLI: Anisotropy stress tensor	114
5.12. SBLI: Streamwise profile of C_f	115
5.13. SBLI: Streamlines in the recirculation bubble	116
5.14. SBLI: PDF of C_f and probability of detached flow	117
5.15. SBLI: p_w over time	118
5.16. SBLI: $p(y = 0.163B_l)$ over time	119
5.17. SBLI: Contours of premultiplied wall pressure PSD	120
5.18. SBLI: PSD of p_w in the upstream TBL and at the leading shock	120
5.19. SBLI: Contours of premultiplied PSD of $p(y = 0.163B_l)$	122
5.20. SBLI: PSD of $p(y = 0.03)$ at both shocks	122
5.21. SBLI: Welch averaged PSD of pressure	123
5.22. SBLI: Transfer function of the SBLI system	123

5.23. SBLI: Mean pressure contours	125
5.24. SBLI: PSD of autocorrelations within the interaction zone . .	127
5.25. SBLI: PSD of correlations of recirculating bubble detachment	129
5.26. SBLI: Contours of instantaneous pressure fluctuations	130
5.27. SBLI: PSD of autocorrelations of the pressure signal	131
6.1. DMD: Spectrum and modal amplitude I	140
6.2. DMD: Spectrum and modal amplitude II	141
6.3. DMD: Pressure contours of modes M_1 - M_4	143
6.4. DMD: Streamwise velocity contours of mode M_4	144
6.5. DMD: Pressure contours for two vortex shedding modes . . .	145
6.6. DMD: $ p_w ^2$ for different modes	146
6.7. DMD: Reconstruction of leading shock position	148
6.8. DMD: Reconstruction of rear shock position	149
6.9. DMD: Reconstruction of recirculating mass	151
6.10. DMD: Reconstruction of the recirculation bubble I	152
6.11. DMD: Reconstruction of the recirculation bubble II	153
6.12. DMD: Reconstruction of the pressure field I	155
6.13. Sens: Pressure contours of the direct shock-mode	166
6.14. Sens: Velocity contours of the direct shock-mode	167
6.15. Sens: Pressure contours of the adjoint shock-mode	169
6.16. Sens: Velocity contours of the adjoint shock-mode	170
6.17. Sens: Pressure and velocity of the adjoint shock-mode	171
6.18. Sens: Streamwise velocity wavemaker of the shock-mode . . .	172
6.19. Sens: Sensitivity to baseflow modifications of the shock-mode	173

List of Tables

2.1. Computational efficiency of implicit and explicit time integration	39
3.1. Initial conditions for test cases 11 and 15 taken from [49]	59
3.2. Parameters of the TBL simulation at $Re_\delta = 4736$	75
3.3. Parameters of the precursor simulation at $Re_\delta = 3000$	75
3.4. Details on the TBL reference station x_0	78
4.1. Comparison of different SBLI studies	98
5.1. Parameters of the transonic SBLI simulation	102
6.1. Error norm for the DMD reconstruction of the SBLI	147
6.2. Adjoint expressions for receptivity	168

List of Procedures

2.1. Implementation of Boundary Conditions	44
2.2. Conservative Filtering Algorithm	49
3.1. Forcing Algorithm for Isotropic Turbulence	67
3.2. Digital Filter Approach for TBL inflow data	73
6.1. Dynamic Mode Decomposition of a Snaphsot Sequence	137
6.2. Computation of Sensitivity to Baseflow Modifications	165

Introduction

Shock-wave/boundary-layer interactions (SBLI) play an important part in many engineering applications. They are common in internal and external aerodynamic flows. A prime example is the transonic flow over an airfoil. The flow is accelerated over the airfoil and a supersonic pocket forms which is terminated by a shock-wave. The shock implies a sudden, almost discontinuous change in all flow quantities. This imposes large unfavorable loads on the airfoil and increases drag. When the shock is strong enough, a recirculation bubble can form at the impingement point and further complicate the situation. Depending on a number of factors, like Mach number, angle of attack or airfoil shape, the position of the shock begins to oscillate. The onset of this effect, called *buffeting*, has to be prevented in order for regular flight to continue.

While the above example deals with transonic flow over an airfoil, similar situations can happen in fully supersonic flows. Common examples are compression ramps or high-speed turbomachinery intakes. Common for all these SBLIs is the development of low-frequency unsteadiness in the interaction zone whose origin is not completely understood.

In the last decade, supersonic SBLIs in model geometries have been studied intensively in order to find the fundamental ingredients of the interactions. On the other hand, transonic interactions, who are more complex due to the added route of interaction through upstream traveling pressure effects, have not been treated with the same thoroughness.

Besides experimental studies, large eddy and direct numerical simulations of the Navier-Stokes equations are the tool of choice to investigate the complex shock interaction because they rely on no or as little modeling assumptions as possible and yield insight into the whole flow field. However, numerical simulation of turbulent boundary-layer flow containing shocks is very demanding

for the employed algorithms. Generally shocks and small scale turbulence as well as acoustics demand competing qualities from the underlying numerics. The correct treatment of shocks is dependent on the correct representation of conservation properties, which is a natural hallmark of Finite-Volume (FV) schemes, which are based on the integral formulation of the equations of motion. However, most Finite-Volume methods introduce artificial numerical dissipation through upwind discretization and have difficulty separating kinetic from internal energy while still conserving the sum of both. This introduces difficulties when simulating small scale turbulence, where the interplay of energy transfer and dissipation dominates, or sound and pressure propagation, which is characterized by very small fluctuations. When such phenomena are of interest, high-order Finite-Differences (FD) are the natural choice. Such schemes reach high order of accuracy while being computationally efficient and can be build to reproduce the correct dispersion relation of the fluid.

As such, it is unclear what the natural choice of numerical method for the simulation of SBLI is. As computational efficiency is the most pressing demand for highly accurate large-scale simulations, most studies employ FD methods. A way to adapt and improve these methods are the so-called *skew-symmetric* or *energy-preserving* schemes. They are based on the skew-symmetric formulation of the Navier-Stokes equations and feature conservation properties not present in standard finite-differences as well as a correct treatment of the kinetic energy. Previously such schemes existed only of limited order of accuracy in time, restricting their application to large-scale simulations.

Goals and outline of the thesis

Considering these points, the goals of this thesis can be summarized as follows:

1. Construct a conservative, skew-symmetric finite-difference discretization of the Navier-Stokes equations that is:
 - of arbitrary order in space
 - of arbitrary order in time
 - applicable on distorted grids
2. Do a direct numerical simulation of a three-dimensional transonic shock-wave/boundary-layer interaction in order to:

-
- do statistical analysis of the flow and identify the timescales associated with the low-frequency unsteadiness
 - use *dynamic mode decomposition* to identify dominant structures of the low-frequency unsteadiness
 - use methods of modal sensitivity analysis to find an ansatz as to how to prevent the low-frequency unsteadiness

In order to achieve the above goals, this thesis is split into two parts. The first part deals with the construction of a fully conservative finite-difference discretization of the skew-symmetric equations of compressible flow. This part is structured into 3 chapters. First, the Navier-Stokes equations and their skew-symmetric formulation are presented. The second chapter presents the derivation of the fully conservative discretization. After giving an overview of the current state of the art, section 2.2 derives a semi-discretization in space that is easy to implement and can be constructed of arbitrary order of accuracy. In section 2.3 this discretization is modified to allow fully conservative time-integration of arbitrary order. After these fundamental steps, sections 2.4-2.5 explain how the scheme is adapted to include distorted grids and boundary conditions. Section 2.6 adapts a shock-filtering algorithm for the use in the skew-symmetric, conservative framework. Finally, parallel implementation is discussed in 2.7. After the construction of the scheme, chapter 3 is used to validate the method for use in the simulation of compressible, turbulent, boundary-layer flow with shocks. Over the course of the chapter, simulations of inviscid shock test-cases, isotropic turbulence and turbulent boundary-layers are presented.

The second part of this work presents the simulation and analysis of a shock-wave/boundary-layer interaction in transonic, turbulent flow over a bump. This configuration is chosen in order to be able to study the complete transonic interaction without influence from downstream effects not belonging to the interaction itself. Part 2 begins with an overview of the physics of SBLI and the current state-of-the-art of research concerning them. Emphasis is put on the origins of the low-frequency unsteadiness. Chapter 5 details the direct numerical simulation itself. The mean flow field is investigated and statistical methods are employed in order to quantify the low-frequency unsteadiness. Following this conventional analysis, chapter 6 is dedicated to a modal analysis of the transonic SBLI. The snapshot-based *dynamic mode decomposition* will be used to identify the dominant components of the low-frequency oscillations. Afterwards, a classical global stability analysis of the

direct and adjoint flow will be used to derive the sensitivity of the modes associated with the unsteadiness.

Finally, chapter 7, gives an overview of the results of this work and presents possibilities for future work on the subject of transonic SBLIs.

I

Conservative Finite-Differences for Compressible Flow

The Skew-Symmetric Navier-Stokes Equations

Compressible fluid flow is governed by the Navier-Stokes equations which govern the balance of mass, momentum and energy. Written in conservative form the equations are usually expressed in the variables of density, (ρ), velocity, $(u_\alpha)_{\alpha=1,2,3}$, and energy, (E). The system of 5 partial differential equations reads, assuming the summing convention is used:

$$\partial_t \rho + \partial_{x_\alpha} (\rho u_\alpha) = 0, \quad (1.1)$$

$$\partial_t (\rho u_\alpha) + \partial_{x_\beta} (\rho u_\beta u_\alpha) + \partial_{x_\alpha} p = \partial_{x_\beta} \tau_{\alpha\beta}, \quad (1.2)$$

$$\partial_t (\rho E) + \partial_{x_\beta} u_\beta (\rho E + p) = \partial_{x_\alpha} u_\beta \tau_{\alpha\beta} - \partial_{x_\alpha} \Phi_\alpha. \quad (1.3)$$

The pressure is denoted as p , the stress tensor, $\tau_{\alpha\beta}$, rate of strain, $S_{\alpha\beta}$ and heat conduction, Φ_α , are defined as:

$$\tau_{\alpha\beta} = 2\mu S_{\alpha\beta} + \delta_{\alpha\beta} \left(\mu_d - \frac{2}{3}\mu \right) \partial_{x_\gamma} u_\gamma, \quad (1.4)$$

$$S_{\alpha\beta} = \frac{1}{2} \left(\frac{\partial u_\alpha}{\partial x_\beta} + \frac{\partial u_\beta}{\partial x_\alpha} \right), \quad (1.5)$$

$$\Phi_\alpha = -\lambda \partial_{x_\alpha} T. \quad (1.6)$$

Here T is the temperature and μ the molecular viscosity which is modeled by the Sutherland law

$$\mu = \mu_0 \frac{T_0 + S}{T + S} \left(\frac{T}{T_0} \right)^{3/2} \quad (1.7)$$

using the constant $S = 110.4K$. The thermodynamic relation

$$p = \rho RT \quad (1.8)$$

is used to close the system with the specific gas constant $R = 287m^2K^{-1}s^{-2}$. Finally heat conductivity λ is given by Fourier's law as

$$\lambda = \mu \frac{C_p}{Pr} \quad (1.9)$$

with $\gamma = C_p/C_v = 1.4$, $C_p - C_v = R$ and $Pr = 0.71$.

The form of the system of equations above is often called the conservative formulation of the Navier-Stokes equations. This is because an integration over space and time immediately reveals the conservation of mass, momentum and energy when boundary fluxes are neglected. An alternative formulation of the above equations is the so-called *skew-symmetric* form of the equations which can be derived by using the product rule to rewrite the momentum equation and splitting the internal energy,

$$e = \frac{1}{\gamma - 1} \frac{p}{\rho}, \quad (1.10)$$

off from the total energy:

$$E = e + \frac{u_\alpha u_\alpha}{2}. \quad (1.11)$$

One then arrives at:

$$\partial_t \rho + \partial_{x_\alpha} (\rho u_\alpha) = 0, \quad (1.12)$$

$$\frac{1}{2} (\partial_t \rho \cdot + \rho \partial_t \cdot) u_\alpha + \frac{1}{2} (\partial_{x_\beta} \rho u_\beta \cdot + \rho u_\beta \partial_{x_\beta} \cdot) u_\alpha + \partial_{x_\alpha} p = \partial_{x_\beta} \tau_{\alpha\beta}, \quad (1.13)$$

$$\begin{aligned} \frac{1}{\gamma - 1} \partial_t p + \frac{\gamma}{\gamma - 1} \partial_{x_\alpha} (u_\alpha p) - u_\alpha \partial_{x_\alpha} p \\ + u_\alpha \partial_{x_\alpha} \tau_{\alpha\beta} - \partial_{x_\beta} u_i \tau_{\alpha\beta} = -\partial_{x_\alpha} \Phi_\alpha. \end{aligned} \quad (1.14)$$

The equations (1.12)-(1.14) are called *skew-symmetric* because both the temporal differentiation operator and convection term

$$(\phi \partial \cdot + \partial \phi \cdot) \quad (1.15)$$

are skew-symmetric. This can easily be proven by looking at the scalar product $(v, w) = \int_\Omega v w dV$ and integrating by parts:

$$\int_\Omega v (\phi \partial_x \cdot + \partial_x \phi \cdot) w dV = - \int_\Omega w (\phi \partial_x \cdot + \partial_x \phi \cdot) v dV. \quad (1.16)$$

1.1. Skew-Symmetry and Conservation

The skew-symmetry of the Navier-Stokes equations is an important quality. It can be used to derive the conservation of energy by the equations (1.12)-(1.14). In addition it defines the rate of change of kinetic to internal energy. The equation for the temporal evolution of kinetic energy $(\rho u_\alpha u_\alpha)/2$ can be obtained by multiplying the equation of momentum with u and integrating over the whole domain, Ω , and assuming periodic boundaries:

$$\begin{aligned} \partial_t \int_{\Omega} \frac{1}{2} (\rho u_\alpha^2) dV &= - \int_{\Omega} \left(\frac{1}{2} u_\alpha (\rho u_\beta \partial_{x_\beta} \cdot + \partial_{x_\beta} \rho u_\beta \cdot) u_\alpha + u_\alpha \partial_{x_\alpha} p - u_\alpha \partial_{x_\beta} \tau_{\alpha\beta} \right) dV \\ &= - \int_{\Omega} (u_\alpha \partial_{x_\alpha} p - u_\alpha \partial_{x_\beta} \tau_{\alpha\beta}) dV. \end{aligned} \quad (1.17)$$

The convection operator disappears due to its skew-symmetry and thus does not add or destroy kinetic energy which is *only* changed by pressure and friction forces. The change in internal energy, e , is given by the integration of equation (1.14) over the domain:

$$\begin{aligned} \frac{1}{1-\gamma} \partial_t \int_{\Omega} p dV &= \int_{\Omega} - \left(\frac{\gamma}{\gamma-1} \partial_{x_\alpha} (u_\alpha p) - u_\alpha \partial_{x_\alpha} p \right. \\ &\quad \left. + u_\alpha \partial_{x_\alpha} \tau_{\alpha\beta} - \partial_{x_\beta} u_i \tau_{\alpha\beta} + \partial_{x_\alpha} \Phi_\alpha \right) dV \\ &= \int_{\Omega} (u_\alpha \partial_{x_\alpha} p - u_\alpha \partial_{x_\beta} \tau_{\alpha\beta}) dV. \end{aligned} \quad (1.18)$$

Again, fluxes over the boundaries are neglected. Thus the *skew-symmetric* Navier-Stokes equations conserve total energy because the changes in kinetic and internal energy balance. Kinetic energy that is destroyed by pressure and friction is converted into internal energy and vice versa. This property of the equations will be the central point in the structure-preserving discretization of equations (1.12)-(1.14). As will be shown, the skew-symmetric formulation of the equations allows this property to be retained in the discrete case.

1.2. Wall-Bounded Flows

In large parts of the flow, the viscous forces in the Navier-Stokes equations are very weak. In these regions the fluid behaves almost as predicted by the inviscid Euler-equations. In the vicinity of walls the viscosity of the flow is of utmost importance as shear forces increase drastically and a boundary-layer

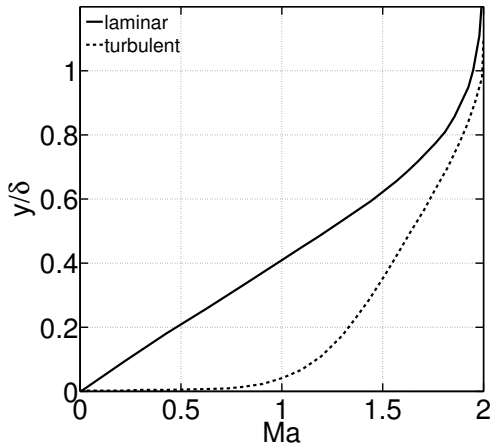


Figure 1.1.: A comparison of a laminar and turbulent mean velocity profile in a flat-plate boundary-layer.

forms. The simplest example being a uniform freestream that flows tangentially to a no-slip wall at which the velocity is fixed to zero. The structure of such a boundary-layer is complex, especially in the turbulent case. Figure 1.1 depicts both a laminar and a turbulent boundary-layer profile for normalized mean velocity. The laminar profile can be obtained from the Orr-Sommerfeld equations, see [97], which although strictly valid only for incompressible flow still is a very good approximation for the compressible profile. No analytical solution for the turbulent profile exists. The turbulent profile is more complex than the laminar one. Especially the very thin near-wall layer is difficult to capture analytically. Its thickness is often less than 0.002δ , where δ is the 99% thickness of the boundary-layer. A description of the turbulent profile is due to Prandtl and Kármán, see e.g. [122]. They postulate that the boundary-layer is made up of three distinct layers: The inner layer, where viscous shear dominates; the outer layer, where turbulent shear dominates and the overlap region where both types of shear are important and a continuous link between the inner and outer layer exists. Prandtl argued that the inner profile depends only on shear stress, fluid properties and distance from the wall, y .

$$u = f(\tau_w, \rho, \mu, y) \tag{1.19}$$

The wall shear stress τ_w being given by

$$\tau_w = \mu \left(\frac{\partial u}{\partial y} \right)_{y=0}. \quad (1.20)$$

For the outer layer Kármán postulated that the wall acts only to reduce the velocity below freestream velocity U_e independent of viscosity but dependent on boundary-layer thickness and pressure gradient in the freestream, this can be written as:

$$U_e - u = F(\tau_w, \rho, y, \delta, \frac{\partial p_e}{\partial x}). \quad (1.21)$$

In the overlap region, both profiles would have to agree. Dimensionality analysis reduces the inner layer profile to

$$\frac{u}{u_\tau} = f\left(\frac{y}{\delta_v}\right), \quad u_\tau = \left(\frac{\tau_w}{\rho}\right)^{1/2}, \quad \delta_v = \frac{\nu}{u_\tau}. \quad (1.22)$$

The quantity u_τ is called the wall-friction velocity and δ_v denotes the viscous length scale. Wall normal distance related to the viscous lengthscale is usually denoted as $y^+ = y/\delta_v$. Similar nondimensionalization of the outer layer profile yields:

$$\frac{U_e - u}{u_\tau} = F\left(\frac{y}{\delta}, \xi\right), \quad \xi = \frac{\delta}{\tau_w} \frac{\partial p_e}{\partial x}. \quad (1.23)$$

Thus the *velocity defect* depends on the local pressure gradient. Given a specific ξ it follows that the identity

$$\frac{u}{u_\tau} = f\left(\frac{\delta u_\tau y}{\nu \delta}\right) = \frac{U_e}{u_\tau} - g\left(\frac{y}{\delta}\right) \quad (1.24)$$

holds in the overlap region. This can only be satisfied if both profiles follow a logarithmic law. Finally one obtains

$$u^+ = \frac{u}{u_\tau} = \frac{1}{k} \ln(y^+) + B, \quad (1.25)$$

$$\frac{U_e - u}{u_\tau} = -\frac{1}{k} \ln\left(\frac{y}{\delta}\right) + A. \quad (1.26)$$

The constants k and B can be experimentally determined as $k \approx 0.41$ and $B \approx 5.2$. The constant A depends on the adverse pressure gradient. In

general, the more adverse the pressure gradient is, the larger A becomes. Looking at the outer profile this implies a thickening of the boundary-layer with an increasing adverse pressure gradient. Once the pressure gradient becomes too large, the boundary-layer will separate and the above profiles lose their validity.

In terms of dimensionless wall distance, y^+ , the *logarithmic region* covers the space $35 < y^+ < 350$. The region of the flow nearest to the wall, where $y^+ < 5$, is called *viscous sublayer*. Here the flow is laminar and almost completely ruled by viscous forces. The velocity profile is linear in the viscous sublayer, i.e. $u^+ = y^+$. In the intermediate region, called *buffer layer*, the profile is a continuous blending of the linear and logarithmic profile.

1.3. The Rankine-Hugoniot Relations

The compressible Navier-Stokes equations admit solutions containing shock-waves and other discontinuities. Their origin is best described through gas dynamics which are governed by the inviscid Euler equations. Shocks are generally defined as surfaces over which flow properties undergo a rapid change. In the inviscid case the change is discontinuous. In viscous fluid the change is continuous but its lengthscale is of the order of the mean free path of particles as viscous forces are very weak away from boundaries. The relation of quantities across the shock is defined by the Rankine-Hugoniot relations which describe the jump of a variable ϕ , denoted by $[\phi]$, across a surface S . When \vec{n} is the unit vector normal to S and \vec{U} the vector of velocities, the Rankine-Hugoniot conditions for mass, momentum and energy are:

$$[\rho \vec{U} \cdot \vec{n}] = 0, \quad (1.27)$$

$$[\vec{U}] \rho \vec{U} \cdot \vec{n} + [p] \vec{n} = 0, \quad (1.28)$$

$$[h_{st}] \rho \vec{U} \cdot \vec{n} = 0. \quad (1.29)$$

Here the stagnation enthalpy, $h_{st} = h + u^2/2$, is used for the energy equation. Enthalpy itself is defined as $h = u + p/\rho$. These equations admit a number of different solutions. The most common one, the *shock-wave*, is described by a non-zero mass flux through the shock, $\vec{U} \cdot \vec{n} \neq 0$. In this case the following conditions for the tangential and normal velocity components, U_t and U_n ,

and the stagnation enthalpy can be derived.

$$[U_t] = 0, \tag{1.30}$$

$$[U_n]\rho U_n + [p] = 0, \tag{1.31}$$

$$[h_{st}] = 0. \tag{1.32}$$

In addition, the entropy, s , increases through the shock, satisfying the Second Law of Thermodynamics.

From the considerations in the previous sections, one can derive the following insights into a wall-bounded flow crossing a shock-wave:

- Flow velocity decreases
- Pressure increases rapidly
- The boundary-layer thickens or is separated
- The underlying surface is experiences high local loads
- A decrease in stagnation pressure which causes additional drag

This emphasizes why the study of shock-wave/boundary-layer interactions, where the shock location can oscillate in time, is so important.

Finite-Difference Discretization of the Skew-Symmetric Navier-Stokes Equations

The simulation of fluid flow places a large number of demands on numerical schemes. Most basic among these are consistency and accuracy. However, specific physical situation need to be addressed in specific ways. One example is the treatment of shocks. While the viscous nature of the Navier-Stokes equations yields a continuous shape of the shock, the length scale of said phenomena is very small, often in the order of the mean free path of gas particles. Because the discretization cannot resolve such small lengthscales shocks appear discontinuous in the numerics. Conservative schemes are able to treat these continuities in the correct manner. Schemes based on the integral formulation of the Navier-Stokes equations, like most Finite-Volume schemes have this property. Finite-Difference schemes, which utilize the differential formulation of the partial differential equations, struggle near shocks since the underlying assumption on the smoothness of the solution is violated. Spurious oscillations and crippling instabilities appear if no corrective measures are taken and even wrong shock speeds can occur. On the other hand, fluid flow features many phenomena, like small scale turbulence or acoustic propagation, that are greatly influenced by dissipation and dispersion. Take the propagation of sound, acoustic waves feature very small pressure and velocity fluctuations propagating with the a specific velocity, the speed of sound c . For numerical schemes to correctly simulate acoustic phenomena, no artificial dissipation mechanisms have to be present, as even small dissipation

can dampen acoustic perturbations to the point of nonexistence. In addition, the dispersion relation of the analytic equations has to be preserved in order to match the speed of sound. Finite-Difference schemes on structured grids allow for high-order of accuracy and nearly correct dispersion relations with comparably low computational costs. These traits make finite-difference schemes the preferred method for high-accuracy simulations of small-scale turbulence and acoustics. Other methods, often based on dissipative upwind formulas can invalidate results obtained from e.g. acoustic simulations.

The previous chapter introduced the skew-symmetric formulation of the Navier-Stokes equations, as given in equations (1.12)-(1.14), and motivated the relation between skew-symmetry and conservation. Special attention was paid to the convection term in the momentum equation and the fact that it does not change kinetic energy at all. In addition emphasis was placed on the transfer of energy from kinetic to internal energy.

This chapter will introduce finite-difference schemes that preserve these properties of the analytical equations. The resulting scheme will be of arbitrary order in space and time. It will exhibit no artificial, numerical dissipation and be unconditionally stable on periodic domains. Thus it will combine traits that make it a natural choice for the simulation of shock-laden turbulent flows, like the transonic shock-wave/boundary-layer. In particular, the correct treatment of the conservation properties is the first step for a numerically and analytically correct treatment of shocks. The non-existent numerical dissipation is necessary for the correct propagation of sound and pressure waves which play a crucial role in the transonic SBLI system where pressure information can scatter upstream. Lastly, the high possible order of the scheme makes direct numerical simulation of the turbulent boundary-layer feasible.

Before continuing, a note on the term conservative is in order. In the context of this work, conservation means the temporal preservation of a generic quantity within the flow field. Let φ be an arbitrary function of the field. Then the temporal rate of change of $\int \varphi dx$ is of interest. If $\partial_t \int \varphi dx = 0$, then the quantity φ is said to be conserved. In numerical mathematics, the term conservative, when applied to a numerical scheme, often describes a scheme that confirms with the Lax-Wendroff theorem which includes additional properties besides the discrete conservation. This is a purely spatial property that enables the scheme to correctly compute unsteady solutions. While the scheme constructed here will confirm with Lax-Wendroff, the term conservative is generally used in a slightly different meaning.

The following chapter is organized as follows. First, an overview of ex-

isting techniques and methods concerning skew-symmetric and conservative discretizations is given. Then, a spatial semi-discretization of the skew-symmetric equations is derived that is conservative in the semidiscrete setting. In section 2.3 the semi-discrete equations will be expanded to the fully discrete setting and time-integrators will be introduced that allow the scheme to be fully conservative in space and time. The two sections 2.2 and 2.3 contain the brunt of the work done in this chapter. Afterwards, the application and treatment of boundary conditions for the conservative discretization will be discussed. The following section 2.5 elevates the scheme to arbitrarily distorted cartesian grids. Before closing the chapter with notes of the implementation of the method on massively parallel computing systems, a conservative shock-capturing methodology is introduced based on the work of Bogey et al., see [8].

2.1. State of the Art

The notion of skew-symmetric schemes for the Navier-Stokes equations dates back to Feiereisen et al., [24], as well as Tadmor, [111]. Their schemes used the skew-symmetric formulation of conservation laws to construct numerical schemes with conserved quantities. The basic principle of skew-symmetric discretizations is to construct a discrete convection operator that does not change kinetic energy. Classical conservative formulations that conserve total energy by first principle, meaning through the fundamental theorem of calculus, can indiscriminately convert kinetic to internal energy. Often artificial, unwanted numerical dissipation destroys kinetic energy and increases internal energy in an unphysical manner. Skew-symmetric schemes prevent this from happening. Results of Pirozzoli et al., [72, 73], Blaisdell et al., [7], as well as Ducros, [21], have shown that the skew-symmetric, often called *split-convective*, formulation of the convective terms improves energy conservation and thus stability of finite-difference discretizations. Pirozzoli also proved that the split-convective form can be used to construct a locally conservative flux form. This ansatz has been applied in a variety of areas. In the context of compressible flow, skew-symmetric schemes have been used to study the nature of turbulent shear flow, [6], boundary-layers, [72], and low Machnumber flows, [63]. Skew-symmetric schemes are also available for the incompressible equations, e.g. [65, 66]. The underlying idea of the skew-symmetric formulation has been employed outside of the finite-difference context. Jameison constructs kinetic energy conserving finite-volume schemes in [40, 41].

Other examples include the work of Subbareddy and Candler, [110], and Kok, [46, 47]. Recently, applications in the Discontinuous-Galerkin ansatz have been developed by Gassner, [28]. As the numerous examples above testify, the use of the split-convective formulation for the conservation of kinetic energy yields excellent numerical schemes. One of the main goals of the development of skew-symmetric discretizations is the construction of fully conservative schemes. Schemes that not only preserve kinetic energy but emulate structural conservation properties of mass, momentum and total energy present in the Navier-Stokes equations, recent examples of this are Verstappen, Trias et al., [117,120], Morinishi, [63], as well as Brouwer et. al, [12]. The classical ansatz in fluid mechanics goes back to Morinishi et al., [65]. Through skillful averaging on staggered grids, Morinishi et al. derive skew-symmetric formulations of the convection operator that conserve kinetic energy by fist principle. Extensions of this approach have been developed in recent years that apply this method to compressible flows, [62]. However, this is not the only way to achieve conservation. Reiss et. al., [82], present a matrix-driven skew-symmetric discretization which features full conservation. In contrast to many of the above mentioned approaches, Reiss and Sesterhenns approach allows generic finite-difference stencils for the spatial discretization and uses no individually constructed averaging procedures. In the analytical equations, skew-symmetry yields temporal conservation through the product rule. Since the product rule generally does not hold in the discrete equations, all fully conservative schemes try to emulate this property to some extent. For a long time, schemes that conserve mass, momentum and energy in the spatial and temporal discrete equations were restricted to second and fourth order in time, see e.g. [120]. Temporal conservation necessitates implicit time integrators and all temporally conservative schemes can be viewed as modifications of the *implicit midpoint rule*, see [63,110]. Recently, both Brouwer et al., see [10,12] and Rozema et al., [89], were independently able to extent the ideas introduced by Morinishi, [63], Subbarredy and Candler, [110], to time integrators of arbitrary order. Both conclude that a specific family of implicit Runge-Kutta schemes can be used to achieve full conservation in time. Similar results for the incompressible equations are presented in [92]. Apart from the temporal discretization, the extension of conservative skew-symmetric schemes to distorted grids and the correct implementation of boundary conditions are topics of continuing interest. Recent advances in the extension of skew-symmetric schemes to arbitrary grids have been made by Reiss and Morinishi, [64,82]. Both were able to extent their respective methods to non-uniform, structured grids. Trias et al., [117], achieve the same for a

Finite-Volume discretization of the incompressible Navier-Stokes equations. Boundary conditions in skew-symmetric schemes deserve more attention in conservative discretization. Fluxes over the boundary naturally change the conserved quantities over time. When boundary conditions are set in the discrete case, care has to be taken as to not introduce artificial sources or sinks of mass, momentum or energy. A way to achieve this, as used in [82], is the use of *summation-by-parts* matrices for the spatial discretization. These matrices allow for the numerical boundary flux to be completely determined by the boundary point. Thus the analytical fluxes can be retained in the discrete case. Carpenter et al., [26], give a recent overview on this topic.

2.2. Conservative Discretization in Space

In this section a conservative semidiscretization of the skew-symmetric Navier-Stokes equations will be constructed. Before proving the main theorem of this section a short example is used to illustrate the notation and methods used throughout the chapter. This example will use Burger's equation,

$$\partial_t u + \partial_x \left(\frac{u^2}{2} \right) = 0, \quad (2.1)$$

as a model for the nonlinear equation of momentum on a one-dimensional domain, Ω . Until boundaries are discussed in section 2.4 all domains are assumed to be periodic. Although equation (2.1) has no direct physical interpretation it can be shown to conserve two quantities tentatively named kinetic energy, $\int_{\Omega} \left(\frac{u^2}{2} \right) dx$, and momentum, $\int_{\Omega} u dx$. The conservation of momentum follows directly from integrating the conservative form of the Burgers equation, presented above, over the whole domain. The conservation of kinetic energy can be shown by constructing the skew-symmetric form of the equation. It is the combination of equation (2.1) and the quasi-linear form of the Burgers equation

$$\partial_t u + u \partial_x u = 0. \quad (2.2)$$

Combining both, one arrives at

$$\partial_t u + \frac{1}{3} (\partial_x u \cdot + u \partial_x \cdot) u = 0. \quad (2.3)$$

As the spatial derivative operator is skew-symmetric, the energy $\int_{\Omega} \left(\frac{u^2}{2}\right) dx$ is conserved. Now, a spatial discretization is constructed for equation (2.3) that retains these conservation properties.

Throughout chapter 2, the domain Ω is discretized with M uniformly placed gridpoints. Therefore any quantity ϕ on the grid is represented as $\phi = (\phi_i, \dots, \phi_M)^T$. In case pointwise multiplication of two variables is needed, the diagonal matrix $\Phi = \text{diag}(\phi)$ is introduced. The spatial derivative $\partial_x \cdot$ is replaced by the application of a discrete differentiation matrix $D \in \mathbb{R}^{M \times M}$.

This results in the semidiscrete representation of (2.3) being:

$$\partial_t u = -\frac{1}{3}(DU + UD)u. \quad (2.4)$$

The discrete expression for the momentum on a uniform grid with stepsize Δx is given by

$$\int_{\Omega} u dx \approx \Delta x \sum_{i=1}^M u_i = \Delta x \mathbf{1}^T u. \quad (2.5)$$

while kinetic energy is given as

$$\int_{\Omega} \left(\frac{u^2}{2}\right) dx \approx \frac{\Delta x}{2} \sum_{i=1}^M u_i u_i = \frac{\Delta x}{2} u^T u. \quad (2.6)$$

In the analytical case, energy was conserved due to the skew-symmetry of the operator $(\partial_x u \cdot + u \partial_x \cdot)$. Assuming the discrete operator $A = (DU + UD)$ is skew-symmetric as well, discrete energy is conserved in the same manner. Equation 2.3 is multiplied by u^T from the left. Note that the factor Δx will be neglected for simpler notation. This will be continued throughout the chapter since the conservation is unaffected by the multiplication with a scalar:

$$\begin{aligned} \partial_t \left(\frac{u^T u}{2}\right) &= \frac{1}{3} u^T (DU + UD) u \\ &= \frac{1}{3} u^T A u \\ &= \frac{1}{3} u^T A^T u \\ &= -\frac{1}{3} u^T A^T u \\ &= 0 \end{aligned} \quad (2.7)$$

Thus, the skew-symmetry of the discrete differentiation operator

$$A = (DU + UD) \quad (2.8)$$

ensures conservation of energy. Since u cannot be controlled and $U = U^T$, the differentiation matrix D has to be chosen accordingly and a skew-symmetric D implies a skew-symmetric A :

$$A^T = (DU + UD)^T = (UD^T + D^T U) = -(DU + UD) = -A. \quad (2.9)$$

The discrete momentum is conserved when the matrix-vector product $\mathbf{1}^T D$ is set to zero. This property is called the *telescoping sum property* and implies that the sum of all the columns of D is zero. Take a look at the discrete equation for momentum conservation:

$$\begin{aligned} \partial_t(\mathbf{1}^T u) &= -\frac{1}{3} \mathbf{1}^T (DU + UD) u & (2.10) \\ &= -\frac{1}{3} (\mathbf{1}^T DU + \mathbf{1}^T UD) u \\ &= -\frac{1}{3} (u^T Du) \\ &= 0. \end{aligned}$$

Where the last step again requires the skew-symmetry of D . Thus the semidiscrete Burgers equation, eq. (2.4), conserves momentum and energy if the differentiation matrix D fulfills the twin requirements of skew-symmetry and the telescoping sum property:

$$D = -D^T, \quad \mathbf{1}^T D = 0. \quad (2.11)$$

The most important question at this point is whether there exist suitable differentiation schemes such that D fulfills these requirements. In fact, the matrix form of all central difference schemes on periodic, equidistant grids, which can be expressed in the general form,

$$u'_i = \sum_{k=1}^m \alpha_k (u_{i+k} - u_{i-k}), \quad (2.12)$$

is skew-symmetric and the telescoping sum property is a basic constraint on the consistency of a numerical differentiation scheme on periodic grids. This

allows great freedom in the choice of the spatial derivative. Central differences are available in arbitrary (even) order of accuracy, $\mathcal{O}(\Delta x^p)$ with the order being $p = 2m$ if so desired. Alternatively, degrees of freedom can be used to improve other aspects of the derivative, e.g. a better dispersion relation, at the cost of the order. The most famous example of such a derivative being the 4th order Tam & Webb scheme, see [112].

After this introductory example the application to the skew-symmetric Navier-Stokes equations, derived in chapter 1, follows. For reference, the equations that will be discretized take the following form:

$$\begin{aligned} \partial_t \rho + \partial_{x_\alpha} (\rho u_\alpha) &= 0, \\ \frac{1}{2} (\partial_t \rho \cdot + \rho \partial_t \cdot) u_\alpha + \frac{1}{2} (\partial_{x_\beta} \rho u_\beta \cdot + \rho u_\beta \partial_{x_\beta} \cdot) u_\alpha + \partial_{x_\alpha} p &= \partial_{x_\beta} \tau_{\alpha\beta}, \\ \frac{1}{\gamma - 1} \partial_t p + \frac{\gamma}{\gamma - 1} \partial_{x_\alpha} (u_\alpha p) - u_\alpha \partial_{x_\alpha} p + u_\alpha \partial_{x_\alpha} \tau_{\alpha\beta} - \partial_{x_\beta} u_i \tau_{\alpha\beta} &= -\partial_{x_\alpha} \Phi_\alpha. \end{aligned}$$

These equations are discretized on a three-dimensional domain with an equidistant grid using $[M_1, M_2, M_3]$ points. Therefore, each discrete quantity is represented on the computational domain as $\phi = (\phi)_{ijk}$, $i, j, k = 1, \dots, M_{1,2,3}$ and $\phi \in \mathbb{R}^{(M_1 \times M_2 \times M_3)}$. For the proof of the conservation properties, ϕ is then reordered into a long one-dimensional vector, $\phi \in \mathbb{R}^{(M_1 M_2 M_3)}$:

$$(\phi_{(1,1,1)}, \dots, \phi_{(M_1,1,1)}, \phi_{(1,2,1)}, \dots, \phi_{(M_1, M_2, 1)}, \phi_{(1,1,2)}, \dots, \phi_{(M_1, M_2, M_3)}). \quad (2.13)$$

Again, $\Phi = \text{diag}(\phi)$, is used to represent pointwise multiplications of variables. Performing a direct discretization of the above equations, the following theorem holds:

Theorem 1. *Let $D_i^1 \in \mathbb{R}^{M_i \times M_i}$, $i = 1, 2, 3$, be a differentiation matrix which has the properties*

$$(D_i^1)^T = -D_i^1, \quad \mathbf{1}^T D_i^1 = 0, \quad (2.14)$$

and

$$D_1 = (D_1^1 \otimes \mathbf{I}_{M_2} \otimes \mathbf{I}_{M_3}), \quad (2.15)$$

$$D_2 = (\mathbf{I}_{M_1} \otimes D_2^1 \otimes \mathbf{I}_{M_3}), \quad (2.16)$$

$$D_3 = (\mathbf{I}_{M_1} \otimes \mathbf{I}_{M_2} \otimes D_3^1), \quad (2.17)$$

where $\mathbf{I}_n \in \mathbb{R}^{n \times n}$ is the identity matrix and \otimes is Kronecker matrix product while $R = \text{diag}(\rho)$ and $U_\alpha = \text{diag}(u_\alpha)$. Then the semidiscrete, three-dimensional Navier-Stokes equations on periodic grids,

$$\partial_t \rho = -D_\alpha R u_\alpha, \quad (2.18)$$

$$\frac{1}{2} (\partial_t R \cdot + R \partial_t \cdot) u_\alpha = -\frac{1}{2} (D_\beta R U_\beta + R U_\beta D_\beta) u_\alpha - D_\alpha p + D_\beta \tau_{\alpha\beta}, \quad (2.19)$$

$$\begin{aligned} \partial_t p = & -\gamma D_\alpha U_\alpha p + (\gamma - 1) \left((U_\alpha D_\alpha p - U_\alpha D_\alpha \tau_{\alpha\beta} \right. \\ & \left. + D_\beta U_\alpha \tau_{\alpha\beta} - D_\alpha \Phi_\alpha \right), \end{aligned} \quad (2.20)$$

conserve discrete mass, momentum and total energy:

$$\partial_t (\mathbf{1}^T \rho) = 0, \quad (2.21)$$

$$\partial_t \frac{1}{2} (\rho^T u_\alpha) = 0, \quad (2.22)$$

$$\partial_t \left(\frac{1}{\gamma - 1} \mathbf{1}^T p + \frac{1}{2} (u_\alpha^T R u_\alpha) \right) = 0. \quad (2.23)$$

In addition, kinetic energy is not changed through convection.

Proof. The unusual representation of the three-dimensional differentiation operators through the use of the Kronecker product applied to a one-dimensional vector simplifies the proof of the conservation properties immensely. In effect, it allows the use of the same methodology as in the previous, one-dimensional example using the Burgers equation. First of all, the properties of the Kronecker product can be used to show that the skew-symmetry of D_i^1 implies the skew-symmetry of D_i . The same is true for the telescoping sum property.

$$(D_i^1)^T = -D_i^1 \implies (D_i)^T = -D_i, \quad (2.24)$$

$$\mathbf{1}^T (D_i^1) = 0 \implies \mathbf{1}^T (D_i) = 0. \quad (2.25)$$

Conservation of Mass The conservation of mass is the most basic conservation property. In fact, all consistent finite-difference discretizations conserve mass by first principle. The rate of change of total mass is given by

$$\partial_t \mathbf{1}^T \rho = - \underbrace{\mathbf{1}^T D_\alpha R u_\alpha}_{=0} = 0. \quad (2.26)$$

Thus, mass is conserved.

Conservation of Momentum Conservation of momentum is not achieved via first principle. In fact, equation (2.19) does not have the telescoping sum property to ensure conservation. Instead the goal is achieved using the skew-symmetry of D together with a consistent discretization and coupling with the equation of mass, (2.18). The product rule implies $\partial_t \rho u_\alpha = \frac{1}{2} u_\alpha \partial_t \rho + \frac{1}{2} (\partial_t \rho \cdot + \rho \partial_t \cdot) u_\alpha$. This can be expressed in semidiscrete form for the integral of momentum over the whole domain Ω as:

$$\partial_t (\rho^T u_\alpha) = \frac{1}{2} u_\alpha^T \partial_t \rho + \mathbf{1}^T \frac{1}{2} (\partial_t R \cdot + R \partial_t \cdot) u_\alpha. \quad (2.27)$$

The first term on the right hand side is the equation of mass multiplied from the left with $\frac{1}{2} u_\alpha^T$. Plugging in both equations (2.18) and (2.19) results in:

$$\begin{aligned} \partial_t (\rho^T u_\alpha) &= -\frac{1}{2} u_\alpha^T D_\beta R u_\beta - \frac{1}{2} \mathbf{1}^T (D_\beta R U_\beta + R U_\beta D_\beta) u_\alpha - \mathbf{1}^T D_\alpha p + \mathbf{1}^T D_\beta \tau_{\alpha\beta} \\ &= -\frac{1}{2} u_\alpha^T D_\beta R u_\beta - \frac{1}{2} \mathbf{1}^T U_\beta R D_\beta u_\alpha \\ &= -\frac{1}{2} u_\alpha^T D_\beta R + \frac{1}{2} u_\alpha^T D_\beta R u_\beta = 0. \end{aligned} \quad (2.28)$$

The last step utilizes the identities $\mathbf{1}^T U_\alpha = u_\alpha^T$ and $D_\beta^T = -D_\beta$. Thus, through consistent discretization of both mass and momentum equation, the discrete momentum is conserved over time.

Conservation of Total Energy Like the conservation of momentum, the conservation of energy relies on the consistent discretization of two equations. In this case the momentum, (2.19), and energy, (2.20), equations. The momentum equation is used to derive a formula for the temporal evolution of the discrete kinetic energy $\frac{1}{2} (u_\alpha^T R u_\alpha)$. It will be shown that only friction and pressure work change kinetic energy. This change is exactly balanced by the rate of change of discrete internal energy, $\left(\frac{1}{\gamma-1} \mathbf{1}^T p\right)$, derived from equation (2.20). Multiplying (2.19) with u_α^T from the left results in

$$\begin{aligned} \frac{1}{2} \partial_t (u_\alpha^T R u_\alpha) &= -\frac{1}{2} u_\alpha^T \underbrace{(D_\beta R U_\beta + R U_\beta D_\beta)}_{=0} u_\alpha - u_\alpha^T D_\alpha p + u_\alpha D_\beta \tau_{\alpha\beta} \\ &= -u_\alpha^T D_\alpha p + u_\alpha D_\beta \tau_{\alpha\beta}. \end{aligned} \quad (2.29)$$

This is the temporal rate of change of kinetic energy, proving that convection does not change kinetic energy in the semidiscrete case due to the skew-

symmetry of the convection operator. The discrete sum of (2.20) is

$$\begin{aligned}
 \partial_t \left(\frac{1}{\gamma-1} \mathbf{1}^T p \right) &= - \frac{\gamma}{\gamma-1} \underbrace{\mathbf{1}^T D_\alpha U_\alpha p}_{=0} + \mathbf{1}^T U_\alpha D_\alpha p - \mathbf{1}^T U_\alpha D_\alpha \tau_{\alpha\beta} \\
 &\quad + \underbrace{\mathbf{1}^T D_\beta U_\alpha \tau_{\alpha\beta}}_{=0} - \underbrace{\mathbf{1}^T D_\alpha \Phi_\alpha}_{=0} \\
 &= u_\alpha^T D_\alpha p - u_\alpha^T D_\alpha \tau_{\alpha\beta}.
 \end{aligned} \tag{2.30}$$

Adding up (2.28) and (2.30) results in the desired conservation property:

$$\begin{aligned}
 \partial_t \left(\frac{1}{\gamma-1} \mathbf{1}^T p + \frac{1}{2} (u_\alpha^T R u_\alpha) \right) &= -u_\alpha^T D_\alpha p + u_\alpha D_\beta \tau_{\alpha\beta} + u_\alpha^T D_\alpha p - u_\alpha^T D_\alpha \tau_{\alpha\beta} \\
 &= 0.
 \end{aligned} \tag{2.31}$$

□

Corollary 1 (Discretization of the friction terms). *In the above proof, the skew-symmetry of D is necessary to ensure the convective terms in the temporal evolution of various quantities vanish. When the friction terms are concerned, only the telescoping sum property is needed. This allows an even greater degree of freedom in the choice of discretization methods. Only the convective terms have to be discretized using skew-symmetric, central schemes while non-symmetric upwind schemes can be used for the friction terms.*

Unless otherwise noted, all simulations provided in this thesis have been performed using central difference schemes.

Previously it was remarked that the term *conservative* in the context of numerical mathematics often refers to schemes that comply with the Lax-Wendroff theorem. The Lax-Wendroff theorem states, that if a numerical scheme for conservation laws with consistent and local fluxes converges to a solution u in the limit of increasing grid refinement, then u is a weak solution of the underlying conservation law. As such, the numerical scheme is able to predict discontinuities with confidence and converges to a true solution of the underlying problem. A numerical flux is said to be local if it is calculated from a finite number of neighboring values and consistent if it reduces to the analytical flux for constant solutions. The discretization scheme developed here is not written or implemented in flux form, but Reiss et al., see [82], show that the present formulation can be written in flux form. They were then able to show the following.

Corollary 2 (Consistent and Local Fluxes). *The semidiscrete, conservative discretization of the skew-symmetric Navier-Stokes equations has local and consistent fluxes.*

2.3. Conservative Discretization in Time

This section's goal is to extend the conservative semidiscretization obtained in section 2.2 to achieve full conservation in space and time. The theory and results presented in this section have been published by the author in [12]. Conservative integration in time is not self-evident. The approach taken here to construct conservative schemes of arbitrary order is inspired by Morinishi et al., [63], and Subbareddy and Candler, [110]. In both cases, the authors were able to construct a conservative time integrator of second order. While both works come from different backgrounds, their results are remarkably similar. Subbareddy and Candler develop a skew-symmetric finite-volume scheme and take inspiration from Roe's approximate Riemann solver, while Morinishi et al. construct conservative finite-difference schemes through averaging of the considered quantities. Both construct second-order accurate schemes that are modifications of the implicit midpoint rule. The modifications being that the intermediate value for the velocity in the convective term of the equation of momentum is replaced by the so-called *density-weighted velocity*

$$\frac{(\sqrt{\rho}u)^{n+1} + (\sqrt{\rho}u)^n}{(\sqrt{\rho})^{n+1} + (\sqrt{\rho})^n}. \quad (2.32)$$

This section details a generalization of this approach to schemes of arbitrary order. This is done in two steps. Instead of modifying the implicit midpoint rule, the skew-symmetric Navier-Stokes equations are modified in such a way that the density-weighted velocity appears when the genuine implicit midpoint rule is applied. Afterwards, it will be shown that the method can be extended to schemes of arbitrary order.

Rewriting of the Skew-Symmetric Navier-Stokes Equations Here, the formulation of the skew-symmetric Navier-Stokes equations used for the fully conservative finite-difference scheme is constructed. The cumbersome, skew-symmetric temporal difference operator in the momentum equation will be

eliminated. Following Morinishi, [63], it can be expressed as

$$\frac{1}{2}(\partial_t \rho \cdot + \rho \partial_t \cdot) u_\alpha = (\sqrt{\rho}) \frac{\partial}{\partial t} (\sqrt{\rho} u_\alpha). \quad (2.33)$$

This eliminates the double temporal difference in the equation and motivates a rewriting of equations (1.12)-(1.14) in the variables $((\sqrt{\rho}), (\sqrt{\rho} u_\alpha), p)$:

$$\frac{1}{2}(\sqrt{\rho}) \partial_t (\sqrt{\rho}) + \partial_{x_\alpha} (\rho u_\alpha) = 0, \quad (2.34)$$

$$(\sqrt{\rho}) \frac{\partial}{\partial t} (\sqrt{\rho} u_\alpha) + \frac{1}{2} (\partial_{x_\beta} \rho u_\beta \cdot + \rho u_\beta \partial_{x_\beta} \cdot) u_\alpha + \partial_{x_\alpha} p = \partial_{x_\beta} \tau_{\alpha\beta}, \quad (2.35)$$

$$\frac{1}{\gamma-1} \partial_t p + \frac{\gamma}{\gamma-1} \partial_{x_\alpha} (u_\alpha p) - u_\alpha \partial_{x_\alpha} p + u_\alpha \partial_{x_\alpha} \tau_{\alpha\beta} - \partial_{x_\beta} u_i \tau_{\alpha\beta} = -\partial_{x_\alpha} \Phi_\alpha. \quad (2.36)$$

where $\rho = (\sqrt{\rho})^2$, $u_\alpha = (\sqrt{\rho} u_\alpha) / (\sqrt{\rho})$ and $\rho u_\alpha = (\sqrt{\rho})(\sqrt{\rho} u_\alpha)$, so that only the new set of variables, called the skew-symmetric set of variables, is used within the equations. Application of the unmodified implicit midpoint rule to the equations given above, given for a generic ordinary differential equation $\dot{y} = f(y)$ as

$$y^{n+1} = y^n + \Delta t f \left(\frac{y^{n+1} + y^n}{2} \right), \quad (2.37)$$

results in the same term for the intermediate velocity as in [63] and [110]. In the following, it will be shown that the implicit midpoint rule, and in fact a whole class of time integrators, applied to a discretization of the skew-symmetric Navier-Stokes equations, as given above, is fully conservative in space and time. For purposes of notation, the time domain $[0, T]$ is discretized at the discrete points $t^i = i\Delta t$, $i = 0, N$. A generic quantity at timestep i is denoted as ϕ^i .

Theorem 2. *Let $D_i^1 \in \mathbb{R}^{M_i \times M_i}$, $i = 1, 2, 3$, be a differentiation matrix which has the properties*

$$(D_i^1)^T = -D_i^1, \quad \mathbf{1}^T D_i^1 = 0, \quad (2.38)$$

and

$$D_1 = (D_1^1 \otimes \mathbf{I}_{M_2} \otimes \mathbf{I}_{M_3}), \quad (2.39)$$

$$D_2 = (\mathbf{I}_{M_1} \otimes D_2^1 \otimes \mathbf{I}_{M_3}), \quad (2.40)$$

$$D_3 = (\mathbf{I}_{M_1} \otimes \mathbf{I}_{M_2} \otimes D_3^1), \quad (2.41)$$

where $\mathbf{I}_n \in \mathbb{R}^{n \times n}$ is the identity matrix and \otimes is Kronecker matrix product. Let $R = \text{diag}((\sqrt{\rho})^2)$, $(\sqrt{R})^{-1} = \text{diag}(1/(\sqrt{\rho}))$ and $U_\alpha = \text{diag}((\sqrt{\rho}u_\alpha)/(\sqrt{\rho}))$. Then all Runge-Kutta schemes whose coefficient fulfill

$$b_i a_{ij} + b_j a_{ji} = b_i b_j, \quad (2.42)$$

and thus are symplectic and conserve quadratic invariants, e.g. Gauss-collocation methods, applied to the semidiscrete, three-dimensional skew-symmetric Navier-Stokes equations on periodic grids,

$$\partial_t(\sqrt{\rho}) = -\frac{1}{2}(\sqrt{R})^{-1}D_\alpha R u_\alpha, \quad (2.43)$$

$$\begin{aligned} \partial_t(\sqrt{\rho}u_\alpha) = & -\frac{1}{2}(\sqrt{R})^{-1}(D_\beta R U_\beta + U_\beta R D_\beta)u_\alpha \\ & -(\sqrt{R})^{-1}D_\alpha p + (\sqrt{R})^{-1}D_\beta \tau_{\alpha\beta}, \end{aligned} \quad (2.44)$$

$$\begin{aligned} \partial_t p = & -\gamma D_\alpha U_\alpha p + (\gamma - 1)\left(U_\alpha D_\alpha p - U_\alpha D_\alpha \tau_{\alpha\beta} \right. \\ & \left. + D_\beta U_\alpha \tau_{\alpha\beta} - D_\alpha \Phi_\alpha\right), \end{aligned} \quad (2.45)$$

conserve discrete mass, momentum and total energy:

$$\mathbf{1}^T \rho^N - \mathbf{1}^T \rho^0 = 0, \quad (2.46)$$

$$\mathbf{1}^T (\sqrt{\rho}u_\alpha)^N - \mathbf{1}^T (\sqrt{\rho}u_\alpha)^0 = 0, \quad (2.47)$$

$$\left(\frac{1}{\gamma - 1} \mathbf{1}^T p^N + \frac{1}{2} ((\sqrt{\rho}u_\alpha)(\sqrt{\rho}u_\alpha)) \right) - E^0 = 0. \quad (2.48)$$

In addition, kinetic energy is not changed through convection.

Before proceeding with the proof of theorem 2, it is prudent to recall a few facts about Runge-Kutta time integrators and their properties. In general, a Runge-Kutta method can be written as

$$y^{n+1} = y_n + \Delta t \sum_{i=1}^s b_i k_i, \quad (2.49)$$

$$k_i = f(t^n + c_i \Delta t, Y_i), \quad (2.50)$$

$$Y_i = y^n + \Delta t \sum_{j=1}^s a_{ij} k_j. \quad (2.51)$$

The coefficients a_{ij} , b_i and c_i are usually given in form of the so-called Butcher table:

$$\begin{array}{c|c} c_i & a_{ij} \\ \hline & b_j \end{array}.$$

The key to the generalization of the conservative approach to time-integrators of arbitrary order is the realization that the implicit midpoint rule is the simplest member of a whole class of time integrators, the so-called Gauss-collocation methods. These methods can be constructed with an arbitrary number of stages s and are of order of accuracy $2s$, as shown by Butcher in 1964, [13]. Construction of the schemes is based on the Legendre interpolation points and they can be shown to be A- and B-stable as well as symplectic and conserve quadratic invariants, see [34]. The Butcher table of the Gauss-collocation methods of order 2, the implicit midpoint rule, and order 4 are given below.

$$\begin{array}{c|c} \frac{1}{2} & \frac{1}{2} \\ \hline & 1 \end{array}, \quad (2.52)$$

$$\begin{array}{c|cc} \frac{1}{2} - \frac{\sqrt{3}}{6} & \frac{1}{4} & \frac{1}{4} - \frac{\sqrt{3}}{6} \\ \frac{1}{2} + \frac{\sqrt{3}}{6} & \frac{1}{4} + \frac{\sqrt{3}}{6} & \frac{1}{4} \\ \hline & \frac{1}{2} & \frac{1}{2} \end{array} \quad (2.53)$$

Theorem 2 states, that all Runge-Kutta methods that conserve quadratic invariants lead to fully conservative schemes when applied to the semidiscrete skew-symmetric Navier-Stokes equations written in skew-symmetric variables. Let $\dot{y} = f(y)$, $y \in \mathbb{R}^n$ be a system of ordinary differential equations and $C \in \mathbb{R}^{n \times n}$ a symmetric matrix. Then

$$Q(y) = y^T C y \quad (2.54)$$

is a quadratic invariant of the system if

$$y^T C f(y) = 0 \quad \forall y \in \mathbb{R}^n. \quad (2.55)$$

Cooper's theorem, see [16], states that all Runge-Kutta methods whose coefficients satisfy

$$b_i a_{ij} + b_j a_{ji} = b_i b_j \quad (2.56)$$

conserve quadratic invariants. In addition, relation (2.42) also implies that the corresponding Runge-Kutta scheme is symplectic, for a proof of both of these facts see [34]. It is then easy to proof the following

Lemma 1. *Gauss-collocation methods conserve quadratic invariants.*

2.3.1. Proof of theorem 2

With these tools available, theorem 2 can be proven. For the sake of brevity, the proof is only conducted for the one-dimensional version of equations (2.43)-(2.45). In addition, the following notation of the equations is introduced and used within the proof:

$$\begin{pmatrix} (\sqrt{\rho})_t \\ (\sqrt{\rho}u)_t \\ p_t \end{pmatrix} = \begin{pmatrix} f^\rho \\ f^{\rho u} \\ f^p \end{pmatrix} \quad \text{and} \quad k_i = \begin{pmatrix} k_i^\rho \\ k_i^{\rho u} \\ k_i^p \end{pmatrix} = \begin{pmatrix} f^\rho(Y_i) \\ f^{\rho u}(Y_i) \\ f^p(Y_i) \end{pmatrix}.$$

Note that is proof is taken from the authors previous work in [12].

Proof. The proof follows the same script as in section 2.2. First, the conservation of mass will be shown, followed by momentum and energy where special emphasis is placed on the rate of change of kinetic energy.

Conservation of Mass As in the semidiscrete case, the conservation of mass can be shown in a straightforward manner when considering the above notions on quadratic quantities. With the equation of mass being

$$(\sqrt{\rho})_t = -(\sqrt{R})^{-1}DRu,$$

it is clear that mass, $1^T \rho = (\sqrt{\rho})^T(\sqrt{\rho})$, can be expressed as a quadratic function and

$$(\sqrt{\rho})^T f^\rho = -(\sqrt{\rho})^T(\sqrt{R})^{-1}DRu = 1^T DRu = 0 \quad (2.57)$$

holds true because of the *telescoping sum property* imposed on D . Therefore, mass is a quadratic invariant and is conserved by all suitable integration methods.

Conservation of Momentum Again, as in the semidiscrete case, momentum and energy are conserved through the consistent coupling of two different equations. First, the conservation of momentum, $1^T(\rho u) = (\sqrt{\rho})^T(\sqrt{\rho}u)$, through the use of equations (2.43) and (2.44) is shown by direct application

of the Runge-Kutta formula, (2.49):

$$\begin{aligned}
 (\sqrt{\rho})^{n+1T} (\sqrt{\rho}u)^{n+1} &= \left((\sqrt{\rho})^n + \Delta t \sum_{i=1}^s b_i k_i^\rho \right)^T \left((\sqrt{\rho}u)^n + \Delta t \sum_{j=1}^s b_j k_j^{\rho u} \right) \\
 &= (\sqrt{\rho})^{nT} (\sqrt{\rho}u)^n + \Delta t \sum_{j=1}^s b_j (\sqrt{\rho})^{nT} k_j^{\rho u} \\
 &\quad + \Delta t \sum_{i=1}^s b_i k_i^{\rho T} (\sqrt{\rho}u)^n + (\Delta t)^2 \sum_{i,j=1}^s b_i b_j k_i^{\rho T} k_j^{\rho u}.
 \end{aligned}$$

Equations (2.50) and (2.51) can be used to write $y^n = Y_i - \Delta t \sum a_{ij} k_j$ and insert this into the above expression:

$$\begin{aligned}
 (\sqrt{\rho})^{n+1T} (\sqrt{\rho}u)^{n+1} &= (\sqrt{\rho})^{nT} (\sqrt{\rho}u)^n \\
 &\quad + \left[\Delta t \sum_{j=1}^s b_j \left(Y_j^\rho - \Delta t \sum_{i=1}^s a_{ji} k_i^\rho \right)^T k_j^{\rho u} \right] \\
 &\quad + \left[\Delta t \sum_{i=1}^s b_i k_i^{\rho T} \left(Y_i^{\rho u} - \Delta t \sum_{j=1}^s a_{ij} k_j^{\rho u} \right) \right] \\
 &\quad + (\Delta t)^2 \sum_{i,j=1}^s b_i b_j k_i^{\rho T} k_j^{\rho u} \\
 &= (\sqrt{\rho})^{nT} (\sqrt{\rho}u)^n \\
 &\quad + \underbrace{\Delta t \sum_{j=1}^s b_j Y_j^{\rho T} k_j^{\rho u}}_A + \underbrace{\Delta t \sum_{i=1}^s b_i k_i^{\rho T} Y_i^{\rho u}}_B \\
 &\quad + \underbrace{(\Delta t)^2 \sum_{i,j=1}^s (b_i b_j - b_j a_{ji} - b_i a_{ij}) k_i^{\rho T} k_j^{\rho u}}_C.
 \end{aligned}$$

Expression C reduces to zero due to equation (2.42) and the terms B and C cancel each other out as will be shown. The products summed up in

expression A take the form

$$\begin{aligned}
 Y_i^{\rho^T} k_i^{\rho u} &= (\sqrt{\rho})_i^T f^{\rho u}((\sqrt{\rho}u)_i) \\
 &= (\sqrt{\rho})_i^T \left(-\frac{1}{2}(\sqrt{R})_i^{-1} (DR_i U_i + U_i R_i D) u_i \right) \\
 &\quad + (\sqrt{\rho})_i^T \left(-(\sqrt{R})_i^{-1} D p_i + (\sqrt{R})_i^{-1} D \tau_i \right) \\
 &= -\frac{1}{2} 1^T (DR_i U_i + U_i R_i D) u_i - 1^T D p_i + 1^T D \tau_i \\
 &= -\frac{1}{2} u_i^T R_i D u_i \\
 &= \frac{1}{2} u_i^T DR_i u_i,
 \end{aligned} \tag{2.58}$$

while the products in B can be computed as

$$\begin{aligned}
 Y_i^{\rho u^T} k_i^{\rho} &= (\sqrt{\rho}u)_i^T f^{\rho}((\sqrt{\rho})_i) \\
 &= (\sqrt{\rho}u)_i^T \left(-\frac{1}{2}(\sqrt{R})_i^{-1} DR_i u_i \right) \\
 &= -\frac{1}{2} u_i^T DR_i u_i.
 \end{aligned} \tag{2.59}$$

Thus A and B add to zero and the conservation of momentum is given as:

$$(\sqrt{\rho})^{n+1^T} (\sqrt{\rho}u)^{n+1} = (\sqrt{\rho})^{n^T} (\sqrt{\rho}u)^n. \tag{2.60}$$

Conservation of Total Energy Conservation of total energy is shown by balancing the rate of change of kinetic energy, $e_{kin} = (\frac{1}{2}(\sqrt{\rho}u)^T(\sqrt{\rho}u))$, with that of internal energy $e = \frac{1}{\gamma-1} (1^T p)$. Kinetic energy is expanded using the Runge-Kutta formula in the same way the momentum was previously:

$$\begin{aligned}
 (\sqrt{\rho}u)^{n+1^T} (\sqrt{\rho}u)^{n+1} &= (\sqrt{\rho}u)^{n^T} (\sqrt{\rho}u)^n \\
 &\quad + 2\Delta t \underbrace{\sum_{i=1}^s b_i Y_i^{\rho u^T} k_i^{\rho u}}_{A'} \\
 &\quad + \Delta t^2 \underbrace{\sum_{i,j=1}^s (b_i b_j - b_i a_{ij} - b_j a_{ji}) k_i^{\rho u^T} k_j^{\rho u}}_{C'}.
 \end{aligned}$$

where expression C' is zero due to the conservation of quadratic quantities. The product terms in A' can be written as

$$\begin{aligned}
 Y_i^{\rho u_i^T} k_i^{\rho u} &= (\sqrt{\rho u})_i^T f^{\rho u} ((\sqrt{\rho u})_i) \\
 &= (\sqrt{\rho u})_i^T \left(-\frac{1}{2} (\sqrt{R})_i^{-1} (DR_i U_i + U_i R_i D) u_i \right) \\
 &\quad (\sqrt{\rho u})^T \left(-(\sqrt{R})_i^{-1} D p_i + (\sqrt{R})^{-1} D \tau_i \right) \\
 &= -\frac{1}{2} u_i (DR_i U_i + U_i R_i D) u_i - u_i^T D p_i + u_i^T D \tau_i \\
 &= -u_i D p_i + u_i D \tau_i.
 \end{aligned} \tag{2.61}$$

Thus the discrete rate of change in kinetic energy is given by

$$\frac{1}{2} (\sqrt{\rho u})^{n+1^T} (\sqrt{\rho u})^{n+1} - e_{kin}^n = \Delta t \sum_{i=1}^s b_i (-u_i^T D p_i + u_i^T D \tau_i). \tag{2.62}$$

Equation (2.62) states that the kinetic energy is only changed by pressure work and friction. This mirrors the analytical behavior of kinetic energy discussed in chapter 1. The temporal evolution of pressure, i.e. the internal energy, is given by

$$\begin{aligned}
 1^T p^{n+1} &= 1^T p^n + \Delta t \sum_{i=1}^s b_i 1^T k_i^p \\
 &= 1^T p^n + \Delta t \sum_{i=1}^s b_i 1^T (-\gamma D U_i p_i) \\
 &\quad - \Delta t \sum_{i=1}^s b_i 1^T (\gamma - 1) (-U_i D p_i - D U_i \tau_i + U_i D \tau_i + D \Phi_i) \\
 &= 1^T p^n + \Delta t \sum_{i=1}^s b_i (\gamma - 1) (u_i^T D p_i - u_i^T D \tau_i) \\
 \implies \frac{1}{(\gamma - 1)} (1^T p^{n+1} - 1^T p^n) &= \Delta t \sum_{i=1}^s b_i (u_i^T D p_i - u_i^T D \tau_i).
 \end{aligned} \tag{2.63}$$

The combination of (2.62) and (2.63) yields the conservation of total energy as the change in kinetic energy is balanced by the change in internal energy:

$$\left(\frac{1}{\gamma - 1} 1^T p^{n+1} + \frac{1}{2} (\sqrt{\rho u})^{n+1^T} (\sqrt{\rho u})^{n+1} \right) - E^n = 0. \tag{2.64}$$

□

2.3.2. A formulation in \sqrt{p}

The previous proof took advantage of the fact, that discrete mass is a quadratic quantity. However, it is possible to write the equations (2.43)-(2.45) in the variables $((\sqrt{\rho}), (\sqrt{\rho}u), (\sqrt{p}))$. In this formulation all physically conservative quantities, mass, momentum and total energy, are quadratic quantities. Written in $(\sqrt{\rho}), (\sqrt{\rho}u)$ and (\sqrt{p}) , the semidiscrete skew-symmetric Navier-Stokes equations are:

$$(\sqrt{p})_t = -\frac{1}{2}(\sqrt{R})^{-1}DRu, \quad (2.65)$$

$$(\sqrt{\rho}u)_t = -\frac{1}{2}(\sqrt{R})^{-1}(DRU + URD)u - (\sqrt{R})^{-1}Dp + (\sqrt{R})^{-1}D\tau, \quad (2.66)$$

$$(\sqrt{p})_t = \frac{1}{2}\sqrt{P}^{-1}(-\gamma DUp - (\gamma - 1)(UDp - DU\tau + UD\tau + D\Phi)). \quad (2.67)$$

In this formulation the proof of theorem 2 becomes trivial.

Proof. As Gauss-collocation methods conserve quadratic invariants, $y^T C y$, suitable matrices C_i have to be given so that mass, momentum and energy can be expressed in such a way. With $y = ((\sqrt{\rho}), (\sqrt{\rho}u), (\sqrt{p}))$ these matrices are:

$$1^T \rho = y^T \underbrace{\begin{pmatrix} 1 & 0 & 0 \\ 0 & 0 & 0 \\ 0 & 0 & 0 \end{pmatrix}}_{C_1} y, \quad (2.68)$$

$$(\sqrt{p})^T (\sqrt{\rho}u) = y^T \underbrace{\begin{pmatrix} 0 & \frac{1}{2} & 0 \\ \frac{1}{2} & 0 & 0 \\ 0 & 0 & 0 \end{pmatrix}}_{C_2} y, \quad (2.69)$$

$$\frac{1}{\gamma - 1}(\sqrt{p})^T (\sqrt{p}) + \frac{(\sqrt{\rho}u)^T (\sqrt{\rho}u)}{2} = y^T \underbrace{\begin{pmatrix} 0 & 0 & 0 \\ 0 & \frac{1}{2} & 0 \\ 0 & 0 & \frac{1}{\gamma - 1} \end{pmatrix}}_{C_3} y. \quad (2.70)$$

The identity $y^T C_i f(y) = 0$ holds for all three quantities and thus mass, momentum and energy are conserved. \square

An interesting note following this proof is that the matrix $C = C_1 + C_2 + C_3$ is symmetric and positive definite and thus can be used to define a norm $\|y\|_C = y^T C y$ on the discrete solution space. Following the proof 2.3.2 it

can be shown that given some initial data y_0 the $\|\cdot\|_C$ -norm of the discrete solution remains constant and equal to $\|y_0\|_C$, therefore proving

Corollary 3 (Stability of the method). *All Gauss-collocation methods applied to the skew-symmetric formulation of the Navier-Stokes equations written in $(\sqrt{\rho}), (\sqrt{\rho}u)$ and (\sqrt{p}) conserve the discrete norm of the solution and are therefore unconditionally stable on periodic grids.*

The above result shows that the scheme developed within this work is unconditionally stable. Under the assumption that the nonlinear system of equations within the implicit timestepping methods can be solved, the energy of solution is bounded for all times. However, this stability should not be confused with the physicality of the solution. Since the norm of the solution does not decrease either, any spurious oscillations introduced within the domain, e.g. in the vicinity of strong discontinuities, are not damped by the algorithm and will remain and propagate within the computational domain when no artificial, external filtering algorithms are applied. However, since the scheme itself is undamped, the artificial, numerical dissipation introduced is explicitly known and can be controlled in very specific ways. This allows, e.g. to reintroduce kinetic energy that is destroyed by the filtering back into the field as thermal energy. This way, the prospective filtering algorithm acts in a physical manner, converting kinetic to internal energy. As shown later in chapter 3, conservative shock-capturing and filtering algorithms can be applied selectively to the scheme with very good results.

2.3.3. Implementation of the implicit time integration scheme

The major disadvantage of the conservative time-integrators constructed for the skew-symmetric Navier-Stokes equations is their implicit nature. The application of the implicit Gauss-collocation schemes to the semidiscrete system requires solving the nonlinear system of equations (2.50),

$$k_i = f(t^n + c_i \Delta t, Y_i),$$

where Y_i is given as $Y_i = y^n + \Delta t \sum_j a_{ij} k_j$ and f represents the Navier-Stokes equations (2.18)-(2.19). As an explicit solution to this system is unknown, approximate iterative methods for nonlinear systems have to be employed. There exists a wide variety of literature on, and methods for, the iterative solution of nonlinear systems and an adequate discussion of this topic would

be out of scope for this work. Therefore, only a brief description of the method used for the computation of transonic shock-wave/boundary-layer interactions is presented alongside a short explanation as to why this method was chosen.

Within this work, the fixed-point method is used for the solution of the nonlinear system of equations. Given a starting vector x_0 , the iteration

$$x_{n+1} = f(x_n), \quad n = 0, 1, 2, \dots \quad (2.71)$$

is constructed until the residual $r = \|x_{n+1} - x_n\|$ reaches a given threshold $r < \epsilon$. If the function f is a contraction in the vicinity of the initial vector, the fixed-point iteration converges toward the fix point $x = f(x)$ linearly. The necessity of f being a contraction is not a problem in practical applications as the small timestep, in physical timescales, almost always guarantees the existence of a solution within the vicinity of the current flow field. However, the first order convergence is a major problem for the computational efficiency in actual application. A large number of iterations means a large number of evaluations of the right-hand side. Whereas explicit methods have a steady computational effort per timestep, with iterative methods the actual effort varies depending on the number of iterations needed. Table 2.1 shows a comparison of computational time between the explicit 4th order Runge-Kutta scheme and the implicit 4th order Gauss-collocation scheme for various CFL numbers and residuals. The data for the comparison stems from the computation of the one-dimensional skew-symmetric Navier-Stokes equations. While the exact data is dependent on the specific case, the general trend observed in table 2.1 is repeated for more sophisticated large-scale and three-dimensional computations. One observes that the computational effort of the implicit scheme is strongly dependent on the timestep Δt . One of the major advantages of implicit methods is their unrestricted timestep. Considering the results observed here, the actual timestep that can reasonably be chosen for large-scale computations is in the vicinity of CFL number 1 for accurate solutions to the nonlinear system with $r < 10^{-10}$. For higher residuals the implicit schemes can become more efficient than the explicit ones. In all simulations conducted within this work, the computational effort of the implicit scheme is about 2 – 3 times larger than for the explicit scheme. Thus more sophisticated methods with a higher order of convergence for the solution of (2.50) should be employed. The most commonly known of these methods is Newton’s method, which has order of convergence 2,

$$x_{n+1} = x_n - DF^{-1}(x_n)f(x_n). \quad (2.72)$$

$res \backslash CFL$	0.3	0.5	1.0	1.3	1.5
10^{-3}	0.76	0.76	0.76	0.76	0.76
10^{-7}	1.02	1.29	1.52	1.79	1.79
10^{-10}	1.3	1.5	2.36	3.5	4.7

Table 2.1.: Relation of computational time between the 4th order explicit Runge-Kutta method, t_{RK} , and the 4th order Gauss-collocation scheme, (t_{GC}). The fraction $(t_{RK})/(t_{GC})$ is displayed.

However, this method, and most methods with superlinear convergence require the construction and inversion of the Jacobian DF of f . In the discrete case, where DF is not explicitly given, and/or very large and distributed over multiple computing processes, this is a difficult prospect. The solution of (2.72) on a parallel system requires parallel solvers for matrix operations and was therefore not feasible within the context of this work. In contrast, the fixed-point iteration operates purely local and is therefore suited for massively parallel applications.

2.4. Boundary Treatment

Up to this point all the theory developed within this chapter has neglected boundary conditions. The reason for this is that the implementation of boundary conditions in discrete derivatives usually breaks the telescoping sum property. The symmetric, central difference stencil has to be modified near the boundary points since not all points necessary for the stencil

$$u'_i = \sum_{k=1}^m \alpha_k (u_{i+k} - u_{i-k}) \quad (2.73)$$

are available. At these m points different one-sided derivatives are employed. The effects of these alterations is best understood when considering an example take from [82]. The one-dimensional equation of mass in semidiscrete form,

$$\partial_t \rho = -DRu, \quad (2.74)$$

is discretized using second order central differences at the inner points and first order upwind schemes at the boundary, leading to:

$$D = \frac{1}{\Delta x} \begin{pmatrix} -1 & 1 & 0 & & 0 \\ -\frac{1}{2} & 0 & \frac{1}{2} & & \ddots \\ 0 & -\frac{1}{2} & 0 & \frac{1}{2} & \\ & & \ddots & & \\ & & -\frac{1}{2} & 0 & \frac{1}{2} & 0 \\ & \ddots & & -\frac{1}{2} & 0 & \frac{1}{2} \\ 0 & & & 0 & -1 & 1 \end{pmatrix}. \quad (2.75)$$

This matrix does not have the telescoping sum property at the points belonging to the boundary stencil. In the analytical case, $\partial_t \rho + \partial_x(\rho u) = 0$, the spatial integral over mass reduces the fluxes over the boundaries

$$\partial_t \int_{\Omega} (\rho) dx = -[\rho u]_0^L. \quad (2.76)$$

In the semidiscrete case, constructed with the above D , this is not the case:

$$\partial_t \mathbf{1}^T \rho = -\mathbf{1}^T D R u = -\frac{1}{\Delta x} \left(\frac{3}{2}(\rho u)_{M_1} + \frac{1}{2}(\rho u)_{M_1-1} - \frac{1}{2}(\rho u)_2 - \frac{3}{2}(\rho u)_1 \right). \quad (2.77)$$

Thus, even when velocity is zero at the boundary, e.g. at a solid wall, mass flux is present through the boundary. This phenomenon destroys the core concept of the skew-symmetric discretization, the accurate and physically correct representation of the conservation properties of the Navier-Stokes equations. A possible solution to this problem are the so-called *summation-by-parts* (SBP) differentiation matrices. The theory of these matrices goes back to Strand, [109], and they have recently been discussed in the context of split-symmetric or skew-symmetric schemes by Reiss et al, [82], and Fisher et al., [26].

2.4.1. Summation by Parts Derivatives

Definition 1. A SBP differentiation matrix D is defined as

$$D = W^{-1}Q, \quad (2.78)$$

with

$$Q + Q^T = B = \text{diag}(-1, 0, \dots, 0, 1), \quad (2.79)$$

$$1^T Q = (-1, 0, \dots, 0, 1)^T, \quad (2.80)$$

where W is a diagonal weight or norm matrix, with $\xi^T W \xi > 0$ for $\xi \neq 0$.

The quantities conserved are then given in the W -norm, $(\cdot, \cdot)_W$, and the fluxes collapse to the boundary points. Returning to the above example of the equation of mass, this leads to:

$$\rho_t = -DRu \iff W\rho_t = -QRu \quad (2.81)$$

$$\implies (1, \rho)_W = -1^T QRu = -(\rho u)_{M_1} + (\rho u)_1. \quad (2.82)$$

Here, the numerical fluxes reduce to the analytical fluxes. Using the tools provided by the SBP matrices, theorems 1 and 2 can be extended to include boundary conditions. These extensions are only given for the one-dimensional skew-symmetric Navier-Stokes equations. This is only done for ease of notation. They extend straight forward to multiple dimensions. The extension for the semidiscrete case is given by:

Theorem 3. *When D is a SBP differentiation matrix with a diagonal norm W , the following conservation properties hold true for the semidiscrete, skew-symmetric Navier-Stokes equations, (2.18)-(2.20), on non-periodic domains.*

$$\partial_t (1, \rho)_W = - [(\rho u)]_1^M, \quad (2.83)$$

$$\partial_t (1, \rho u)_W = - [\rho u^2 - p - \tau]_1^M, \quad (2.84)$$

$$\partial_t (1, E)_W = - \left[\rho u^3 + \frac{\gamma}{\gamma - 1} u p + u \tau + \Phi \right]_1^M. \quad (2.85)$$

The semidiscrete fluxes indeed are the analytical fluxes. In addition, kinetic energy is changed by convection only through the boundary fluxes.

The extension of theorem 2 involves the evaluation of fluxes at the Runge-Kutta substeps. But assuming a constant value is prescribed throughout those substeps, the expressions again reduce to the analytical ones.

Theorem 4. *On non-periodic grids, the skew-symmetric Navier-Stokes equations, (2.43)-(2.45), discretized using SBP differentiation matrices with a diagonal weight matrix W , the change in discrete mass, momentum and energy*

is given by:

$$[(\sqrt{\rho}, \sqrt{\rho})_W]_0^N = -\Delta t \sum_{n=0}^N \sum_{i=1}^s b_i (\rho u)_{M_1}^{n,i} + \Delta t \sum_{n=0}^N \sum_{i=1}^s b_i (\rho u)_1^{n,i}, \quad (2.86)$$

$$\begin{aligned} [(\sqrt{\rho}, (\sqrt{\rho}u)^N)_W]_0^N &= -\Delta t \sum_{n=0}^N \sum_{i=1}^s b_i [\rho u^2 - p - \tau]_{M_1}^{n,i} \\ &\quad + \Delta t \sum_{n=0}^N \sum_{i=1}^s b_i [\rho u^2 - p - \tau]_1^{n,i}, \end{aligned} \quad (2.87)$$

$$\begin{aligned} [(1, E)_W]_0^N &= -\Delta t \sum_{n=0}^N \sum_{i=1}^s b_i \left[\rho u^3 + \frac{\gamma}{\gamma-1} up + u\tau + \Phi \right]_{M_1}^{n,i} \\ &\quad + \Delta t \sum_{n=0}^N \sum_{i=1}^s b_i \left[\rho u^3 + \frac{\gamma}{\gamma-1} up + u\tau + \Phi \right]_1^{n,i}. \end{aligned} \quad (2.88)$$

Here s is the number of Runge-Kutta stages and the superscript (n, i) marks the quantity in the i -th Runge-Kutta substep of the n -th timestep. The b_i are the respective constants of the Runge-Kutta scheme. Again, convection only changes the kinetic energy through boundary fluxes. For the sake of brevity ad a constant timestep Δt is assumed.

Proof. The proof of both theorem 3 and 4 proceeds in the same way as in the periodic versions. The only difference being the two identities

$$\mathbf{1}^T Q \phi = \phi_{M_1} - \phi_1, \quad (2.89)$$

$$\phi^T (QV + VQ) \phi = (\phi v)_{M_1} - (\phi v)_1, \quad (2.90)$$

replacing

$$\begin{aligned} \mathbf{1}^T D \phi &= 0, \\ \phi^T (DV + VD) \phi &= 0, \end{aligned}$$

for arbitrary quantities ϕ and v and SBP differentiation matrices $D = W^{-1}Q$. Multiplying the Navier-Stokes equations with the weight matrix W and putting expressions (2.89) and (2.90) into the proofs of theorems 3 and 4 immediately results in the extended statements above. The identities (2.89) and (2.90) are constructed from the definition of SBP matrices as follows:

$$\mathbf{1}^T Q \phi = (-1, 0, \dots, 0, 1)^T \phi = \phi_{M_1} - \phi_1$$

and

$$\begin{aligned}
 \phi^T (QV + VQ) \phi &= \phi^T (VD^T + D^T V) \phi \\
 &= \phi^T (V(B - Q) + (B - Q)V) \phi \\
 &= \phi^T (VB + BV) \phi - \phi^T (VQ + QV) \phi \\
 \implies 2\phi^T (QV + VQ) \phi &= 2\phi^T VB \phi \\
 \implies \phi^T (QV + VQ) \phi &= (\phi v)_{M_1} - (\phi v)_1.
 \end{aligned}$$

□

This way, using SBP differentiation matrices, the analytical fluxes and conservation properties are retained. In practice, the SBP differentiation matrices are regular central difference matrices with modified stencils at the boundary points. The weight matrix W only modifies the scheme at these boundary points as well. Appendix B gives the matrices used for the simulations presented in this work. The SBP closure is used for all derivative terms, convective as well as viscous.

2.4.2. Implementation of Boundary Conditions

The use of SBP matrices yields schemes where the fluxes are defined by the boundary points alone. Boundary conditions are enforced by the addition of an external forcing term f to the equations of mass, momentum and energy. This method is illustrated using the equation of momentum,

$$\partial_t(\sqrt{\rho}u_\alpha) = -\frac{1}{2}(\sqrt{R})^{-1} (D_\beta R U_\beta + R U_\beta D_\beta) u_\alpha + W^{-1} f, \quad (2.91)$$

where viscous and pressure terms are neglected, and a moving wall boundary condition with fixed velocity $u = u_w$. In order to set the velocity equal to u_w , the method given in procedure 2.1 is employed. Some annotations to the above method are necessary. First, since f is just an additive term, the right-hand side of eq. (2.91) has to be evaluated only once. In explicit time integration schemes, the forcing vector f can be directly computed. In implicit schemes, like the Gauss-collocation methods, where the calculation of the new timestep involves iterative procedures, the forcing has to be iterated as well. In practice, calculating the new step $i + 1$ using the forcing f_i derived from the current iterationstep yields accurate results and a correct enforcement of the various boundary conditions.

Procedure 2.1: Implementation of Boundary Conditions

1. Calculate the uncorrected velocity u_{uc} at the timestep $(n + 1)$ using equation (2.91) without the forcing term f .
2. Set $f_b = \frac{1}{\Delta t}(u_w - u_{uc})$
3. Set $f = I_b f_b$, where I_b is an indicator function that sets f to zero at non-boundary points.
4. Calculate the correct velocity field using equation (2.91).

2.4.3. Boundary conditions in fluid dynamics

The physical boundary conditions necessary for the computations of wall bounded flow presented within this work are non-reflecting in- and outflow conditions as well as adiabatic no-slip walls. The in- and outflow conditions are set by performing a characteristic decomposition of the flow field, see e.g. Hirsch, [37,38], into Riemann invariants and then setting the inflowing characteristics to zero. At a subsonic outflow this method eliminates the inflowing, physical information on the flow characteristics at *infinity*. Dictating the pressure at the outlet to a specific value results in numerical reflections. To combat this phenomenon, methods developed by Poinso and Lele in their seminal paper on boundary conditions for the Navier-Stokes equations, see [79], are employed at the outflow. The adiabatic no-slip wall is described by boundary conditions that set all velocity components to zero as well as an energy flux of zero through the boundary.

2.5. Distorted Grids

In fluid dynamics, the ability to work on grid-spaces that are neither equidistant nor orthogonal is invaluable. When complex geometries are modeled this need is obvious. However, even simple geometries without curved surfaces necessitate grids that can be locally refined. Take for example the simulation of a turbulent boundary-layer. The computational domain is a rectangular cube. Consider an equidistant grid spacing. The small scale of the turbulence near the wall would force a very fine resolution of the grid. The small turbulent scales near the boundary dictate the grid spacing for the whole domain.

This is unfeasible. Therefore the ability for a numerical scheme to integrate non-uniform grids is of utmost importance. Compared to other discretization methods like finite-volumes or finite-elements, finite-difference schemes more restricted in their ability to deal with distorted grids. They are restricted to structured grids which can be described by a C^1 mapping of the unit cube. For many cases this restricted freedom on the form of the grid is enough. The case studied within this work, a turbulent boundary-layer impinging on an obstacle which can be described by a continuous function, is such a case. This section shows how the discrete formulation of skew-symmetric Navier-Stokes equations (1.12)-(1.14) can be applied on arbitrarily distorted grids as long as a suitable C^1 mapping from the unit cube exists. It will be shown that all the conservation properties derived previously apply on non-uniform grids. The key to this property will be to keep the skew-symmetric structure in the transformed equations. Schemes that preserve skew-symmetry on distorted grids go back to the work of Kok, see [47]. More recent work has been done by Morinishi et al. in [64]. For the matrix-driven discretization presented within this work, distorted grids have been the topic of work by Reiss and Sesterhenn, e.g. [81, 82].

Following the notation in [12] and [82], the physical coordinates are denoted as (x_1, x_2, x_3) and while the equidistant computational space $[0, 1]^3$ is written as (ξ_1, ξ_2, ξ_3) . There exists a continuous mapping $(\xi_1, \xi_2, \xi_3) \rightarrow (x_1, x_2, x_3)$ and thus the physical coordinates are a function of the computational ones. The local base vectors e_i are defined as the partial derivatives of said function:

$$e_i = \partial_{\xi_i} r, \quad r = (x_1, x_2, x_3). \quad (2.92)$$

The Jacobian of the grid transformation is

$$J = (e_1 \times e_2) \cdot e_3. \quad (2.93)$$

As written in Thompson et al., [43], the divergence on the physical domain can be expressed as

$$\frac{\partial u_i}{\partial x_i} = \frac{1}{J} \sum_{i,cy} \partial_{\xi_i} (e_j \times e_k) u \quad (2.94)$$

$$= \frac{1}{J} \sum_{i,cy} (e_j \times e_k) \partial_{\xi_i} u. \quad (2.95)$$

The notation (i, cy) denotes that the indices i, j, k change cyclical. Expression (2.94) is termed the *conservative* formulation while (2.95) is named *non-conservative*. The key to the extension of the skew-symmetric scheme to

distorted grids is to employ a combination of both variants of the divergence to retain the skew-symmetry of the convection operator:

$$(\partial_{x_\beta} \rho u_\beta \cdot + \rho u_\beta \partial_{x_\beta} \cdot) u_\alpha \quad (2.96)$$

$$= \frac{1}{J} \sum_{i,cy} (\partial_{\xi_i} (e_j \times e_k) u_\rho \cdot + (e_j \times e_k) u_\rho \partial_{\xi_i} \cdot) u_\alpha \quad (2.97)$$

The operator defined in (2.97) is skew-symmetric. The first derivative is written in the conservative form while the second term uses the non-conservative variant. Their combination yields the familiar skew-symmetric form for the convection operator. The formulation used for all the other spatial differences needs to be chosen with care to replicate the correct coupling of the equations and retain the telescoping sum property for all terms with a leading derivative. Therefore everything but the viscous terms is written in the conservative form. For the viscous part, the inner derivatives use the non-conservative formulation while the outer derivative is again conservative. A discretization of such a formulation of the skew-symmetric equations retains the same conservation properties as on equidistant grids. No direct proof is given since it contains no significant difference to those conducted for theorems 1, 2, 3 and 4. The full three-dimensional semi-discrete, skew-symmetric Navier-Stokes equations on distorted grids are given in appendix A.

2.6. Shock Treatment

Two main objectives guide the selection of a suitable shock filter for use with the skew-symmetric scheme. First, a selective treatment of the flow field is desired as to not add dissipation mechanisms to the turbulent parts of the flow field and alter the small scale turbulent structures. In addition, the filter should be conservative to retain the integrity of the conservative scheme and correctly predict the shock propagation. With this restrictions in mind, the conservative shock-capturing scheme of Bogey, Baily and de Cacqueray, [8], is chosen as the basis for the shock treatment. The description of the unmodified filtering procedure follows [8]. The algorithm is described in one dimension. For multi-dimensional cases, the procedure is applied successively in each spatial dimension.

The conservative form of the shock-capturing algorithm at grid node i is

given as

$$u_i^{sc} = u_i - \left(\sigma_{i+1/2}^{sc} D_{i+1/2}^{sc} - \sigma_{i-1/2}^{sc} D_{i-1/2}^{sc} \right), \quad (2.98)$$

with the varying filtering strength $\sigma \in [0, 1]$. The damping functions $D_{i\pm 1/2}^{sc}$ are given by

$$D_{i+1/2}^{sc} = \sum_{j=1-n}^n c_j u_{i+j}, \quad D_{i-1/2}^{sc} = \sum_{j=1-n}^n c_j u_{i+j-1}. \quad (2.99)$$

The filtering coefficients c_j are constructed from the non-conservative form of the filtering operation. Bogey et. al. use an optimized second order filter to construct the coefficients c_j . Details on the derivation of the coefficients can be found in their work. The coefficients are given, taking $c_{1-j} = -c_j$ into account, as:

$$c_1 = -0.210383 \quad (2.100)$$

$$c_2 = 0.039617. \quad (2.101)$$

Shock Sensor As per the goals defined for the shock-filter, the filtering magnitude σ should be nonzero only in the immediate vicinity of discontinuities. Bogey et. al. propose two different detectors using different flow quantities to estimate the filtering strength. This approach harkens back to Jameson, [42], and is based upon the magnitude of high wavenumber components of pressure or dilatation, $\Theta = \nabla \cdot u$. For a generic quantity φ this magnitude is computed in two steps. First the high wavenumber components of φ are computed using a high-pass filter according to

$$D\varphi_i = (-\varphi_{i+1} + 2\varphi_i - \varphi_{i-1})/4. \quad (2.102)$$

Then the magnitude is computed as:

$$D\varphi_i^{mag} = \frac{1}{2} \left[(D\varphi_i - D\varphi_{i+1})^2 + (D\varphi_i - \varphi_{i-1})^2 \right]. \quad (2.103)$$

The shock-sensor r_i is then computed in different ways for the pressure or the dilatation:

$$r_i^p = \frac{Dp_i^{mag}}{p_i^2} + \epsilon, \quad r_i^\Theta = \frac{D\Theta_i^{mag}}{c_i^2/\Delta x^2} + \epsilon. \quad (2.104)$$

Here, c_i^2 is the square of the speed of sound and $\epsilon = 10^{-16}$ is used to avoid round off problems. A threshold parameter r_{th} is then defined to switch the filtering on and set σ^{sc} :

$$\sigma^{sc} = \frac{1}{2} \left(1 - \frac{r_{th}}{r_i} + \left| 1 - \frac{r_{th}}{r_i} \right| \right), \quad (2.105)$$

$$\sigma_{i+1/2}^{sc} = \frac{1}{2} (\sigma_{i+1}^{sc} + \sigma_i^{sc}), \quad (2.106)$$

$$\sigma_{i-1/2}^{sc} = \frac{1}{2} (\sigma_i^{sc} + \sigma_{i-1}^{sc}). \quad (2.107)$$

This choice ensures a filtering magnitude of $0 < \sigma^{sc} < 1$ and especially $\sigma = 0$ for $r_i < r_{th}$. Therefore the filtering is switched off when pressure and dilatation show only small gradients. The threshold parameter has to be chosen specifically for each specific case but commonly resides in the range of $r_{th} \in [10^{-6}, 10^{-4}]$. A lower threshold value corresponds to a larger filtered region and in turn to a smoother solution which can overestimate the desired numerical dissipation. On the other hand a higher threshold value corresponds to only the regions of the strongest gradients being filtered. This may lead to the onset of numerical artifacts and spurious oscillations in the shock region when the applied dissipation is not sufficient to resolve the shock. The filter constructed this way is conservative as can be seen from the *telescoping sum property* of equation (2.98) and the definitions (2.99) and (2.106). On periodic domains the integral of a generic quantity ϱ is conserved by the filtering procedure (2.98) as it is given in flux form and

$$\sum_i \varrho_i^{sc} = \sum_i \left[\varrho_i - \left(\sigma_{i+1/2}^{sc} D_{i+1/2}^{sc} - \sigma_{i-1/2}^{sc} D_{i-1/2}^{sc} \right) \right] = \sum_i \varrho_i \quad (2.108)$$

holds.

Before implementing this filtering scheme into the conservative finite - difference code a few modifications to the scheme have to be discussed. These are the adaption of the scheme into the conservative framework, since in the skew-symmetric scheme, momentum is not conserved by first principle and thus momentum cannot be filtered without modification. Second is the treatment of boundaries as their treatment is not discussed in [8]. Last is the choice of variable for the shock detection. Due to the conservative nature of the filter, direct application of the scheme to the conserved quantities mass, momentum and total energy would keep those at their previous level. However, application of the filter to the momentum generally decreases the kinetic

Procedure 2.2: Conservative Filtering Algorithm

1. Compute the shock sensor σ_{sc} .
2. Compute the variables ρ , (ρu_i) and $e = \frac{1}{\gamma-1}p$.
3. Apply the filtering procedure (2.98) to the density ρ .
4. Compute the kinetic energy $E_{kin}^{pre} = \frac{1}{2}(\rho u_i)^2$ at each node.
5. Apply the filtering procedure to the momentum (ρu_i) .
6. Compute the kinetic energy $E_{kin}^{post} = \frac{1}{2}(\rho u_i)^2$ from the filtered momentum $(\rho u_i)^{sc}$.
7. Add $\Delta E_{kin} = E_{kin}^{pre} - E_{kin}^{post}$ to the internal energy e .
8. Apply the filtering procedure to the internal energy e .

energy of the fluid. While filtering ρE may keep the total energy constant it obscures the specific change in kinetic and internal energy. Since great effort was taken to ensure the correct change in kinetic energy within the numerical scheme, it is highly undesirable to introduce this with the filtering algorithm. Therefore the algorithm given in procedure 2.2 is applied at each time step for shock-filtering purposes. When applied this way, the filtering procedure conserves the total energy by converting the kinetic energy destroyed during the filtering to internal energy. It acts like a physical dissipation mechanism, which converts kinetic to internal energy. Through this procedure, the filtering algorithm acts consistent with the intent of the spatial discretization of the skew-symmetric finite-difference method.

The treatment of boundary points with the filtering algorithm is not covered by the procedure described above. The expression for the filtering magnitude and the damping functions are not defined at the boundaries. Since it is assumed that no shock will reach the boundaries in the forthcoming simulations described in this thesis, the following easy extension is employed at the boundary points. As the boundary-layer separates the wall from the shock in the *SBLI* case and the viscous effects smooth out the discontinuity there, this assumption seems to be justified. All quantities at the boundary points

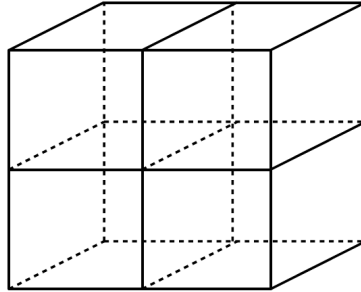


Figure 2.1.: Domain decomposition of a three-dimensional domain in two directions.
Figure taken from [105]

are set to the values at the nearest off-the-boundary points:

$$D\varphi_1 = D\varphi_2, \quad D\varphi_N = D\varphi_{N-1}, \quad (2.109)$$

$$\sigma_1^{sc} = \sigma_2^{sc}, \quad \sigma_N^{sc} = \sigma_{N-1}^{sc}, \quad (2.110)$$

$$D_{1\pm 1/2}^{sc} = D_{2\pm 1/2}^{sc} = D_{3\pm 1/2}^{sc}, \quad (2.111)$$

$$D_{N\pm 1/2}^{sc} = D_{N-1\pm 1/2}^{sc} = D_{N-2\pm 1/2}^{sc}. \quad (2.112)$$

As for the choice of variable, on which to base the shock-sensor, the two common choices are pressure p and dilatation $\Theta = \nabla \cdot u$. In general, pressure is the common choice of shock-sensor, e.g. [8]. However, for the simulation of turbulent flows, this is an inadequate choice, since the pressure fluctuations within the turbulent flow field often reach high enough amplitudes to activate the shock detector and thus falsify the turbulence structures in the simulation. This prompts the choice of dilatation as the governing parameter in applications studied within this work.

2.7. Parallel Implementation

Due to the nature of turbulent flow and the large difference in spatial and temporal lengthscales, direct numerical simulations of the Navier-Stokes equations require a very large number of grid points to completely resolve the

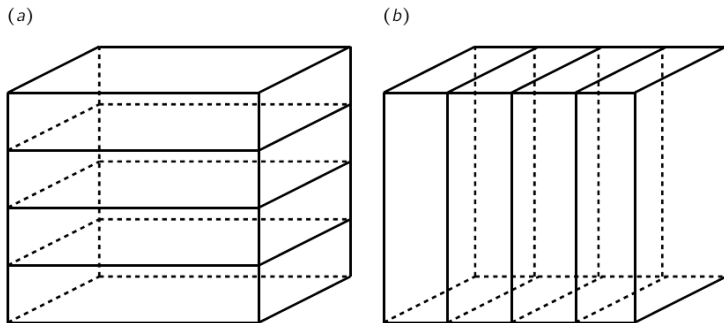


Figure 2.2.: Transformation of the decomposed domain in x- and y-direction. (a) slices in x-direction, (b) slices in y-direction. For the decomposition in z-direction, such blocks are concatenated in the third dimension. Figure taken from [105]

physics of the flow. Since the lengthscales depend on the Reynoldsnumber, the ratio between viscous and convective forces, the size of the grid also depends on the Reynoldsnumber. At the time of writing, the largest direct numerical simulations of wall-bounded turbulence need grid sizes of the order of $\sim 2 \cdot 10^9$ gridpoints to resolve Reynoldsnumbers of order $Re \sim 3 \cdot 10^4$, see [74]. Such computational domains necessitate the use of massively parallel high performance systems to distribute the computational load evenly between a large number of processes. The code employed within is parallelized using the domain decomposition approach, see fig. 2.1. Using this approach, each process solves the Navier-Stokes equations only on a small part of the original domain. However, communication between the processes is indispensable. For example, when calculating the derivatives the differentiation stencil at the boundary points of each process needs information on points in the neighboring process. This implementation of the code on massively parallel computing centers uses the Message Passing Interface (MPI) for the inter-process communication. The three-dimensional domain is decomposed in all three physical directions. Since the inter-block communication is almost exclusively required for the computation of discrete derivatives, the following communication approach, based on work by Edison and Erlebacher, see [23], is used. The data in the decomposed domain is rearranged, so that continuous slices in the desired direction appear without changing the total amount

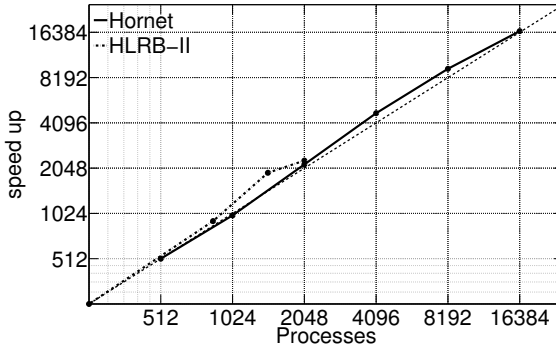


Figure 2.3.: Parallel scaling of the code on two different computing centers. A large-scale job using 10^9 gridpoints is used for the scaling.

of grid points per processor. Figure 2.2 illustrates the mechanism in x- and y-direction. In this way, each process contains the entire data in the desired direction. This method guarantees a balanced computational burden for each process and avoids bottlenecks.

The performance and scalability of the present algorithm on two different high performance computing centers, the *HLRS-Hornet* cluster and the *HLRB-II* system is plotted in figure 2.3. For testing purposes, a large-scale job, using over 10^9 gridpoints is used. The domain size was kept constant while the number of processes was increased. The code shows linear scaling up to 16384 cores. A similar test case, where the number of gridpoints per process was kept constant displays the same behavior. The *HLRB-II* system at the Leibniz Rechenzentrum uses a SGI ALTix 4700 architecture while the *HLRS-Hornet* Cluster in Stuttgart is a Cray XC40 machine. The same linear scaling behavior on these two different systems is encouraging.

Validation of the Method

This chapter deals with the practical validation of the conservative skew-symmetric finite-difference scheme constructed in the previous chapter. As the aim of this work is the computation of turbulent shock-wave/boundary-layer interaction, the test cases are chosen with this goal in mind. Following a short section validating the basic conservation properties of the method, test cases are studied that deal with the main difficulties in the simulation of shock-wave/boundary-layer interactions. These are the treatment of shocks, the simulation of small-scale compressible turbulence and the accurate representation of turbulent boundary-layers including the generation of turbulent inflow data. After a brief section on conservation properties, the classical Lax-Liu shock cases, see [49], are used to validate the accurate representation of inviscid shock systems. Simulations of decaying and forced isotropic turbulence at compressible Mach numbers show that the present code is capable of accurately computing small-scale turbulence at high Mach numbers. Within this section, a new, conservative forcing algorithm for isotropic turbulence is crafted. Lastly, simulations of a turbulent flat-plate boundary-layer are compared with existing direct numerical simulations. The boundary-layer section includes notes on two different methods for the generation of realistic turbulent inflow data and a discussion of their respective strengths and weaknesses. The order of accuracy for all differentiation schemes used in this chapter and part II is checked for the skew-symmetric, fully conservative formulation of the Navier-Stokes equations and displayed in figure 3.1. Note that parts of

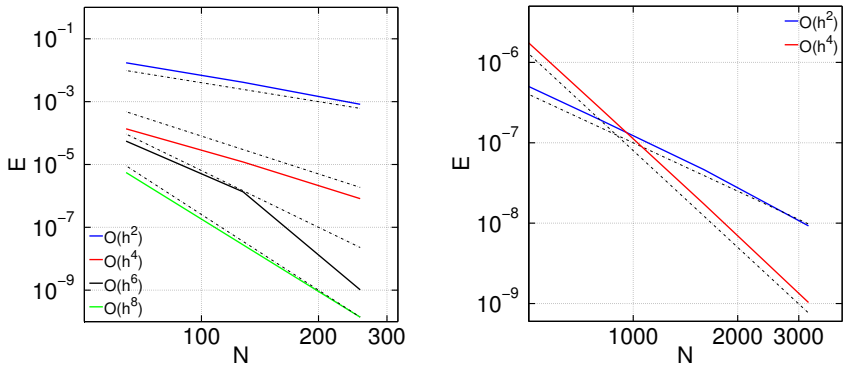


Figure 3.1.: Order of convergence in space (left) and time (right). Standard central differences of order 2-8 are used for the spatial discretization of the conservative, skew-symmetric Navier-Stokes equations. The temporal convergence is given for Gauss-collocation methods of order 2 and 4.

section 3.1 and 3.3 have already been published by the author in [12].

3.1. Conservation Properties

Before venturing to more complicated test settings, the conservation properties of the skew-symmetric formulation are checked and validated in a simple, one-dimensional setting. This is done by checking the temporal evolution of the relative change in the conserved quantities of mass, momentum and total energy. As mentioned in chapter 2.3, the conservation is only perfect if the implicit, nonlinear system of equations arising in the application of the Gauss-collocation methods is solved exactly. As this cannot be done in practice, the conservation properties are investigated with respect to the accuracy of the solution of said system of nonlinear equations. Since the use of implicit time integrators is not feasible in all circumstances, mainly when heavy restrictions on computational efficiency exist that outweigh the increased numerical stability, conservation properties of the skew-symmetric formulation of the Navier-Stokes equations, written in $(\sqrt{\rho}, \sqrt{\rho}u, p)$, are checked for non-conservative, explicit time-integrators. Furthermore it will be argued, that the skew-symmetric formulation, even with non-conservative time integra-

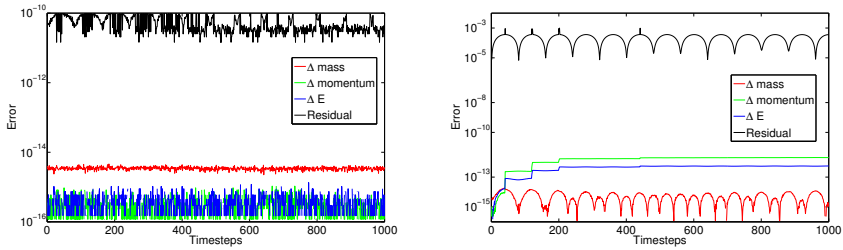


Figure 3.2.: Relative change in the conserved quantities and the timestepping residual for the 1-dimensional Navier-Stokes equations. Terminal conditions - left: $res \leq 10^{-10}$; right: $res \leq 10^{-3}$. Plot taken from Brouwer et al.m [12].

tion, has advantages when compared to the usual convective formulation of the equations of flow.

3.1.1. Navier-Stokes Equations with Smooth Initial Data

The setup for this test case is rather simple and easily reproducible. The skew-symmetric Navier-Stokes equations written in $(\sqrt{\rho}, \sqrt{\rho}u, p)$, (2.34)-(2.36), are discretized using standard central differences of order 8 in space and the Gauss-collocation method of order 4 in time, the implicit time-integration is handled using a simple fixpoint iteration. The initial conditions on the periodic domain $[0, 2\pi)$, are set to:

$$\begin{cases} \rho &= 1.2, \\ u &= 1 + \sin(x) + 0.3 \sin(4x + \pi/3), \\ p &= 100000. \end{cases} \quad (3.1)$$

The system is then run for 1000 timesteps with a CFL number of 0.3. Figure 3.2 shows the relative change in mass, momentum and energy when a residual of $r < 10^{-10}$ is employed for the fixed-point iteration. Although the accuracy of the solution of the nonlinear system is far away from 10^{-16} , momentum and energy change is down to machine precision. The rate of change of mass is about one order of magnitude higher, but still negligible with a magnitude of 10^{-15} . For the fixed-point iteration, low residuals imply a high number of iterations. Therefore low residuals also directly imply a high computational effort. Consequently, it is of interest how the conservation changes when a

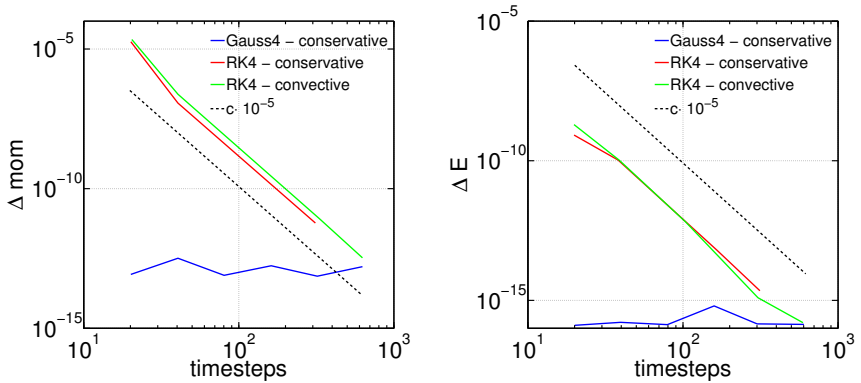


Figure 3.3.: Comparison of the convergence properties in the conserved quantities between the full skew-symmetric scheme, non-conservative time integrators applied to the skew-symmetric formulation and the convective formulation for smooth solutions. left: momentum; right: total energy

higher residual is applied. Figure 3.2 also depicts the same quantities with a residual of $r < 10^{-3}$. The figure contains three interesting points. First and most important, while the residual is larger by 7 orders of magnitude, conservation only goes down by 3 orders of magnitude. This verifies the robustness of the present formulation with respect to the specifics of the implementation of the Gauss-collocation method. Furthermore, large jumps in the relative change of all quantities can be traced to instances of untypically large residuals. Lastly, the magnitude of the conservation of mass seems to be unaffected by the residual while the rate of change in momentum and energy increases by a few orders of magnitude. This is most likely due to the direct summation-by-parts property of the equation of mass. Contrary to mass, conservation of momentum and energy is due to consistent coupling of the two equations which makes these properties more sensitive to inconsistencies in their solution.

3.1.2. Skew-Symmetric Finite-Differences with Non-Conservative Time-Integrators

This section deals with the conservation properties of non-conservative time integrators applied to the skew-symmetric formulation of the Navier-Stokes

equations. In addition these results are compared to the conservation properties of the *convective* formulation of the momentum equation in primitive variables,

$$u_t + uu_x + \frac{p_x}{\rho} = \frac{\partial_x \tau}{\rho}. \quad (3.2)$$

The conservation study is conducted by observing the convergence to perfect conservation when the timestep, Δt , is reduced. The same setup as in the previous section is used and simulated up to a final time of $t_0 = 0.0012$, where mass, momentum and total energy are compared to their initial values. Three different discretizations are compared with each other. First, the fully conservative scheme developed within this thesis, using a *4th* order Gauss-collocation method for time-integration. Second, the same skew-symmetric formulation, but with the explicit *4th* order Runge-Kutta method, is used for the time integration. Lastly, the explicit RK4 method applied to the above mentioned, convective formulation of the Navier-Stokes equations in primitive variables (ρ, u, p) . Figure 3.3 depicts the convergence behavior for momentum and energy. As expected, the conservation of momentum and energy is independent of the temporal resolution for the fully conservative setup. Both conservative and convective variants of the Navier-Stokes equations show the same behavior. Conservation error decreases with $\mathcal{O}(\Delta t^{-5})$. This coincides with the local order of accuracy of the Runge-Kutta methods employed for the tests. While the figure shows that explicit time integrators can achieve the same accuracy in conservation as the fully conservative implicit method this applies very severe restrictions on the timestep. The initial conditions for this test, given in (3.1), are dominated by very few, large scale structures. It is interesting to observe the conservation when the solution is enriched with small-scale structures with a high temporal frequency, essentially adding *turbulence* to the flow field. To mimic these conditions, a sinusoidal wave with an amplitude of $0.1u$ and a wavelength of $4\Delta x$ is added to the base flow. Figure 3.4 displays the results of this case. Comparing figures 3.3 and 3.4 shows only one discrepancy in the convergence plots. The convective formulation shows a stagnation in the convergence of total energy. The error does not decrease further after a certain point. The same is not true for the Runge-Kutta discretization of the skew-symmetric formulation. This behavior can be explained in the following way. The skew-symmetric formulation developed in chapters 2.2 and 2.3 mirrors the correct, analytical rate of change of kinetic to internal energy. Total conservation is then achieved by the consistent treatment of kinetic and internal energy. This physical transfer mechanism is not

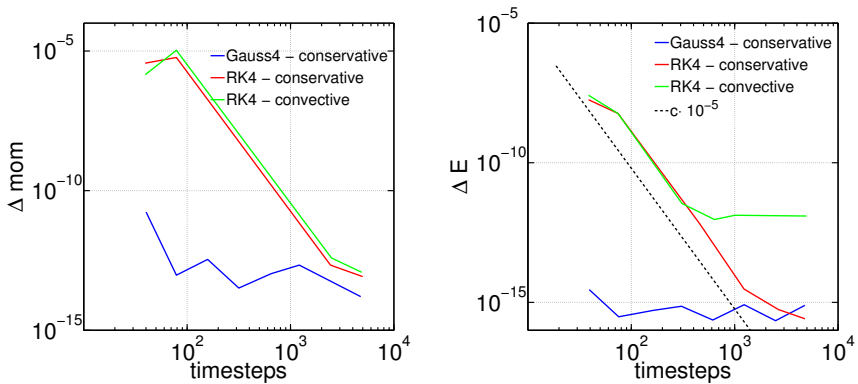


Figure 3.4.: Comparison of the convergence properties in the conserved quantities between the full skew-symmetric scheme, non-conservative time integrators applied to the skew-symmetric formulation and the convective formulation for high-frequency solutions. left: momentum; right: total energy

present in most convective formulations. Thus physical information might be lost and negatively effect the conservation of total energy at a certain point.

This behavior, in combination with the increased stability offered by the skew-symmetry, suggests that the skew-symmetric finite-difference formulation of the Navier-Stokes equations has further applications in situations even when implicit time integration is not feasible.

3.2. Lax-Liu Shock Test Cases

In their 1998 paper *Solution of two-dimensional Riemann problems of gas dynamics by positive schemes*, [49], Lax and Liu present a series of 19 different test cases for the Euler equations for polytropic gas. The test cases are constructed by dividing the unit square evenly into 4 quadrants and choosing uniform initial data in each quadrant such that only a single wave, one-dimensional shock, a one-dimensional rarefaction wave or contact discontinuity appears at each interface. Lax and Liu employ *positive* finite-volume methods to calculate their reference solutions to the test cases. These schemes naturally obey the Rankine-Hugoniot conditions and compute the correct shock-speed, however, these schemes introduce artificial numerical damping

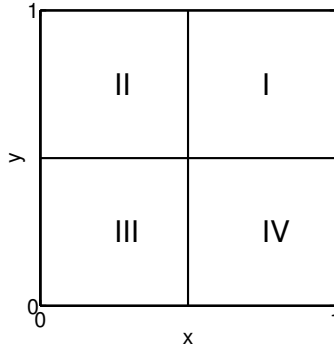


Figure 3.5.: left: Schematic view of the setup for the test cases of Lax and Liu, [49]

that can be hard to predict and may affect the solution.

The following section is devoted to the shock-capturing methodology that is employed in conjunction with the conservative skew-symmetric scheme to handle shock afflicted systems.

3.2.1. Results

Two cases of the Lax & Liu suite are picked to demonstrate situations containing shocks, complex vortical structures as well as rarefaction waves. The cases picked are configurations 11 and 15 from [49]. The unit square is decomposed in 4 quadrants, see figure 3.5, and discontinuous initial conditions are described in each quadrant. Initial conditions for both cases are given in table 3.1. Direct comparison with the results of Lax & Liu is difficult since they only give nondescript contourlines of density at a specific time. To keep

Case	11				15			
Quadr.	I	II	III	IV	I	II	III	IV
u	0.1	0.8276	0.1	0.1	0.1	-0.6259	0.1	0.1
v	0	0	0	0.7276	-0.3	-0.3	-0.3	0.4276
ρ	1	0.5313	0.8	0.5313	1	0.5197	0.8	0.5313
p	1	0.4	0.4	0.4	1	0.4	0.4	0.4

Table 3.1.: Initial conditions for test cases 11 and 15 taken from [49]

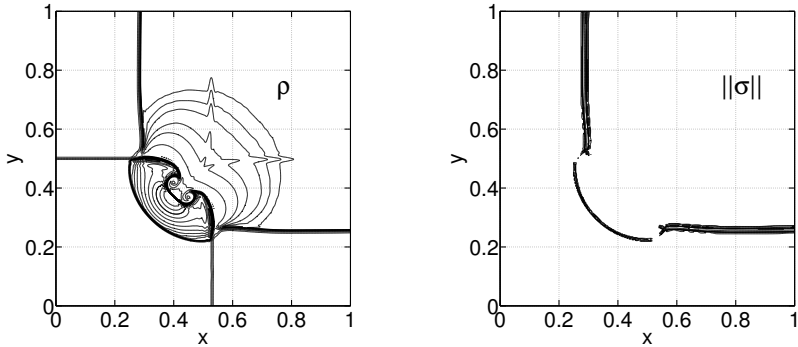


Figure 3.6.: Contourplot for Lax-Liu case 11 at $t = 0.3$; left: density, right: $\|\sigma\|$.

the simulation as similar as possible, the spatial and temporal stepsizes are kept identical. The 2-dimensional inviscid Euler-equations are discretized on the unit square $[0, 1]^2$ using 400 equidistantly spaced gridpoints in each direction. The timestep is fixed at $\Delta t/\Delta x = 0.3$ for case 11 and $\Delta t/\Delta x = 0.2$ for case 15. For the spatial discretization, 6th order central differences with the *summation by parts* property are employed while the 4th order Gauss-collocation method is used for timestepping. For both simulation, the threshold parameter r_{th} is set to 10^{-5} resulting in rather sharp interfaces at the shockfronts. Figure 3.6 shows a contourplot of density at $t = 0.3$. The plot shows great accordance with the results in [49]. Indeed, the simulations match the theoretical shock speeds, computed using the Rankine-Hugoniot conditions, perfectly. Apart from the density contours, figure 3.6 depicts the filtering strength, $\|\sigma\|$. It can be observed that the filter is only active at the sharp interfaces of quadrants *I* and *II* as well as *I* and *IV*. The vortical structure entering zone *III* from the center is not filtered at all. Figure 3.7 depicts contourlines of the density and the filtering strength for the test case no. 15 in [49]. Again, the picture agrees well with the original simulation. In addition to the observations made for the case 11, fig. 3.7 shows a rarefaction wave between quadrants *I* and *II* whose spread agrees with theory and the original simulations. Again, as evident from the filtering strength, only the very sharp interface between quadrants *I* and *IV* is filtered, highlighting the highly selective nature of the filtering algorithm. All in all, the comparison with these classical test cases shows that the conservative skew-symmetric scheme is able to handle strong discontinuities and predicts the correct shock

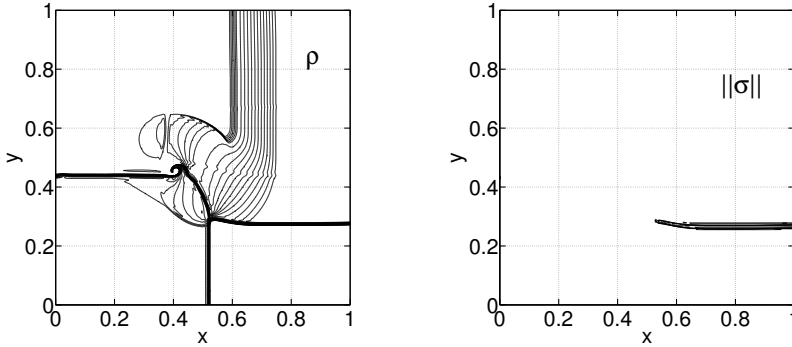


Figure 3.7.: Contourplot for Lax-Liu case 15 at $t = 0.2$; left: density, right: $\|\sigma\|$.

propagation speed .

3.3. Isotropic Turbulence

This section deals with various simulations of compressible, isotropic turbulence. The previous tests in this chapter have validated the conservation properties of the scheme developed in chapters 2.2 and 2.3 as well as its ability to correctly predict shocks. The cases presented here verify whether turbulence in high Reynolds- and Mach number flows can be accurately represented by the conservative, skew-symmetric scheme. To this aim, simulations of both decaying and forced isotropic turbulence are processed and compared to reference simulations found in the work of Samtaney et al. , [91], as well as Wang et al., [121]. The computation of decaying turbulence allows the validation of correct dissipation mechanisms via the energy spectra and decay rates of several quantities. In contrast, the forced simulations are done at high subsonic turbulent Mach numbers where strong velocity fluctuations manifest as shocklets and correct results rely on the interaction of strong discontinuities and turbulence. Note that the simulations presented in this section have been reported and published by the author in [12].

Computational Setup All simulations in the following sections are done using the same basic setup. The computational domain $[0, 2\pi]^3$ is discretized using N^3 gridpoints placed equidistantly in all 3 dimensions. The underlying

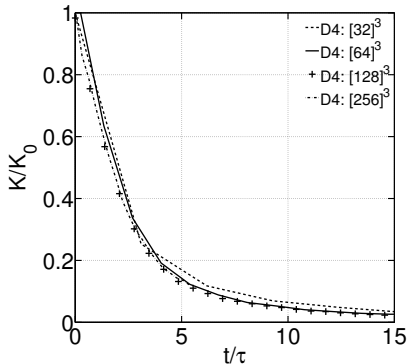


Figure 3.8.: Decay of normalized kinetic Energy K/K_0 for runs of configuration D4 of [91] compared for different grid sizes. Initial $M_t = 0.3$ and $Re_\lambda = 72$

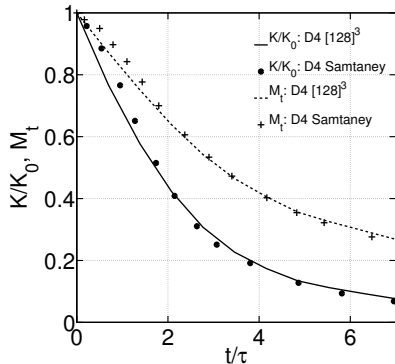


Figure 3.9.: Decay of normalized turbulent Mach number M_t/M_0 and normalized kinetic energy K/K_0

equations for compressible flow are the 3–dimensional Navier-Stokes equations in fully conservative form as derived in section 2.3 and given in appendix A. For the convective terms, 8th order central differences are applied while the friction terms are discretized using 5th order *non symmetric* schemes. As noted in 2.3, corollary 1, the viscous terms can be discretized in such a manner without violating conservation properties. In addition, switching to upwind schemes for the viscous part of the equations has an additional stabilizing influence on the simulations. When using all central schemes, the simulations developed small-amplitude, small-wavelength oscillations that had to be removed via filtering. With the addition of the modified discretization of the viscous terms, these oscillations disappear. For the temporal discretization the implicit 4th order Gauss-collocation Runge-Kutta method is used.

3.3.1. Decaying Isotropic Turbulence

For the verification of dissipation mechanisms, simulations of decaying, compressible turbulence are run. The specifics of these simulations follow those of Samtaney et al. in [91], in particular case D4 discussed in said publication.

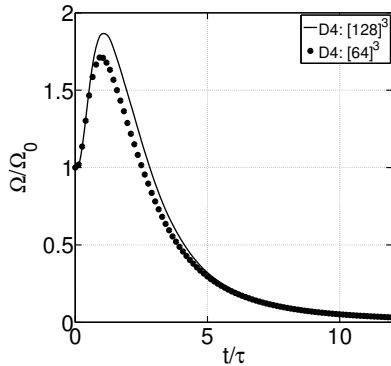
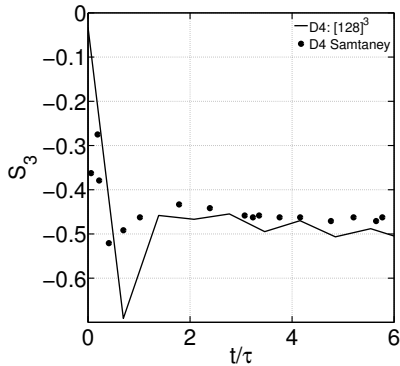


Figure 3.10.: Time evolution of velocity derivative skewness $S_3 = \langle (\partial u_1 / \partial x_1)^3 \rangle / \langle (\partial u_1 / \partial x_1)^2 \rangle^{3/2}$

Figure 3.11.: Normalized enstrophy Ω / Ω_0 for a simulation of configuration D4 of [91]. Initial $M_t = 0.3$ and $Re_\lambda = 72$

The initial turbulent Mach number is set to $M_t = 0.3$. In this regime, the ratio ρ' / ρ_0 of density fluctuations is not negligible and compressibility effects influence the flow. An initial condition for the velocity field is constructed using the method of Rogallo, see [86], to match the prescribed velocity spectrum:

$$E(k) = Ak^4 \exp(-2k^2/k_0^2), \quad (3.3)$$

where k_0 is the peak wavenumber of the spectrum and the constant A is set to obtain the desired initial turbulent Mach number. Initial density and pressure fluctuations are set to zero. This produces a nonphysical initial state of the flow. However, as discussed in [91], after a short initial transient, the simulation is indistinguishable from one realized with a more sophisticated initial state. Choosing $A = 49.5$ and $Re = 465$ yields the desired initial turbulent Mach number $M_t = 0.3$ and $Re_\lambda = 72$. The timestep used is set to $\Delta t / \tau = 0.002$ where τ is the characteristic vortex timescale calculated at $t = 0$.

Before going into detail on the results, a test on grid dependence of the statistics is performed. The above setup is computed using varying gridsizes

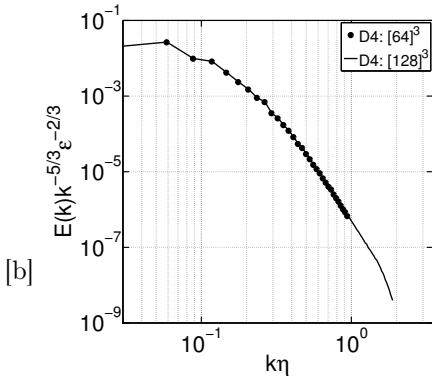


Figure 3.12.: Kinetic energy spectra $E(k)$ for simulations with $[64]^3$ and $[128]^3$ points, taken at $t/\tau \approx 4$

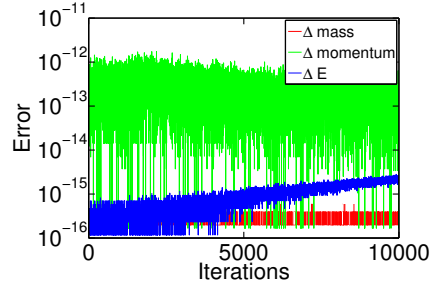


Figure 3.13.: Relative change in the conserved quantities using 4th order Gauss-collocation methods for long timeframes - case D4, [91]

ranging from $[32]^3$ to $[256]^3$. Figure 3.8 depicts the normalized decay of kinetic energy for different grid resolutions. Besides the smallest resolution of $[32]^3$, all curves collapse onto each other. After gaining confidence in the grid independence of the results, the rate of decay of Mach number and kinetic energy is depicted in figure 3.9. Comparison with Samtaney et al. show perfect match after an initial transient, caused by the non-physical initial conditions, lasting until $t/\tau \approx 1 - 1.5$. The same can be observed in the velocity derivative skewness displayed in fig 3.10. A comparison of the enstrophy decay between different gridsizes is shown in figure 3.11.

A quantity of great interest in direct numerical simulations of turbulence is the kinetic energy spectrum. Figure 3.12 shows that the decay of kinetic energy is: (a) consistent with different grid resolutions and (b) follows the expected rate of decay with wavenumber. The results show a small inertial region with a $k^{-5/3}$ rate of decay as well as large dissipation region with the characteristic $k^{-7/2}$ decay. Due to the relatively small Reynolds number at the time the spectra were taken, the dissipation region is much larger

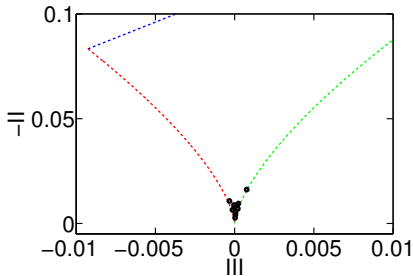


Figure 3.14.: Invariant map of the anisotropy tensor for forced compressible turbulence at $M_t = 0.15$

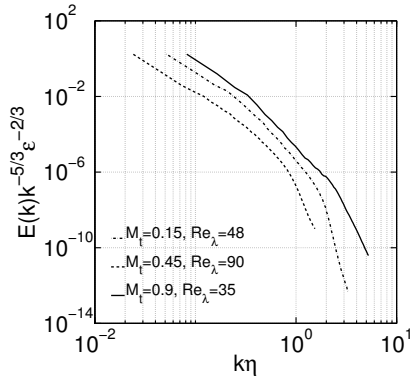


Figure 3.15.: Normalized kinetic energy spectrum $E(k)$ for forced isotropic turbulence at different Mach and Reynolds numbers

compared to the inertial region. Again, following an initial transient, both simulation agree. Figure 3.13 shows the relative change in the conserved quantities during the simulation of decaying turbulence. As expected, changes are down to machine precision over the entire run.

The conservative finite-difference approach compares favorably with the results in [91], where 10th order compact schemes were used. Thus the scheme demonstrates its ability to correctly capture turbulence and dissipation mechanisms in the lower turbulent Mach number regime.

3.3.2. Forced Compressible Isotropic Turbulence

The next step in the validation of the scheme for compressible turbulence are interactions of turbulence with strong discontinuities and shocks. Therefore simulations of forced, isotropic turbulence at high subsonic Mach numbers, up to $M_t = 0.9$, are performed. At these Mach numbers velocity fluctuations are strong enough that interactions between turbulence and shocklets occur. These high Mach numbers are achieved by applying a forcing algorithm, adapted from work done by Wang et al. in [121], at each timestep. The forcing algorithm keeps the energy content in the first two wavenumber

shells constant without changing total mass or energy within the flow. Before looking at results at these high Mach numbers, the forcing algorithm is presented and validated. To handle the occurring shocklets, the conservative shock-capturing scheme developed in section 2.6 was applied to all forced simulations, done at a resolution of $[128]^3$, in combination with a conservative 11-point filter, also from [8], to remove grid oscillations. While the shock-capturing scheme uses a detector function based on the flow dilatation, the grid oscillations were removed every 100 timesteps with a filtering strength of $\sigma_s = 0.1$. To preserve mass, energy and momentum correctly through the filtering procedure, the same modified filtering procedure, described in section 2.6, is applied to the 11-point filter as to the shock-detector. Therefore, both filtering procedures do not violate the conservation and convert kinetic energy into internal energy.

Forcing Algorithm The following forcing algorithm is applied after each discrete timestep is given as procedure 3.1.

To check whether this artificial forcing of the flow destroys its isotropy or the energy dissipation cascade, a simulation with a relatively low turbulent Mach number is performed and checked for isotropy via the invariant map of the anisotropy stress tensor. The energy constant E_1 is set to $E_1 = 1100$ while E_2 is chosen according to the $k^{-5/3}$ decay law. An initial Reynolds number of $Re = 480$ leads to a statistically steady flow with $M_t = 0.15$ and $Re_\lambda = 48$. According to the anisotropy stress tensor, whose invariants are plotted in fig. 3.14, the forcing algorithm does preserve the isotropy of the flow. The kinetic energy spectrum, see figure 3.15, adheres to the expected $k^{-5/3}$ and $k^{-7/2}$ decay. Of note is the abrupt decay of the spectrum terminating the dissipative region. The onset of this rapid decay corresponds with the damping function of the conservative filter and shows little dependency on filtering strength but rather on filtering frequency. The decay due to numerical dissipation is independent of resolution as the onset of the decay collapses to same point when $E(k)$ is plotted over $k\Delta x$ for different resolutions.

After this setup, the forcing algorithm is applied to reach steady states at higher turbulent Mach numbers. Two different steady states are computed. The first one has a high Reynolds number of $Re_\lambda = 90$ and a lower Mach number of $M_t = 0.45$. The other one being characterized by a turbulent Mach number of $M_t = 0.9$, and $Re_\lambda = 35$. The low Mach number state is achieved by setting $E_1 = 8000$ and $Re = 800$, the second one with an $E_1 = 30000$ and $Re = 50$. The time-averaged spectra of the two simulations, together

Procedure 3.1: Forcing Algorithm for Isotropic Turbulence

1. Compute the discrete Fourier transform $\widetilde{\rho u}_i$ of ρu_i .

2. Compute the energy spectrum $E(k)$ of $\widetilde{\rho u}_i$.

3. Set the forcing field for the momentum in Fourier space to:

$$\widetilde{f}_i|_{0.5 < k < 1.5} = (1 - \alpha_1)\widetilde{\rho u}_i, \quad \widetilde{f}_i|_{1.5 < k < 2.5} = (1 - \alpha_2)\widetilde{\rho u}_i, \quad \widetilde{f}_i|_{k > 2.5} = 0,$$

where $\alpha_1 = \sqrt{E(1)/E_1}$, $\alpha_2 = \sqrt{E(2)/E_2}$ and E_1, E_2 are the desired energy values in the first two wavenumber shells.

4. Compute the divergence of the forcing field \widetilde{f} and set $\widetilde{f}_\rho = \text{div}(\widetilde{f})$.

5. Compute the inverse Fourier transform of the forcing fields and set:

$$\begin{aligned} f_\rho &= iFFT(\widetilde{f}_\rho), \\ f_{\rho u_i} &= iFFT(\widetilde{f}_i). \end{aligned}$$

6. Compute the forcing field for the internal energy as $f_e = -u_i \cdot f_{\rho u_i}$.

7. Set the new flow field as follows:

$$\begin{aligned} \rho &= \rho + f_\rho, \\ \rho u_i &= \rho u_i + f_i, \\ e &= e + f_e. \end{aligned}$$

with the simulation used for validation of the forcing algorithm, is displayed in figure 3.15. The simulations with higher Reynolds number display a larger inertial region combined with a dissipative regime that is less pronounced when compared to the previous simulations of decaying turbulence, see 3.12.

Finally, 2–dimensional slices of density and vorticity are shown in figures 3.16 - 3.19. Starting with the lower Mach number simulation, the density field in 3.16 shows large fluctuations in density. However, no clear shocklets are observed. Vorticity, see fig. 3.17, shows a large number of small scale structures that are clustered in regions of higher density gradients. Contrasting this to the simulation at $M_t = 0.9$ a number of differences are noteworthy. The

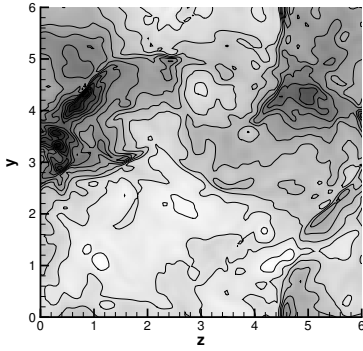


Figure 3.16.: Density contours for forced isotropic turbulence at $M_t = 0.45$ and $Re_\lambda = 90$. Plot taken from Brouwer et al. [12].

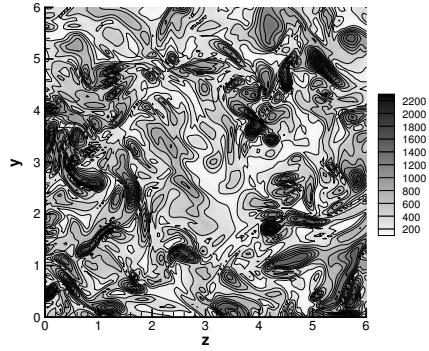


Figure 3.17.: Vorticity contours for forced isotropic turbulence at $M_t = 0.45$ and $Re_\lambda = 90$. Plot taken from Brouwer et al. [12].

density fluctuations in figure 3.18 are much larger than previously observed. In addition multiple regions of very large gradients, shocks, are visible. The vorticity, figure 3.19, is dominated by large scale structures whose shape adhere to the density gradient. The size of the structures is due to the lower Reynolds number of $Re_\lambda = 30$ of this simulation.

Within this section, an algorithm for the generation of forced compressible isotropic turbulence has been introduced that keeps initial mass, momentum and energy within the flow field constant. This algorithm has been used to compute multiple simulation of compressible isotropic turbulence in a statistically steady state with varying Mach- and Reynolds numbers. The statistics and visualization of the computations agree very well with those reported in the literature, e.g. Wang et al. in [121]. All in all, the results of forced compressible isotropic turbulence have been successful in showing the robustness of the skew-symmetric discretization in the presence of shocks and high Mach numbers.

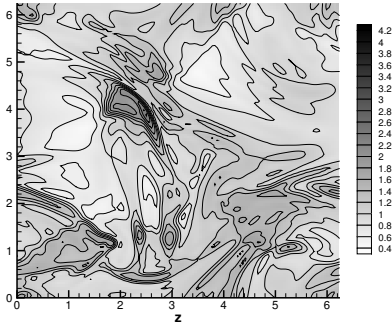


Figure 3.18.: Density contours for forced isotropic turbulence at $M_t = 0.9$ and $Re_\lambda = 30$. Plot taken from Brouwer et al. [12]

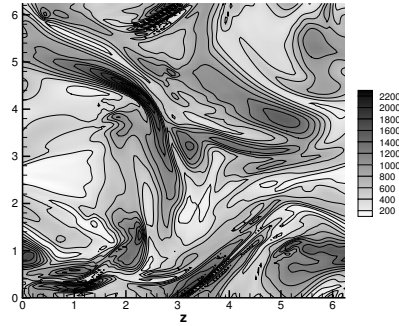


Figure 3.19.: Vorticity contours for forced isotropic turbulence at $M_t = 0.9$ and $Re_\lambda = 30$. Plot taken from Brouwer et al. [12]

3.4. Turbulent Boundary-Layer Flow

The accurate simulation of turbulent boundary-layers is central for the study of shock-wave/boundary-layer interactions. The turbulent flow field of the boundary-layer interacts with the shock-foot. Therefore no physically accurate simulation of the SBLI phenomenon is possible without accurate representation of the boundary-layer. This chapter is split into two parts. In the first, methods for the generation of turbulent inflow conditions are discussed, both in general in their application for boundary-layer flows and in particular for SBLI simulations. The second part describes the simulation of a turbulent boundary-layer with Reynolds number $Re_{\delta_{99}} \approx 5000$ which is used to validate the skew-symmetric finite-difference code for boundary-layer flows.

3.4.1. Turbulent Inlet Conditions

In its essence, a flat plate boundary-layer is a very simple flow configuration. The difficulty for the simulation of turbulent boundary-layers lies in the generation of turbulent inflow conditions. In principal, a laminar boundary-layer with a sufficiently high Reynolds number will transition to turbulent flow,

however the computational domain necessary to capture the natural transition of the flow is too large. Therefore artificial methods to generate turbulent inlet conditions have to be employed. Great care has to be taken to make sure that these artificial techniques do not introduce unphysical frequencies or correlations into the flow. The most simple method of introducing turbulence into the flow is the introduction of random perturbations in the flow field. However, as shown e.g. by [45], this method is not very effective and can even lead to relaminarization of the flow.

Recycling/Rescaling The basic idea of the recycling/rescaling technique is very simple and intuitive. At a wall-normal plane downstream of the inlet, called recycling station, turbulent fluctuations are recorded, rescaled according to self similarity laws of the boundary-layer and superimposed on a turbulent mean profile at the inlet. This idea was first introduced by Lund et al., [55], for incompressible boundary-layers and later adapted to the compressible case for example by Stolz & Adams, [108], and Xu & Martin, [127]. As the extension of the method to the compressible case poses the additional difficulty of finding scaling laws for the thermodynamic variables, many, slightly different, approaches exist. An overview of these methods is given in Sagaut et al, [90]. The approach presented here follows Pirozzoli & Bernadini, [76], and Stolz & Adams, [108]. According to Sagaut, the mean profile at the inflow is kept constant and only the fluctuations of velocity and density are rescaled. This approach avoids the so-called *numerical drift* phenomenon, where e.g. the boundary-layer thickness at the inlet is reduced over time. Pressure fluctuations are not recycled because the ratio $\frac{p'}{\bar{p}}$ is assumed to be negligible. Therefore the flow at the inlet is specified as:

$$\rho(0, y, z, t) = \bar{\rho}(y) + \rho'(0, y, z, t), \quad (3.4)$$

$$u(0, y, z, t) = \bar{u}(y) + u'(0, y, z, t), \quad (3.5)$$

$$v(0, y, z, t) = \bar{v}(y) + v'(0, y, z, t), \quad (3.6)$$

$$w(0, y, z, t) = 0 + w'(0, y, z, t), \quad (3.7)$$

$$p(0, y, z, t) = \bar{p}. \quad (3.8)$$

The mean velocity inlet profile can be specified using a semianalytical expression or taken from another simulation. The density profile is approximated using the Crocco-Busemann relation. To obtain the turbulent fluctuations the boundary-layer is decomposed into an inner and an outer layer which scale in viscous units, $y^+ = y/\delta_v$, and outer units, $\eta = y/\delta_{99}$, respectively.

Stolz & Adams stipulate the scaling for the velocity fluctuations to be

$$\frac{u'_i}{u_\tau} = G_{1,u}(y^+), \quad \frac{u'_i}{u_\tau} = G_{2,u}(\eta), \quad (3.9)$$

where G is a function independent of x . This can be manipulated to yield

$$u'_i(0, y^+) = \gamma u'_i(x_{rec}, y^+) \quad (3.10)$$

for the inner layer and

$$u'_i(0, \eta) = \gamma u'_i(x_{rec}, \eta) \quad (3.11)$$

for the outer layer. The rescaling parameter is the ratio of the friction velocities, $\gamma = \frac{(u_\tau)_{inn}}{(u_\tau)_{rec}}$. The application of the inner/outer layer decomposition to the density is not strictly justified and different scaling laws can be derived as described in references [90] and [108]. However, different authors have reported little influence of the exact scaling used on the results of the method. In particular, the transition length, until a *true* turbulent state is achieved, is not affected. Stolz & Adams propose a scaling of the density fluctuations with the freestream density ρ_∞ :

$$\frac{\rho'}{\rho_\infty} = G_{1,\rho}(y^+), \quad \frac{\rho'}{\rho_\infty} = G_{2,\rho}(\eta). \quad (3.12)$$

This leads to the simple form

$$\rho'(0, y^+) = \rho'(x_{rec}, y^+), \quad \rho'(0, \eta) = \rho'(x_{rec}, \eta), \quad (3.13)$$

for the density fluctuations at the inlet. In general the fluctuations of a quantity φ are assumed to be the weighted sum of the inner and outer layer fluctuations

$$\varphi'(y) = (1 - W(\eta)) \varphi'_{inn}(y^+) + W(\eta) \varphi'_{out}(\eta). \quad (3.14)$$

The weight function W is chosen according to Lund, [55], and Pirozzoli, [76], as

$$W(\eta) = \frac{1}{2} \left(1 + \frac{\tanh \left[\frac{a(\eta-b)}{(1-2b)\eta+b} \right]}{\tanh(a)} \right), \quad (3.15)$$

with $a = 4$ and $b = 0.2$. In addition, the fluctuations are shifted by half a spanwise period to avoid artificial correlation of the turbulent signal. In summary the fluctuations added to the mean inflow profile are:

$$(u'_i)^{inn}(0, y^+, z, t) = \gamma u'(x_{rec}, y^+, z + Lz/2, t), \quad (3.16)$$

$$(u'_i)^{out}(0, \eta, z, t) = \gamma u'(x_{rec}, \eta, z + Lz/2, t), \quad (3.17)$$

$$(\rho')^{inn}(0, y^+, z, t) = \rho(x_{rec}, y^+, z + Lz/2, t), \quad (3.18)$$

$$(\rho')^{out}(0, \eta, z, t) = \rho(x_{rec}, \eta, z + Lz/2, t). \quad (3.19)$$

Pirozzoli et al. use a modified version of the recycling parameter that is weighted with the density at the wall, $\gamma = \frac{(u_\tau \sqrt{\rho_w})_{in}}{(u_\tau \sqrt{\rho_w})_{rec}}$. This can be seen as the compressible modification of the incompressible scaling law derived by Lund for the velocities. See also Schroeder et al., [101], for a similar motivation of the rescaling parameter. To achieve transition to a fully turbulent state faster, the flow is generally initialized with added synthetic perturbations that mimic inner and outer layer streaks as introduced by Sandham et al., see [93].

The Digital Filter Approach The recycling/rescaling approach, while easy to use and implement in most situations, is not without downsides. The feedback loop between the recycling station and the inlet will inevitably introduce artificial low-frequencies and correlations into the computational domain. This is not a significant problem when the distance between inlet and recycling station is very long or in cases where the focus is not on low-frequency behavior. In cases where it is, like shock-wave/boundary-layer interaction, it is hard to justify the use of recycling/rescaling. The artificial tone imprinted on the system by the generation of inflow data might effect the overall behavior of the low-frequency oscillations. In such cases, a different way to generate inflow data has to be used. Methods that generate turbulent data without using intrinsic data from the current flow field are often called *synthetic turbulence* methods. One way is to introduce artificial, analytically determined, perturbations that mimic real turbulence into the flow, see e.g. [75, 93]. Another way, pioneered by Klein, Sadiki and Janicka, is the *digital filter* approach, see [45]. The idea of this technique is to construct a turbulent field with prescribed lengthscales by applying a specifically constructed filter to a set of random variables. It follows a short description of the filter construction and the actual implementation of the technique in the simulation. The approach presented here is based on modifications and simplifications by Toubert and Sandham as well as Xie and Castro on the

Procedure 3.2: Generation of Turbulent Inflow Data via the Digital Filter Approach

1. Generate 3 sets of normally distributed random numbers with zero mean, r^i , $i = u, v, w$.
2. Apply the filter $\nu^i = F_N^i(r^i)$.
3. Correlate the current filtered field with the previous one to enforce the streamwise lengthscale:

$$\phi^i = \nu_{old}^i \exp\left(-\frac{\pi\Delta t}{2\tau}\right) + \nu^i \sqrt{1 - \exp\left(-\frac{\pi\Delta t}{\tau}\right)}. \quad (3.20)$$

The langrangian timescale τ is derived from the integral lengthscale via $\tau = I_x/U$, where U is the local mean velocity.

4. Enforce single-point correlations at the inflow by setting:

$$S = \begin{pmatrix} \sqrt{R_{11}} & 0 & 0 \\ R_{21}/\sqrt{R_{11}} & \sqrt{R_{22} - (R_{21}/\sqrt{R_{11}})^2} & 0 \\ 0 & 0 & \sqrt{R_{33}} \end{pmatrix}. \quad (3.21)$$

5. Set the inflow plane as:

$$\begin{pmatrix} u(0, y, z, t) \\ v(0, y, z, t) \\ w(0, y, z, t) \end{pmatrix} = \begin{pmatrix} U(0, y, z) \\ V(0, y, z) \\ W(0, y, z) \end{pmatrix} + S \begin{pmatrix} \phi^u(y, z, t) \\ \phi^v(y, z, t) \\ \phi^w(y, z, t) \end{pmatrix}. \quad (3.22)$$

original algorithm by Klein et al., found in [115,126]. First a filter, F_N , is constructed that imbues a random vector with zero mean, r_k , with a given integral length scale $I_x = \Delta xn$. The filter

$$F_N(r_k) = \sum_{j=-N}^N b_j r_{k+j} \quad (3.23)$$

is then constructed in a way that its application to r_k yields a field with two-point correlation

$$R(x_k + x) = \exp\left(-\frac{\pi x}{2I_x}\right), \quad (3.24)$$

and integral lengthscale I_x . According to Touber and Sandham, the filter coefficients b_k are given as:

$$b_k = \tilde{b}_k \left(\sum_{j=1}^s \tilde{b}_j^2 \right)^{-1/2}, \quad \tilde{b}_k = e^{-\frac{\pi k}{n}}. \quad (3.25)$$

The procedure above, given in one dimension, can be extended to two dimension with $b_{ij} = b_i \cdot b_j$. The filter needs to be constructed once with given spanwise and wall-normal lengthscales I_y and I_z . The streamwise lengthscale I_x will be enforced in the temporal domain. In addition, the desired Reynolds-stress tensor R_{ij} as well as a mean inflow profile U have to be specified. The full procedure to generate turbulent inflow data is given in 3.2.

Comparisons of the skin-friction and the velocity statistics presented in [115] find that the digital filter approach produces transitional regions of the order of $10\delta_{99}$ before a mean turbulent state is achieved. Touber and Sandham find the method to be very robust to the choice of prescribed lengthscales and filtering coefficients. As long as the lengthscales imposed on the flow are larger than the physical ones, the flow transitions to its natural state very quickly. When the imposed lengthscales are too small, the filter procedure is essentially equivalent to adding white noise to the inflow which can lead to relaminarization of the flow. The method of digital filtering allows the explicit prescription of the lengthscales introduced through the inflow conditions. Therefore it is a good choice for the simulation of transonic shock-wave/boundary-layer interaction since it ensures no low-frequency oscillations are introduced artificially.

3.4.2. A Turbulent Boundary-Layer at $Re_\delta \approx 4736$

A transonic turbulent boundary-layer at Mach number $Ma = 0.8$ is simulated using the conservative skew-symmetric finite-difference approach developed within this thesis. In order to validate the methods, most parameters have been chosen in accordance with a simulation presented by Pirozzoli and Bernardini, case TBL 1 from [74]. The major difference being the chosen

$Re_{\delta_{in}}$	N_x	N_y	N_z	Δx^+	Δy^+	Δy_e^+	Δz^+	Tu_∞/δ_{in}
4736	1920	192	204	~ 7	~ 0.8	~ 6	~ 7	581.7
Re_τ		Re_θ		H		$C_f(\cdot 10^3)$		
203 – 501		471 – 1812		1.916 – 1.696		3.41 – 4.633		

Table 3.2.: Details on the parameters of the turbulent boundary-layer simulation. Δy_e^+ refers to the grid spacing in wall units at the edge of the boundary-layer. T is the timespan during which statistics have been collected. $Re_\tau = \rho_w u_\tau \delta / \mu_w$, $Re_\theta = \rho_0 u_0 \theta / \mu_0$

Mach number. Since the aim of this work is the simulation of transonic SBLI which takes place at freestream Mach numbers in the range 0.7 – 0.85, Pirozzoli’s Mach number has been reduced to fit into that regime.

Computational Setup The conservative, skew-symmetric formulation of the Navier-Stokes equations is discretized using 6th order central differences with the SBP property, see chapter 2.4. Time integration is handled using a standard 4-stage Runge-Kutta scheme during the initial transition period. After a statistically steady regime has been reached, as measured by the temporal evolution of the shape parameter H , which is the ratio of displacement and momentum thickness of the boundary-layer, time integration switches to the conservative 4th order Gauss-collocation method.

The dimension of the computational domain is $[L_x \times L_y \times L_z] = [106\delta_{in} \times 8.3\delta_{in} \times 9.3\delta_{in}]$, where δ_{in} is the 99% boundary-layer thickness at the inlet. This domain is discretized using $[1920 \times 192 \times 204]$ gridpoints. The grid is equidistant in streamwise and spanwise direction, while a hyperbolic tangent function is used to cluster the points near the wall boundary. The grid spacing

$Re_{\delta_{in}}$	N_x	N_y	N_z	Δx^+	Δy^+	Δy_e^+	Δz^+	Tu_∞/δ_{in}
3000	384	192	144	~ 17	~ 0.8	~ 7	~ 15	152
Re_τ		Re_θ		H		$C_f(\cdot 10^3)$		
163 – 266		350 – 730		1.95 – 1.85		3.83 – 5.752		

Table 3.3.: Details on the parameters of the precursor simulation. Δy_e^+ refers to the grid spacing in wall units at the edge of the boundary-layer. T is the timespan during which statistics have been collected. $Re_\tau = \rho_w u_\tau \delta / \mu_w$, $Re_\theta = \rho_0 u_0 \theta / \mu_0$

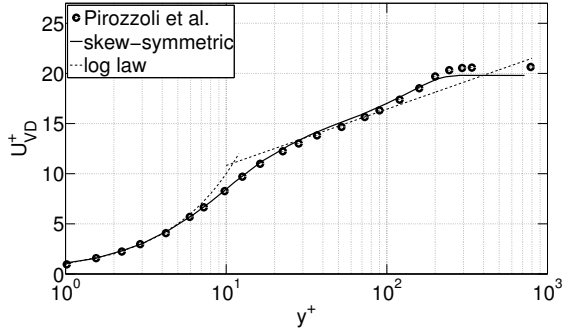


Figure 3.20.: Mean VanDriest velocity profile of the precursor simulation taken at $Re_\delta = 4736$; triangles: Pirozzoli et al. [74]; solid line: log-law ($5.2 + 1/0.41 \log(y^+)$)

in wall units can be seen in table 3.2. The domain is periodic in spanwise direction, while non-reflecting boundary conditions, as described in section 2.4, are applied at the top and downstream boundaries. The flat plate is modeled by an adiabatic no-slip condition.

Inflow Conditions As previously described, the choice of the turbulent inflow conditions is crucial for the simulation of the boundary-layer. Since this simulation deals with an unperturbed TBL, the recycling/rescaling method can be used in its form described previously. The recycling station is placed in the middle of the domain at $x_{rec} = 53\delta_{in}$. Special care is taken in the choice of the prescribed mean turbulent inflow profile. To obtain a suitable inlet profile, a separate precursor simulation, with lower resolution and inlet Reynolds number, has been run on a $[50\delta_{in} \times 6\delta_{in} \times 6\delta_{in}]$ domain. Once the precursor simulation reached a steady state, the mean velocity profile at $Re_\delta = 4736$ was extracted. Details of the precursor simulation are displayed in table 3.3. The inlet profile in the precursor simulation was taken from the semi-analytical expression for the mean VanDriest transformed velocity

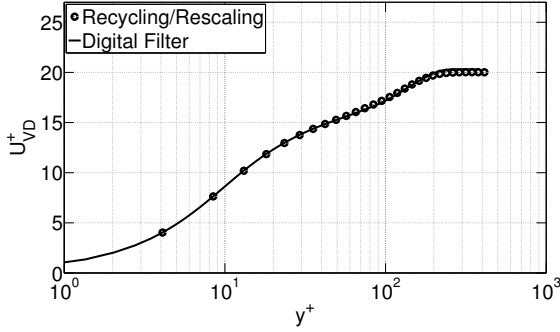


Figure 3.21.: Comparison of mean VanDriest velocity profiles of at $Re_\tau = 207$ in the precursor simulation using the recycling/rescaling and digital filter techniques for the generation of inflow data.

stated by Guarini et al., [32]:

$$\bar{u}_{vd}^+ = \begin{cases} \frac{1}{k} \log(1 + ky^+) + C_1 \left(1 - e^{-y^+/\eta_1} - \frac{y^+}{\eta_1} e^{-by^+} \right) & y < \delta, \\ \bar{u}_{vd\infty}^+ + \frac{1}{k} \left[\left(\frac{y}{\delta} \right)^2 - \left(\frac{y}{\delta} \right)^3 + 6\Pi \left(\frac{y}{\delta} \right)^2 - 4\Pi \left(\frac{y}{\delta} \right)^3 \right] & y > \delta, \end{cases}$$

where $k = 0.41$, $C = 5.1$, $\Pi = 0.2$, $C_1 = C - \log(k)/k$, $\eta_1 = 11$ and $b = 0.33$. Figure 3.20 depicts the mean velocity profile extracted from the precursor simulation. In this, and the following figures, the reference solution is depicted as a series of dots for better visualization. The full profile can be found [74]. This intermediate step was done for two reasons. First, as an additional validation step for the code. Seeing that the code predicts the correct mean flow statistics at lower resolutions validates the basic functionality of the skew-symmetric approach to turbulent flows. In addition, the extraction of the mean profile prevents errors or inconsistencies between the prescribed semianalytical inlet profile and the flow within the domain to effect the highly resolved simulation. The grid used for both the full and precursor simulations is adequate as can be seen from the resolution in wall units given in tables 3.2 and 3.3. While the span- and streamwise resolution of the precursor simulation do not match the usual requirements for rigorous DNS studies of turbulent wall-bounded flows, this fault is rectified in the full simulation.

A note on the digital filter approach for the generation of inflow data: As

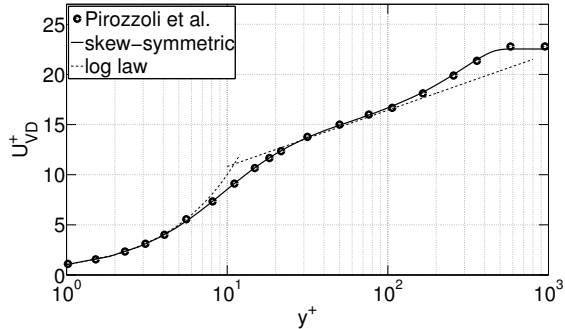


Figure 3.22.: Mean VanDriest velocity profile of the direct numerical simulation taken at $Re_\tau = 482.3$; solid line: log-law ($5.2 + 1/0.41 \log(y^+)$)

mentioned previously, in the simulation of transonic SBFI the recycling/rescaling technique will not be employed due to its ability to introduce artificial frequencies into the simulation. Therefore both the precursor and high-resolution simulation were also computed with the digital filter inlet conditions. In the following, only results of the recycling/rescaling approach are shown. It was found that the digital filter approach produces a transitional region of length $\sim 10\delta_{in}$. For all statistical quantities ϕ of both simulations, the relation $\phi_{DF}(x) \approx \phi_{RR}(x - 10\delta_{in})$ holds. When considering streamwise locations with the same Re_τ , both variants collapse onto each other as evidenced in figure 3.21.

Both the precursor and actual simulations were run on the Hannover complex of the North German Supercomputing Alliance.

Mean Velocity Statistics All flow statistics were collected over 581.7 dimensionless time units corresponding to just under 6 flow through times of the whole computational domain. To lessen the burden on the postprocessing,

x_0/δ_{in}	δ/δ_{in}	Re_τ	Re_θ	H	$C_f(\cdot 10^3)$
83.2	2.51	482.3	1403.4	1.746	3.5

Table 3.4.: Information on the flow features and scaling parameters of the reference station x_0 chosen for the validation of the turbulent boundary-layer simulation.

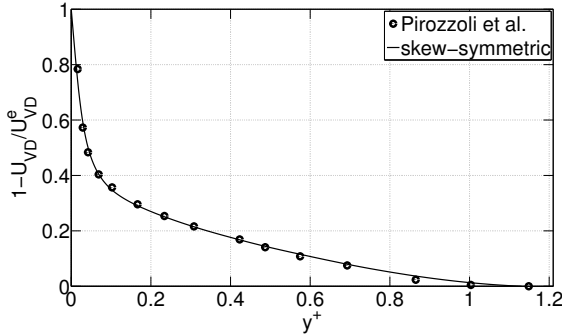


Figure 3.23.: Comparison of mean VanDriest transformed velocity defect for the TBL simulation at reference station x_0

statistics and averages are computed on the fly using a sliding average technique. Before the statistical sampling was started, data from $Tu_\infty/\delta_{in} = 150$ time units was discarded to eliminate any contamination of the results by initial transients. The velocity statistics are displayed for a reference station at $x_0/\delta_{in} = 83.2$, see table 3.4 for details. This specific station was chosen to match the friction Reynolds number $Re_\tau = \rho_w u_\tau \delta / \mu_w$ with data taken from Pirozzoli and Bernadini in [74]. Figure 3.22 compares the mean VanDriest transformed velocity profile at the reference station with the log-law and Pirozzoli's data. The VanDriest transform of the velocity

$$U_{VD} = \int_0^{U_\infty} \left(\frac{\rho}{\rho_w} \right) dU \quad (3.26)$$

can be seen as a density correction of the profile and collapses data at different Mach numbers very well, see [118] and [74, 95, 96]. Assuming a layer of constant stresses and using the assumption that the size of eddies in the overlap layer, $y^+ = x - y$, is proportional to y , the logarithmic law for the effective VanDriest velocity can be constructed:

$$U_{VD}^+ = \frac{1}{k} \log(y^+) + C. \quad (3.27)$$

Typical parameters for turbulent boundary-layers set $k = 0.41$ and $C = 5.2$, see e.g. [80, 119]. As found in [74], the friction Reynolds number, Re_τ , can

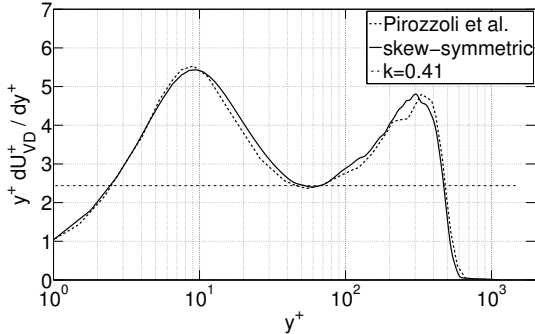


Figure 3.24.: Comparison of the diagnostic function $y^+ dU_{VD}^+ / dy^+$ for the TBL simulation at reference station x_0 . The dotted line denotes the log law with $k = 0.41$.

be used to match data at different Mach numbers surprisingly well. The surprise coming from the fact that simulations with different Mach number but same Re_τ yield different strengths of the wake, see e.g. [48]. The same behavior can be observed in the mean VanDriest velocity defect, see 3.23. In the inner layer, both profiles agree perfectly while only small difference that can be observed past $y\delta = 0.4$. Further inspection of the velocity profile via the so-called diagnostic function

$$y^+ \frac{dU_{VD}^+}{dy^+} \quad (3.28)$$

in figure 3.24 reveals that the Reynolds number of the present simulation is too low to exhibit a significant logarithmic layer at $y^+ = 50 - 200$. However, the profile exhibits its local minimum at the correct value of the matching log-law with $k = 0.41$. All in all it can be concluded that the mean velocity profile of the subsonic turbulent boundary-layer is accurately computed.

To compare the turbulence intensities of the present simulation with those of Pirozzoli and Bernadini, the usual entries of the Reynolds stress tensor have to be density-corrected with a procedure similar to that of the VanDriest transform of the velocity. Following Morkovin's hypothesis, [67], one can arrive at:

$$\widetilde{u''v''} \sim \frac{\bar{\rho}_w}{\bar{\rho}} u_\tau^2, \quad (3.29)$$

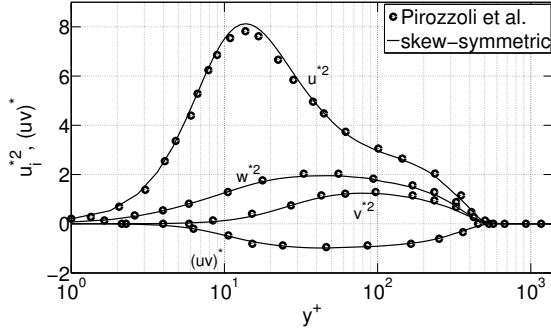


Figure 3.25.: Comparison of inner- and density scaled turbulence intensities for the TBL simulation at reference station x_0 .

where $\tilde{\varphi}$ and φ'' stem from the mass-weighted Favre decomposition: $\varphi = \tilde{\varphi} + \varphi''$, $\tilde{\varphi} = \overline{\rho\varphi}/\bar{\rho}$. Equation (3.29) implies

$$\left(\widetilde{u''^2_i}\right)^{1/2} \sim (\bar{\rho}_w/\bar{\rho})^{1/2} u_\tau \quad (3.30)$$

which is used to define the density-scaled, inner-scaled velocity statistics:

$$(uw)^* = \frac{\widetilde{u''v''}}{u_\tau^2} \left(\frac{\rho}{\rho_w}\right), \quad (u_i)^* = \frac{\left(\widetilde{u''^2_i}\right)^{1/2}}{u_\tau} \left(\frac{\rho}{\rho_w}\right). \quad (3.31)$$

The validity of this scaling can be observed in figure 3.25, where the stresses of the present $Ma = 0.8$ computation are compared with the $Ma = 2$ computation of the reference simulation. The small differences in $(u^*)^2$ in the region $y^+ \approx 10 - 30$ are in line with those observed between Pirozzolis data and incompressible results of Schlatter et al. in [94]. Apart from this discrepancy, all stress profiles match very well.

Lastly, the evolution of skin friction is reported. To compare the data with the incompressible law, see Smits et al. [106]

$$C_f = 0.0024Re_\theta^{-1/4} \quad (3.32)$$

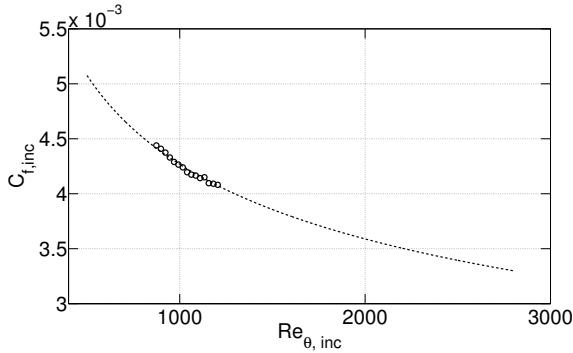


Figure 3.26.: Incompressible scaling of skin friction C_f versus Reynolds number; dotted line: empirical relation (3.32)

the VanDriest II transform of skin friction and Reynolds number,

$$C_{f_{inc}} = F_c C_f, \quad Re_{\theta_{inc}} = F_\theta Re_\theta, \quad (3.33)$$

$$F_c = \frac{\bar{T}_w/T_\infty - 1}{\arcsin^2 \alpha}, \quad F_\theta = \frac{\mu_\infty}{\mu_w}, \quad (3.34)$$

$$\alpha = \frac{\bar{T}_w/T_\infty - 1}{\bar{T}_w/T_\infty (\bar{T}_w/T_\infty - 1)}, \quad (3.35)$$

is applied, see [118]. This way, data taken at different Mach numbers can be accurately compared. Figure 3.26 compares the reference law (3.32) with data taken from the present simulation and finds good agreement.

Flow Visualization and Structure In this section a variety of flow visualizations is shown that serve to illustrate the organization of the wall-bounded turbulent flow. In general, two-dimensional slices of the domain are adequate instruments to understand the flow structure. With this aim in mind, three wall-parallel planes are extracted from the flow at $y^+ = 15$, $y/\delta = 0.3$ and $y/\delta = 0.9$. Since the boundary-layer thickness δ increases throughout the domain, these planes are obtained by interpolation of the original flow field and cannot be extracted explicitly. The plane at $y^+ = 15$ is the region where the streamwise turbulence intensities reach their maximum, see figure 3.25, the second plane represents the outer part of the boundary-layer while the most distant slice at $y/\delta = 0.9$ displays the edge of the boundary-layer itself.

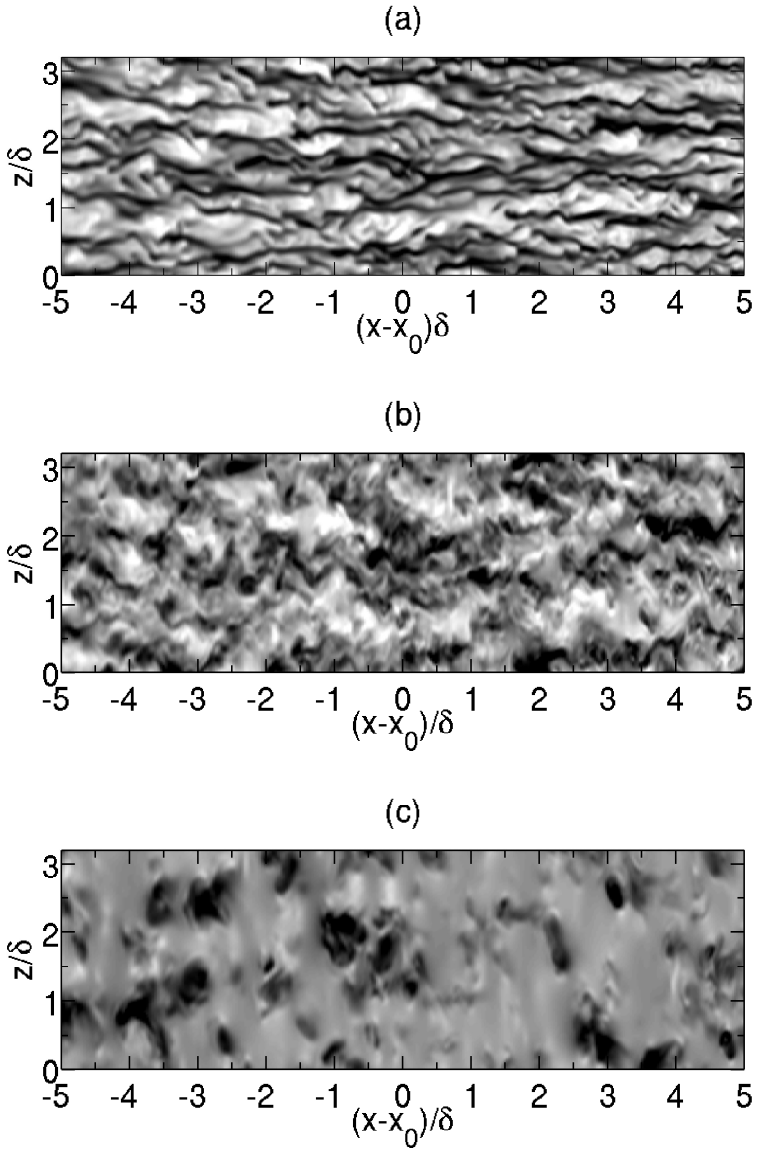


Figure 3.27.: Instantaneous streamwise velocity in a wall normal plane at: (a): $y^+ = 15$, (b): $y/\delta = 0.3$ and (b): $y/\delta = 0.9$. Contours range from $-c \leq u/u_0 \leq c$ with $c = 0.25, 0.15, 0.12$ for the three panels respectively.

Similar visualizations of the boundary-layer are shown in [61, 74]. Figure 3.27 shows the instantaneous velocity field in the wall-normal planes. Figure (a), taken at $y^+ = 15$, shows the typical streak-like structures of spanwise alternating regions of high and low velocity. Going away from the wall to figure 3.27 (b), the streak structure is still visible, although the spanwise extent of the streaks has grown. At the edge of the boundary-layer, 3.27 (c), velocity is almost uniform except for remnants of burst and sweep events, which transport fluid to- and away from the wall. These events will be even more pronounced in the visualization of the temperature.

The temperature field is shown in figure 3.28. The first plane, (a), shows a similar streaklike organization as the velocity. Common to all three wall-normal slices is the negative correlation of temperature and velocity fluctuations. Low-velocity regions correspond to high temperature zones. This can be understood as follows. Ejection events transport low speed and high temperature fluid away from the wall. Panels (b) and (c) of figure 3.28 paint a clear picture of the structure of these ejection events. High temperature structures take on a mushroom like shape with fluid following in a hot wake. In contrast to the velocity structures, which were almost exclusively organized in streamwise direction, the mushroom like zones of hot fluid extent in the spanwise direction when moving away from the wall.

The occurrence of these events transporting fluid away from the wall is even more evident in visualizations of slices in the yz -plane. Figure 3.29 shows streamwise velocity and density fluctuations at $x/\delta_{in} = 65$. The organization of negative velocity and low density structures in mushroom shaped structures is obvious in this depiction. In addition, the spatial growth of these structures with their extent from the wall can be observed.

Lastly, representations of the flow in streamwise aligned, wall-normal slices are shown in figure 3.29. The velocity field shown in pane (a) of 3.29 show the very typical high intermittency in the outer part of the boundary-layer. In addition, deep *valleys* in the velocity structure are visible, where the freestream intrudes deep into the boundary-layer, reaching down into its inner layer. Looking at the density in panel (b), the differentiation between the turbulent, rotational flow within the boundary-layer and the irrotational fluid in the freestream is very distinct when compared to the smoother interfaces in the velocity. Visible in both quantities are distinct bulges of low velocity and density which reach into the outer layer of the flow. The inclination of the density bulges is roughly 45° , while the bulges in velocity have smaller inclination. Note the independent axes in the figure. These correspond to the typical angle of hairpin vortices found in boundary-layer flow.

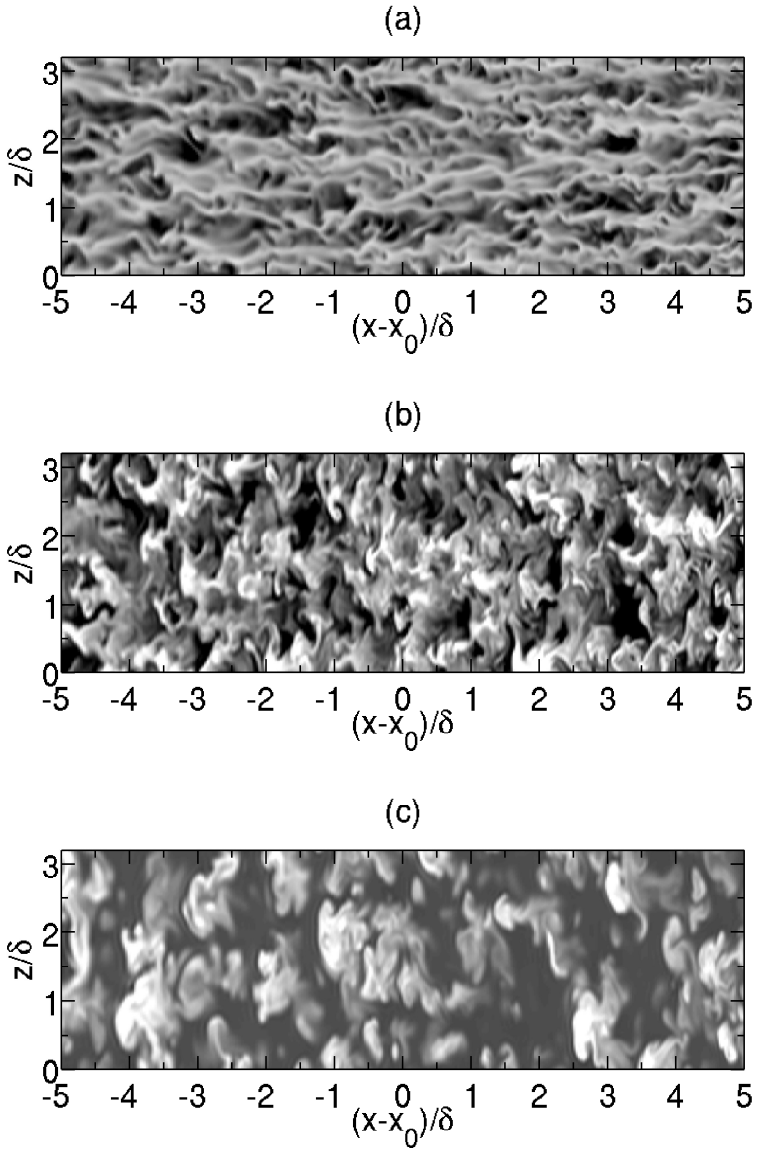


Figure 3.28.: Instantaneous temperature in a wall normal plane at: (a): $y^+ = 15$, (b): $y/\delta = 0.3$ and (c): $y/\delta = 0.9$. Contours range from $-c \leq T/T_0 \leq c$ with $c = 0.12, 0.07, 0.07$ for the three panels respectively.

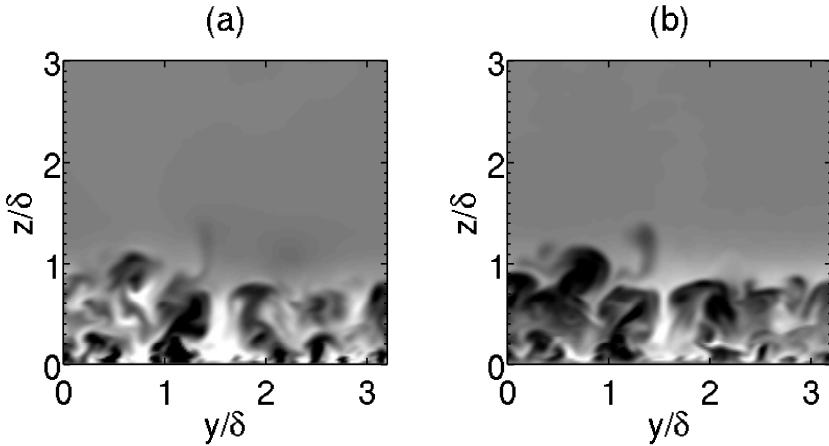


Figure 3.29.: Instantaneous velocity (left) and density (right) fluctuations in a spanwise plane located at $x/\delta_{in} = 65$. Contours range from $-c \leq \varphi/\varphi_0 \leq c$ with $c = 0.13, 0.03$ for the two panels respectively.

Conclusion A DNS simulation of a turbulent boundary-layer with a inlet Reynolds number of $Re_{\delta_{99}} = 4736$ has been performed using the fully conservative, skew-symmetric finite-difference formulation. Velocity statistics and flow visualizations have been compared and validated with existing results of highly accurate direct numerical simulations by Pirozzoli and Bernadini, [74]. Although of a different Mach number, density-scaling of the velocity and stresses leads to a collapse of both simulations when a match of the friction Reynolds number, Re_{τ} , is enforced. All in all, the results of the turbulent boundary-layer simulation with the fully conservative, skew-symmetric finite-difference code compare very well with existing simulations and theoretical results. Therefore a sufficient trust and reliability of the newly developed scheme has been established to tackle the more complex transonic SBLI situation.

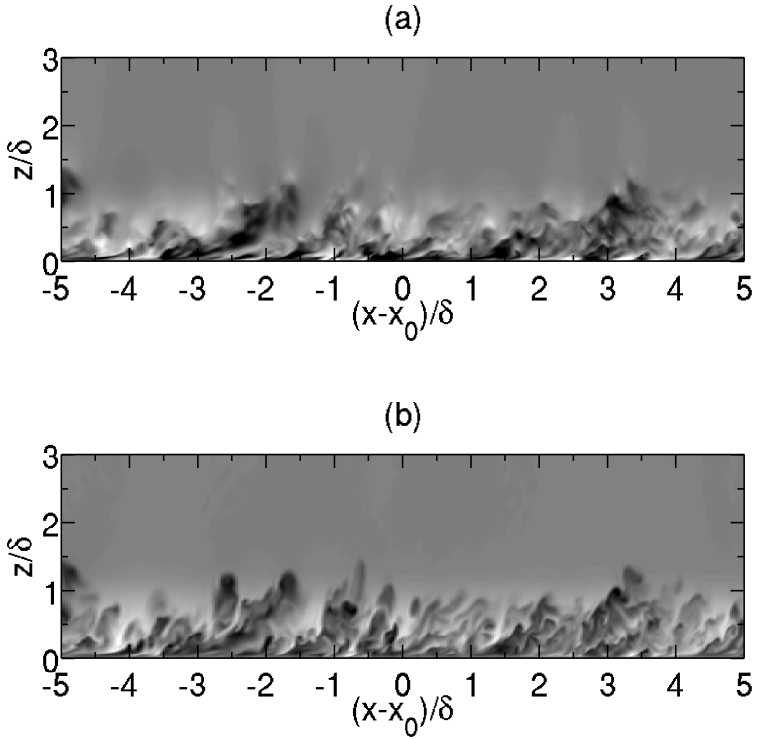


Figure 3.30.: Instantaneous velocity (left) and density (right) fluctuations in a streamwise plane. Contours range from $-c \leq \varphi/\varphi_0 \leq c$ with $c = 0.2, 0.04$ for the two panels respectively.

II

Transonic Shock-Wave/Boundary-Layer Interactions

Introduction to Shock-Wave/Boundary-Layer Interactions

The analysis of shock-wave/boundary-layer interactions is the main objective of this thesis. Therefore this chapter aims to give an introduction into the topic. An overview of the underlying physics will be given. Special effort is placed on low-frequency unsteadiness in SBLI and an overview of research and theories on the origin of this phenomenon is given.

4.1. Description of a Shock-Wave/Boundary-Layer Interaction

Research into the interaction of boundary-layers and shock-waves has been conducted for almost 70 years. In 1946, Liepmann et al, [54] published experiments in which they studied the interaction of transonic boundary-layers with shocks. Since then numerous studies have been conducted into the nature of SBLI in many different situations and circumstances. During this time, advances in technology and scientific insight have furthered the understanding of scientists and engineers into the phenomenon. A number of comprehensive reviews, such as Dolling and Lee, [20,50], at the beginning of the new century, or the more recent work of Clemens and Narazanaswamy, [15], and Babinsky et al, [4], recapitulate the knowledge gained since the mid 40s.

Shock-wave/boundary-layer interactions occur in many engineering applications. Prime examples are airfoils in transonic flight or high speed intakes of turbomachinery. Due to these different circumstances, different variants of SBLI exist. In external aerodynamic flows the baseflow is transonic. When the flow is accelerated over the airfoil a supersonic pocket forms that is terminated by a normal shock impinging on the airfoil surface. Depending on the angle of attack, the Mach and Reynolds number different SBLI situations may occur. Mundell and Mabey, [68], give an overview of the common SBLI setups. They characterize the flow over an airfoil by the occurrence and size of a recirculation bubble downstream of the shock and identify three regimes of transonic SBLI on an airfoil. The first one being a weak shock that does not induce the formation of recirculation bubble. The second one, where the adverse pressure gradient is large enough to separate the boundary-layer, sports a recirculation bubble with a finite extent. The last case is characterized by a separated boundary-layer that does not reattach on the airfoil. All these kind of flows may contain large scale shock movements. These movements, called shock buffeting, impose unwanted and harmful loads on the airfoil and should be avoided at all costs.

In high-speed flows, common for internal aerodynamic applications, the baseflow is already supersonic. Shock-waves, typically generated by changes in the geometry away from the current boundary, impinge on the supersonic flow. The incoming waves may be normal or oblique and the specific nature of the interaction varies accordingly. A similar interaction happens when a supersonic flow impinges on a compression ramp and an oblique shock-wave forms.

Earlier work on shock-wave/boundary-layer interaction often studied the whole complex situation phenomenologically. A good example being Finke's work extensive experimental work on the buffeting behavior of differently shaped airfoils and cylinders in [25]. With the advent of numerical investigations the same trend could be observed there, see e.g. [18,53]. However, in the last few decades the focus of research has shifted. Instead of looking at the complete flow field around an airfoil for example, the focus has been shifted to the fundamentals of the shock-wave/boundary-layer interaction. Even when most of the complexity of real physical flows, like curved geometries and the interaction of sub- and supersonic regions, has been filtered out, the pure interaction of a shock and wall-bounded flow is not fully understood. Since the turn of the century the increasing of computational resources has given rise to highly accurate DNS and LES simulations, probably starting with the DNS of a compression ramp by Adams et al, [1]. These studies, as conducted

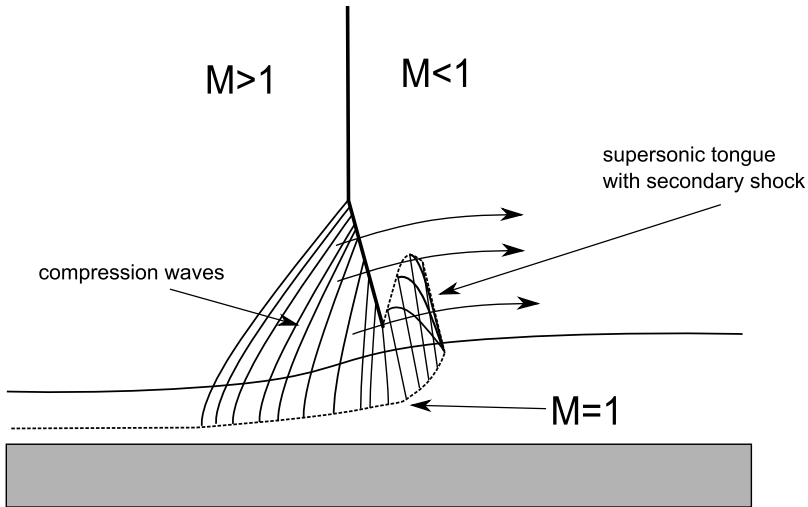


Figure 4.1.: Schematic view of a normal shock impinging on a flat wall without separation.

e.g. by Sandham et al. or Pirozzoli et al., [77, 115], typically do away with the subsonic flow region and investigate a flat plate turbulent boundary-layer with an impinging shock. This way, the SBLI can be investigated without large scale upstream influence.

In the following, the basic organization of a shock-wave/boundary-layer interaction is presented using the example of an impinging normal shock. As introduced by Delery and Marvin in 1986, [19], any SBLI can be characterized as either weak or strong. A weak interaction being an interaction where the adverse pressure gradient imposed by the shock is not large enough to separate the boundary-layer and strong interactions, where significant separation is present. Weak and strong interactions have vastly different flow features, therefore both types will be presented in the following.

Normal Shock Impingement By its nature, a normal shock impinging on a turbulent boundary necessitates supersonic flow upstream of the shock and subsonic flow downstream of it. Away from the wall, the flow is basically inviscid and the shock is described by the Euler-equations. Near the boundary, where viscous effects dominate, an interaction zone develops whose behavior

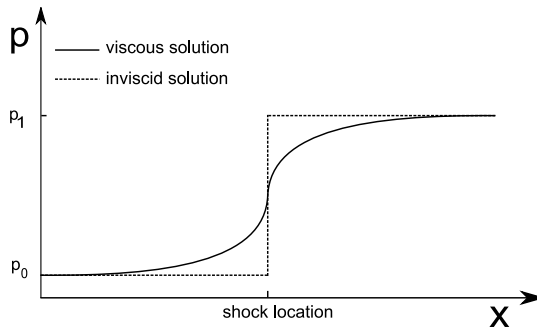


Figure 4.2.: Wall pressure in a weak SBLI without separation

will be detailed in this section. The adverse pressure gradient implied by the shock in the inviscid region is infinite. Would this remain the case down to the wall any boundary-layer would separate. Therefore the interaction of shock and boundary-layer must diffuse the pressure jump near the wall. As seen in figure 4.1, there is a sonic line in the incoming boundary-layer. Below this line the flow is subsonic and pressure information can travel upstream below the shock. This mechanism smears out the pressure change through the shock and lessens the pressure gradient imposed from the freestream region, see fig. 4.2. Due to the adverse pressure influence the upstream boundary-layer thickens as the shape factor and displacement thickness increase. The thicker boundary-layer profile diverts the supersonic flow in the freestream away from the wall. This leads to the formation of compression waves which increase the local pressure at the boundary-layer edge and reduce the local Mach number. This process weakens the shock strength of the normal shock. In this way, an equilibrium position is reached. The fact that the upstream streamlines are tilted away from the wall has the consequence that the foot of the normal shock is curved backwards as to remain normal to the deflected flow. In fact, the thickening of the boundary-layer can be interpreted like a curved surface for the de-facto inviscid outer flow. Behind the shock, the continuous diffusion of the pressure gradient towards the wall imposes a vertical pressure gradient. Coupled with the near sonic velocities behind the shock this can lead to the formation of a so-called *supersonic tongue*. Here expansion waves are generated at the surface which reflect as compression waves from the sonic line. This trailing supersonic region is often terminated by weaker, secondary shocklets, see 4.1.

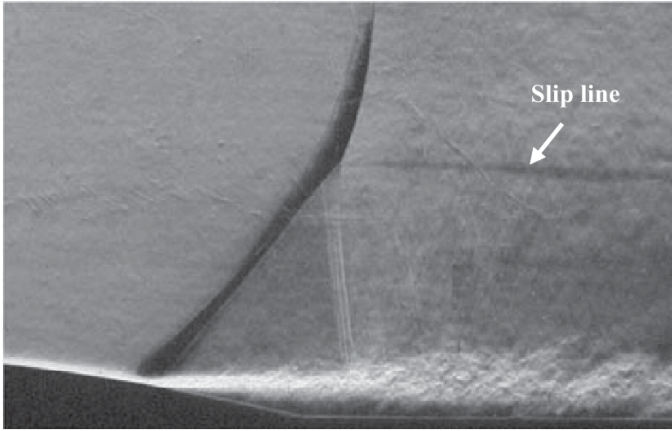


Figure 4.3.: Schlieren visualization of a λ -shock system on a curved surface, taken from [4]

Shock-Induced Separation The picture described above changes radically once the pressure gradient imposed by the shock, even in its diluted form at the wall, is strong enough to separate the boundary-layer. The specific point of boundary-layer separation is hard to pinpoint. Generally a Mach number of $Ma \approx 1.3$ will suffice for the flow to separate. However, this number is sensitive to geometry and other factors. Figure 4.3 depicts the resulting flow field characterized by an additional oblique separation shock and the large scale turbulent structures trailing from the separation. Due to its form, the normal shock system with induced boundary-layer separation is also called λ -shock system. Figure 4.4 shows a schematic sketch of the λ system. The formation of a separation bubble has two main effects on the flow. First, the lengthscale of the upstream influence increases since the recirculating flow in the separated region transmits information upstream in a far more effective manner. Second, the bubble acts like a viscous wedge for the incoming boundary-layer and generates an oblique shock at the separation point. The new shock formation can be explained this way. The onset of separation produces a sharp edge in the effective displacement surface for the incoming supersonic boundary-layer. This causes compression waves to form and coalesce into an oblique shock-wave. The pressure rise through this first compression is not enough to account for the full inviscid pressure jump forecasted by the Rankine-Hugoniot conditions and thus a second shock-leg

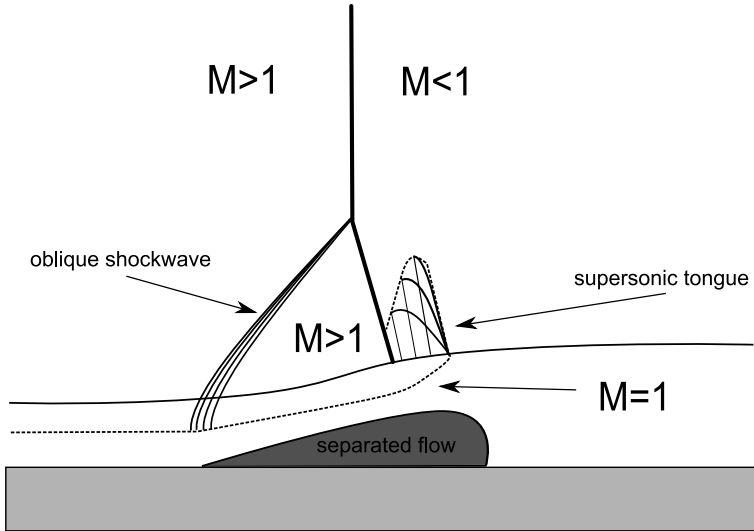


Figure 4.4.: Schematic view of a normal shock impinging on a flat wall with separation - forming a λ -shock system.

forms at the rear part of the structure. The second leg is again inclined as to remain normal to the displaced flow. Leading and terminating shock merge with the main normal shock in the so-called *triple point*. As the shear layer above the separated flow can not support large pressure gradients, the wall pressure displays a plateau beneath the bubble, see figure 4.5. As in the case without separation, the strong vertical pressure gradient coupled with the curved displaced surface leads to the formation of a supersonic tongue downstream of the rear leg.

4.2. Low-Frequency Unsteadiness in SBLI

The most studied topic concerning shock-wave/boundary-layer interactions is the occurrence of low-frequency oscillations within the interaction zone. Under certain conditions, depending on the angle of attack or variations in downstream pressure, this unsteadiness manifests as large scale down- and upstream movement of the shock, [50]. But even on simple flat plate geometries without significant up- or downstream influences the combined system

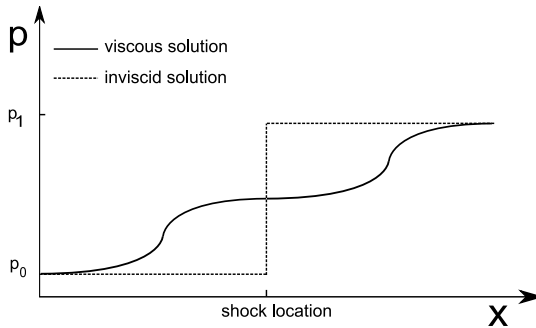


Figure 4.5.: Wall pressure in a strong SBLI with separation

of shock and recirculation bubble undergoes low-frequency oscillations. Even though SBLI appear in all kind of different specific situations the frequency of this unsteadiness is always two to three orders of magnitude below the typical frequency of pressure fluctuations within the incoming boundary-layer whose Strouhal number $St = f\delta/u_0$ is of order 1, where u_0 is the freestream velocity and δ the boundary-layer thickness. See table 4.1 for an overview over some of the available data. Even after extensive research the origin of this unsteadiness is still debated. For obvious reasons, supersonic and transonic SBLI may exhibit different mechanisms for the creation of the unsteadiness, but as table 4.1 shows, the similarities in Strouhal number are striking enough that similar mechanisms must be involved and discussion about unsteadiness in supersonic SBLIs can be insightful for transonic interactions. Basically, there are two mechanisms which are suspect for causing low-frequency oscillations. The first one being upstream influences from the incoming boundary-layer, the second one downstream influences from the separated flow. As Piponniau states, see [70], it is a major difficulty to even distinguish shock-motions associated with one with those associated with the other. First the idea of upstream and downstream influences will be described separately. Afterwards, recent ideas that connect the two will be presented.

The idea that upstream perturbations cause shock movements has been entertained for a long time. In 1975, Plotkin, [78], modeled the shock movement as a response to a random upstream perturbation coupled with a linear restoring mechanism and his model was capable of reproducing the wall pressure spectrum. Andreopoulos and Muck, [2], were able to connect the frequency of bursting events in the upstream boundary-layer with the shock passing fre-

author	year	type	Ma	St
Wu & Martin	2006	compr. ramp	2.9	~ 0.008
Dupont et al.	2006	imp. oblique shock	2.3	~ 0.004
Ganapathisubramani et al.	2009	compr. ramp	2.0	~ 0.02
Touber & Sandham	2009	imp. oblique shock	2.3	~ 0.005
Wollblad et al.	2010	transonic bump	0.7	~ 0.01
Pirozzoli et al.	2010	imp. oblique shock	2.28	~ 0.001
Morgan et al.	2010	imp. oblique shock	2.05	~ 0.01
Hadjadj	2012	imp. oblique shock	2.28	~ 0.0033
Grilli et al.	2012	compr. ramp	2.88	~ 0.0039
Brouwer	2015	transonic bump	0.8	~ 0.0039

Table 4.1.: Comparison of Strouhal number for different cases of low-frequency unsteadiness in SBLI. Strouhal number is computed as $St = f\delta/u_0$, where u_0 is the freestream velocity and δ the incoming boundary-layer thickness.

frequency over a pressure sensor at the wall although their measured frequency was likely to high, as noted by Clemens and Narazanaswamy, [15], due to problems with the experimental measuring setup. However, both Wollblad et al. and Wu & Martin, [123,125], found similar results. It is notable that Wollblad and Davidson results were obtained in the case of transonic SBLI over a bump without separation while both other studies looked at supersonic compression ramps. In 2002, Beresh et al. found correlation between the upstream velocity profile and the shock movement. As a fuller velocity profile is more resistant to separation, such a profile would then delay the point of separation and thus move the shock foot downstream. Continuous variations of the upstream profile thus would lead to the shock movement. All these ansatzes essentially treat the shock as a low-pass filter that relates the high-frequency dynamic in boundary-layer to the low-frequency shock motions. In contrast to this Ganapathisubramani et al., [27], used PIV measurements of to identify very long coherent structures, often called *superstructures*, of length $\lambda \approx 50\delta - 75\delta$ in the upstream boundary-layer. Relating the spatial lengthscale to a temporal one, they found that the low-frequency shock motions scale with $u_0/(2\lambda)$. This scaling is consistent with experimental data derived from Dupont et al., [22], and a DNS by Ringuette et al., [84] found coherent structures of comparable lengthscale. However, it is unclear whether the superstructures in the direct simulation may be artifacts of the recy-

cling/rescaling technique used to create turbulent inflow. Also large eddy simulations of Toubert and Sandham, [115], still find low-frequency oscillations in a domain that does not contain coherent structures in the upstream boundary-layer that are longer than 10δ . Therefore such structures cannot be the main source of the low-frequency unsteadiness.

A different school of thought is that the low-frequency oscillations are the generated by the interplay of recirculation bubble dynamics and the shock movement. Possible origins could be a global instability of the bubble or system of self-sustained oscillations within the interaction zone. The idea of vortices being generated at the mixing layer and interfacing with the recirculation bubble has been studied by Piponniau et al., [70]. They propose that an entrainment driven process in the recirculation bubble is responsible for the low-frequency timescales. Vortices at the interface of the recirculation zone entrain low-momentum fluid from the bubble and hence drain the bubble of mass. As recirculated mass is constant over time, this depleted mass needs to be recharged on a characteristic timescale T that relates to large-scale motion of the shear layer near the reattachment point. A similar entrainment based consideration is found in Wu & Martin for the compression ramp case, [125]. On the notion of self-sustained oscillations, Pirozzoli and Grasso did a DNS of a supersonic boundary-layer with a reflected shock, see [77], and found an acoustic feedback mechanism in the interaction region that could be responsible for low-frequency oscillations. Vortical structures are shed in near the separation point and are convected downstream towards the incident shock. The interaction of the vortices with the shock creates acoustic waves which can travel upstream through the subsonic part of the flow and can trigger the shedding of vortices, creating the feedback loop. Although the timescale of the simulation in [77] was too small to cover low-frequency shock oscillations, Toubert & Sandham, [115], also found upstream moving pressure fluctuations in their LES of incident shock which covers multiple low-frequency oscillations. In general, Clemens and Narayanaswamy state in their review of SBLI, [15], that many studies find correlations between downstream pressure and shock movements where the pressure fluctuations precede the shock displacement. However, all these findings have to be taken with caution since the upstream influence acts on the separated flow, which then acts on the shock. In this way, such pressure-shock correlation do not imply causation.

New ideas on the nature of SBLI can be found in modal decomposition of the SBLI phenomenon. Toubert & Sandham, [115] did a linear stability analysis of a reflected shock at $Ma = 2.3$ and found a globally unstable but

non-oscillatory mode associated with the recirculation bubble. The growth rate of this mode was orders of magnitude lower than the typical frequencies of the turbulent boundary-layer. Similar, Pirozzoli et al., [71], did a linear stability analysis and a dynamic mode decomposition of a supersonic SBLL. They also identified the slowly growing non-oscillatory mode and in addition, found weakly damped modes with an oscillating frequency matching the low-frequency oscillations. Their conclusion supports Plotkin's basic idea, [78]. The low-frequency oscillations exist due to the weakly damped modes within the interaction zone. These modes are fed energy by upstream mechanisms like those described in the previous paragraphs. This is supported by the finding of distinct modes associated with turbulent structures in the upstream boundary-layer by Pirozzoli et al., [71], and similar studies by Toubert and Sandham , [115, 116].

Computation of a Transonic Shock-Wave/Boundary-Layer Interaction

This chapter presents the direct numerical simulation of a transonic shock-wave/boundary-layer interaction. The flow is simulated using the conservative finite-difference scheme developed in part I of this thesis. After a description of the specifics of the chosen setup, statistical analysis of the flow is presented in order to gain insight into the main flow features. A low-frequency unsteadiness is identified and the contributing frequencies are quantified.

5.1. Setup and Geometry

The situation studied within this thesis is a model problem for transonic shock-wave/boundary-layer interaction. A subsonic turbulent boundary-layer impinges on a bump-shaped obstacle, the flow is accelerated and a λ -shock forms on top of the bump. The domain layout is a variation of that used in LES simulations and experiments by Wollblad et. al, [123], and Bron, [9]. Compared to their setup, the Mach number of the incoming flow has been increased. This strengthens the occurring normal shock, in accordance with the general description of SBLI in chapter 4, this leads to a separation of the boundary-layer that is strong enough to generate a λ -shock system. The physical domain size is $[L_x \times L_y \times L_z] = [0.86m \times 0.2186m \times 0.078m]$ while the 99% inlet boundary-layer thickness is $\delta_{in} = 0.0072m$. Therefore the domain is

5. Computation of a Transonic SBLI

L_x	L_y	L_z	N_x	N_y	N_z	y_w^+	$\delta_{99_{in}}$
0.86m	0.2186m	0.078m	1920	576	176	0.64 – 0.93	0.0072m
$Re_{\delta_{in}}$	Ma	ρ_0	p_0	B_l	B_h	B_t	M_s
6531	0.7901	1.425	131000	0.184	0.01048	0.0476	1.26

Table 5.1.: Details on the domain, discretization and physical setup of the transonic SBLI simulation.

sized $[119.4\delta_{in} \times 30.36\delta_{in} \times 10.8\delta_{in}]$ in nondimensional units. The beginning of the bump, whose front half is convex while its rear part is concave, is situated at $x = 0.0m$. The turbulent inlet lies at $x = -0.2m$. The shape of the bump is given by the smooth matching of two sixth order polynomials, details on which can be found in [9]. The shape of the bump is defined by three parameters: height, length and the position of the highest point, i.e. the throat of the bump. The geometry of the bump was chosen in such a way as to minimize the extent of a possible recirculation bubble and to yield a supersonic flow region that is completely contained on top of the obstacle. Bump height is $B_h = 0.01048m$, length is $B_l = 0.184m$ and its throat is located at $B_t = 0.0476m$. A sketch of the domain is given in figure 5.1. From this point on, all distances will be nondimensionalized with the length of the bump, B_l . Thus scaled, the domain size is $[4.674B_L \times 1.188B_l \times 0.424B_l]$. The domain is discretized using $[1920 \times 576 \times 176]$ gridpoints. Points are distributed evenly in stream- and spanwise direction. In the wall-normal coordinate, gridpoints are clustered at the wall by a hyperbolic tangent mapping. This mapping achieves a DNS quality resolution of the turbulent boundary-layer with between 10 and 15 points placed within the viscous sublayer, $y^+ < 10$. For the discretization of the derivatives, 8th order central differences in space and 4th Gauss-collocation in time is used. A summary of the domain and flow details is given in table 5.1. This geometry was chosen to address the following goals:

- Eliminate upstream influence via long-scale superstructures as discussed by Ganapathisubramani et al., see [27].
- Eliminate downstream influences not originating with the SBLI system itself, e.g. trailing edge influence, see [50].
- Simulate the full transonic flow field with the contained supersonic region in order to allow downstream influence away from the subsonic part of the boundary-layer.

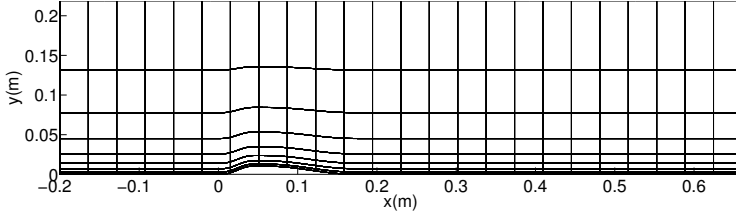


Figure 5.1.: Schematic view of the domain. Lines mark block interfaces of the parallelization.

The state of the incoming turbulent boundary-layer flow is characterized by its freestream values for pressure $p_0 = 131000pa$, density $\rho_0 = 1.425kg/m^3$ and Mach number $Ma = 0.7901$ as well as the Reynolds number $Re_\delta = 6531$ based on inlet boundary-layer thickness.

It must be noted that, although the domain is similar to that used in [123] and [124], direct comparisons are not possible due to the fact that the freestream values of several quantities are different. In addition, the higher Reynolds number of the LES conducted by Wollblad et al. means that viscous effects have larger impact on the results of the direct numerical simulation studied here.

Boundary and Inlet Conditions The wall is modeled as an adiabatic no-slip boundary. Outflow, as well as the upper boundary, are handled using non-reflecting boundary conditions as discussed in section 2.4. To ensure no artificial reflections from the boundaries traveling back into the domain, a small sponge layer is used to supplement the non-reflective conditions, see [105]. This sponge-layer has thickness of 4δ at the outflow and 2δ at the upper boundary. Slightly under-resolved simulations with twice the wall-normal extent have been used to verify that the sponge does not impose any confinement effects on the flow. As discussed in chapter 4, the choice of turbulent inflow conditions is critical in SBLI simulations as some studies link the source of the low-frequency unsteadiness to upstream effects in the incoming boundary-layer. In accordance with the goals described previously, and adapted from the work of Toubert and Sandham, [115], the digital filter approach is used to generate the inflowing turbulence, see chapter 3 for details on the method. The turbulent mean profile as well as the required one- and two-point correlations are taken from the turbulent boundary-layer simulation presented

in section 3.4. The resulting filter has been checked to limit the streamwise lengthscale of generated disturbances to under 1δ . Since the distance between the inlet and the beginning of the bump is $\sim 25\delta$, the turbulent inflow cannot generate coherent structures of a scale that could be related to low-frequency unsteadiness.

5.2. Results of the Transonic SBLI Simulation

Here the results of the SBLI computation are presented. First, the collection of flow-samples is discussed. Then a discussion of the mean flow follows. The structure of turbulence throughout the interaction zone is discussed as well as the properties of the recirculation zone. The low-frequency unsteadiness and shock-motion are found via the discussion of pressure spectra. Finally, different occurring timescales within the interaction zone are discussed in their relation to each other and the shock-motion.

Timescale of the Simulation Once all initial transients have passed, the simulation was run for a nondimensional time of $T = \frac{tu_0}{B_l} \approx 30$, meaning the flow traverses the bump about 30 times.

During this time 768 snapshots of the whole flow field were taken which allow a resolution of Strouhal numbers, $St = f\delta_{in}/u_0$, between $St = 7.7 \cdot 10^{-4}$ and $St = 0.7$. Comparing with results from literature, e.g. [93, 115, 123, 125], this Strouhal number range should be sufficient to resolve all low frequency phenomena taking place within the SBLI complex. In addition, snapshots of the wall quantities were taken with 20 times of this frequency, providing a resolution of Strouhal numbers up to $St \approx 13$, allowing the quantification of all high frequency behavior within the turbulent boundary-layer. If not stated otherwise, statistics were computed at individual locations within the flow and afterwards averaged in spanwise direction as the flow is assumed to be quasi-periodic in this direction. This assumption is supported by observations of the spanwise evolution of all quantities whose largest characteristic spanwise lengthscale was obtained within the interaction zone and is resolved 2–3 times within the computational domain. The lengthscale was computed using the spanwise autocorrelation of streamwise velocity and pressure.

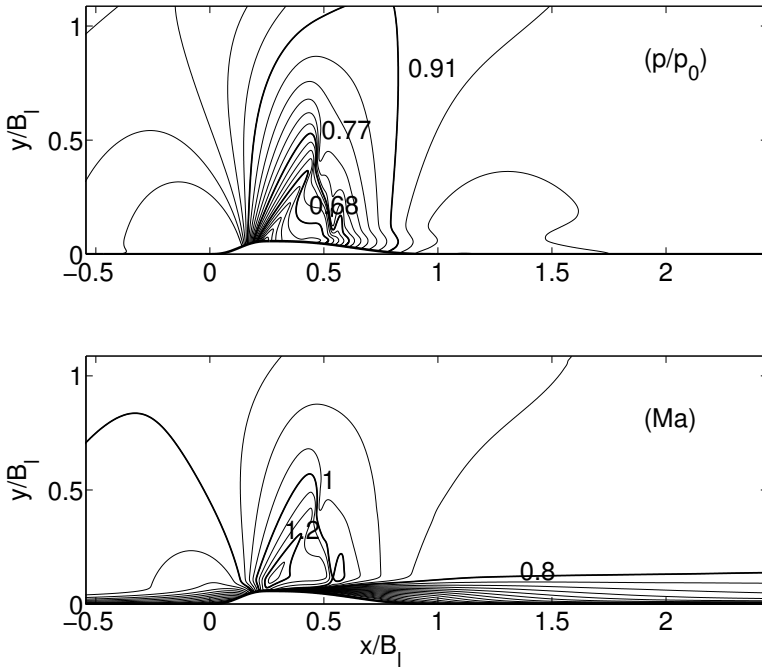


Figure 5.2.: top: mean pressure - 20 equally spaced contourlines between $p/p_0 = 0.572$ and $p/p_0 = 1.03$; bottom: mean Mach number - 25 equally spaced contourlines between 0.0 and 1.25

5.2.1. Mean Flow Description

Before analyzing the transient and oscillatory features of the shock-wave/-boundary-layer interaction, the basic features of the flow are presented. Contourplots of mean Mach number and pressure, see fig 5.2, help visualize the underlying flow mechanics. The λ formation of the shock system is visible in the mean pressure. The Mach number contours show a thickening of the boundary-layer when the upstream influence of the obstacle is felt as well as the following flattening of the boundary-layer due to strong acceleration over the bump. A maximum Mach number of $Ma = 1.26$ is reached at the upstream leg of the shock. It can clearly be seen that the pre-interaction state

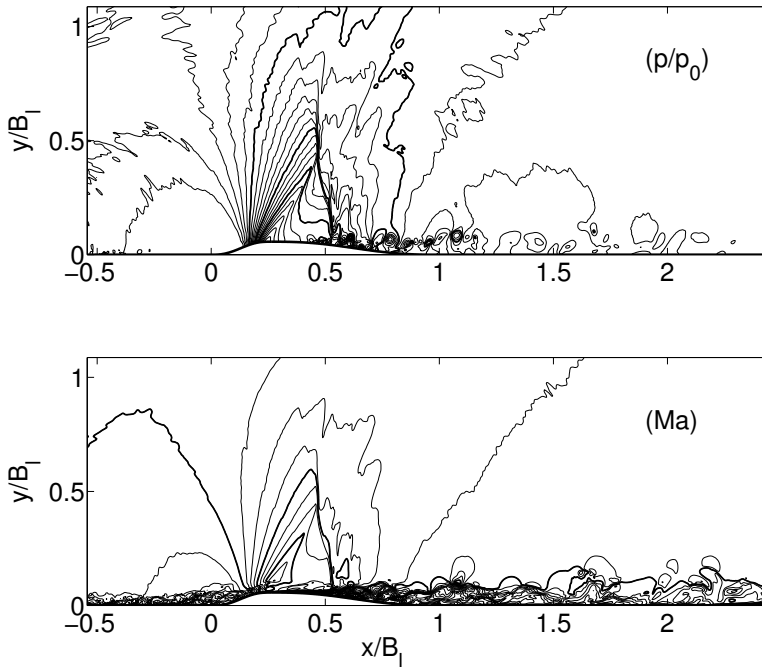


Figure 5.3.: left: instantaneous pressure ; right: instantaneous Mach number - contourlines as in fig 5.2

of the boundary-layer is not recovered within the computational domain as the velocity profile recovers slowly in the downstream direction. The visualization of p and Ma in figure 5.3 show an instantaneous view of the flow field. A shear layer forms behind the bump throat, where a small recirculation bubble has formed and vortices are shed below the downstream leg of the λ -shock. In addition, the mean profile shows the formation of a small supersonic tongue behind the shock, which may occur for transonic SBLI on curved surfaces due to the curvature of the streamlines and, in this case, the additional streamwise velocity introduced by the developing vortices, see chapter 4.

A quantity that is indicative of the mean flow is the evolution of mean wall

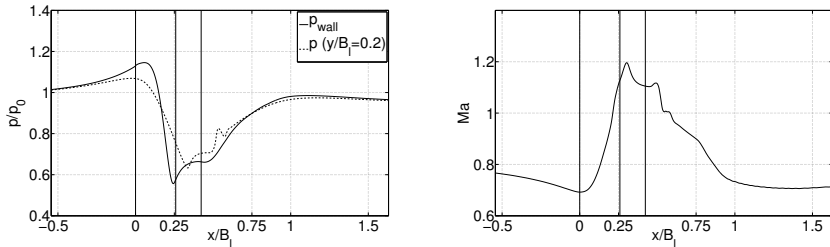


Figure 5.4.: left: Mean pressure profile at the wall and away from the turbulent near wall region; right: Mean Mach number profile at the edge of the boundary-layer.

pressure throughout the domain. It is displayed in figure 5.4. The horizontal lines in the graphs mark the following locations; from left to right: the beginning of the bump; the bump throat; the end of the stable recirculation zone. This notation is continued throughout this chapter for all figures in which the bump geometry is not visible. The pressure at the wall gradually rises upstream of the bump. The location of the front shock can be seen at $x \approx 0.026B_l$ which coincides with the location of the bump throat. The shock location is smeared out in the mean values due to the oscillatory movement of the shock system. When looking at the wall pressure, it is not possible to pinpoint the location of the downstream shock. This is clear when viewing the instantaneous pressure field in figure 5.3. The shedding of vortices takes place at the location of the downstream shock and therefore obscures its location as the pressure gradient does not reach down to the wall. However its mean position near the wall is located at $x = 0.54B_l$. When looking at the pressure away from the wall at $y = 0.2B_l$, the locations of both parts of the λ -shock are visible at $x \approx 0.33B_l$ and $x \approx 0.51B_l$. In addition, the shocklet that terminates the supersonic tongue is visible at $x \approx 0.57B_l$. In transonic shock-wave/boundary-layer interactions, the interaction length is determined by the length of the supersonic region of the shock interaction, measured from the point where pressure first starts to rise up to the point it reaches the critical value indicative of a Mach number equal to 1. Looking at the mean wall pressure in fig 5.4, the interaction length is of an order of 16δ . This is a rather long distance when strong interactions are concerned. However, the wall pressure may not be the best quantity to use for characterizing the interaction zone. The vortices being shed on the downstream part

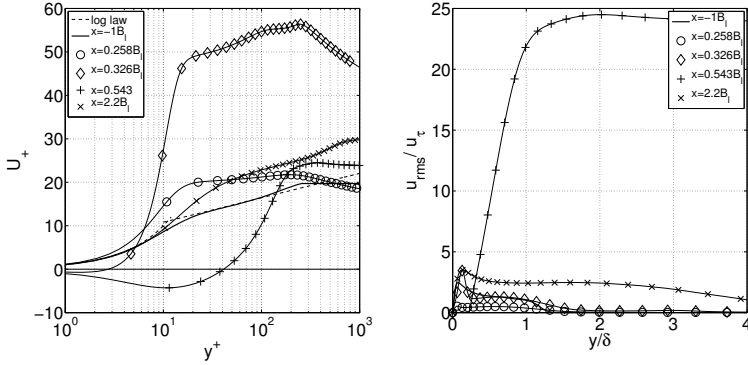


Figure 5.5.: left: Mean streamwise velocity profile in viscous scaling; right: mean streamwise turbulence intensities in outer scaling.

of the bump obscure the influence of the rear shock on the wall pressure and serve to increase the vertical pressure gradient. In figure 5.4 the mean Mach number at the boundary-layer edge is reported in addition to the pressure. Looking at its values, the interaction zone has a length of about 7δ . This value is more in line with the characteristic dimensions observed in strong SBLI.

The mean velocity profiles in viscous scaling reflect this behavior, depicted together with the mean streamwise turbulence intensities in figure 5.5. Figure 5.6 shows a qualitative view of the evolution of the same quantities throughout the interaction zone. Upstream of the bump, the velocity profile of the boundary-layer follows the classical log-law. Near the bump, when the upstream effect of the obstacle manifests itself as an adverse pressure gradient, the typical lifting of the velocity can be observed in the contour plots of Mach number and in figure 5.6. In addition the flow undergoes infrequent, intermittent separation in this region, which explains the divergence from the law of the wall at the start of the bump. At $x = 0.258B_l$, the bump throat, where the maximum velocity is reached, the boundary-layer thickness is at a minimum. The velocity profiles at the rear of the bump reveal the existence of a recirculation bubble with a sharp velocity gradient between recirculating fluid and the rest of the flow. This facilitates the formation of the vortex shedding. The flow recovers downstream of the interaction zone, but the law of the wall extends much further away from wall before a logarithmic behavior

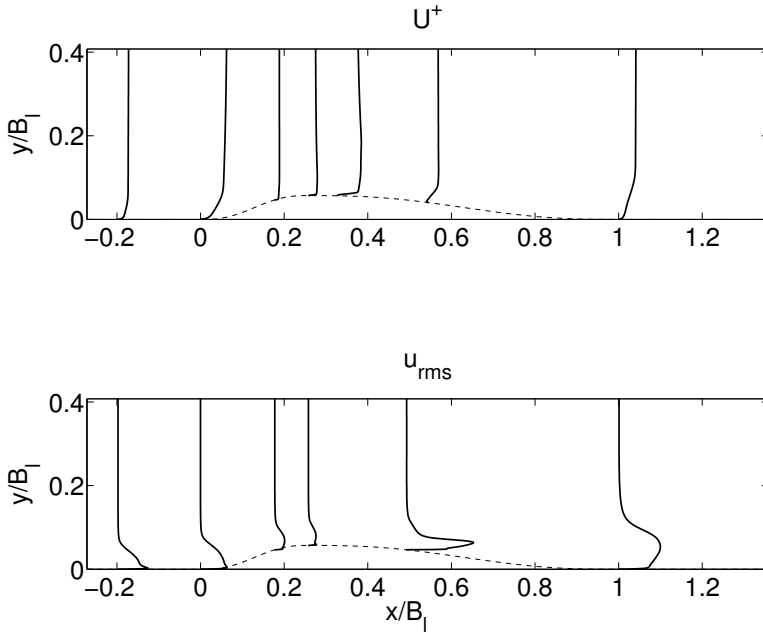


Figure 5.6.: top: Qualitative visualization of u^+ at different streamwise locations throughout the interaction zone; bottom: visualization of u_{rms} profiles throughout the interaction zone.

sets in.

5.2.2. Evolution of Turbulence through the Interaction Zone

The study of turbulence evolution and generation follows. The existence of turbulence is quantified via the turbulence intensities u_i^+/u_τ . Special care is taken to describe the upstream part of the bump where the flow is accelerated and turbulence intensities drop significantly. In addition the anisotropy stress tensor reveals information on the structure of the turbulence within the SBLI.

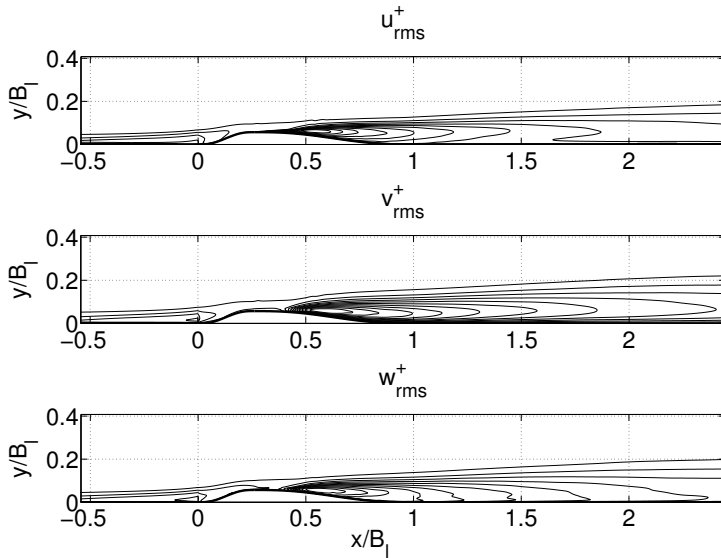


Figure 5.7.: Mean turbulence intensities, u_i^+/u_τ . 13 equally spaced contours between 0 and 20.

The mean turbulence intensities are displayed in figure 5.7. Looking at their contours it is clear that turbulence is mainly generated behind the interaction zone and below the downstream shock. At this position the vortex shedding begins creating mean intensities that dwarf those created within the turbulent boundary-layer, see figures 5.5 and 5.6. As expected, turbulence intensities decrease significantly in the accelerated flow and supersonic flow region as the higher velocity and acceleration serve to drive the flow towards a laminar state. The turbulent energy contained within the vortices can be observed way downstream of the shock system. It is not until $x = 2.17B_l$ that the typical boundary-layer *rms* profile with its peak in the near wall region begins to establish itself again. This behavior is in good agreement with other simulations of transonic SBLI over an obstacle performed by Sandham et al. in [93] or Wollblad et al. [123, 124]. In figure 5.8 the contours of instantaneous streamwise velocity fluctuations u'/u_0 are displayed in a wall parallel plane at a height of $y^+ \approx 10$. The figure gives a clear indication of

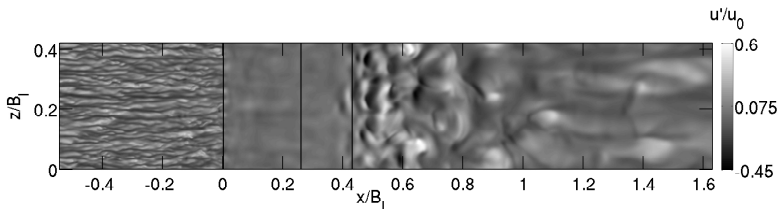


Figure 5.8.: Streamwise velocity fluctuations at $y^+ \approx 10$; Solid lines from left to right: beginning of the bump; bump throat; end of the stable part of the recirculation bubble

the evolution of streamwise flow structures. In the upstream boundary-layer characteristic streaks are visible. Once the flow impinges on the bump and the flow undergoes acceleration, the flow begins to laminarize and velocity fluctuations almost disappear. Fluctuating velocities begin to rise again once the vortex shedding behind the bump throat begins and the region of almost always detached flow ends. There, fluctuations are at a maximum as vortices are generated close to the wall. Further downstream, the eddies detach from the wall and their imprint near the wall is not as strong. However the upstream state of the boundary-layer is not recovered. Starting at $x \approx 1.35B_l$ weak streamwise structures begin to form but their spanwise spacing is about 5 to 10 times larger than in the upstream boundary-layer.

The laminarization process of the boundary-layer on the upstream part of the bump is a critical feature of the flow. It determines the state of the boundary-layer at the onset of the shock impingement. Since turbulent and laminar boundary-layers behave differently when confronted with adverse pressure gradients this is an important question. In general, turbulent boundary-layers resist the adverse pressure gradients better than laminar ones. Therefore the interaction lengthscales of laminar SBLI tend to be larger when compared to turbulent interactions. The interaction lengths observed here compare with turbulent lengthscales but the reduction of *rms* values in front of the shock necessitates further investigation. A first insight into the state of the flow can be gained by looking at the acceleration parameter

$$K = \frac{\mu_e}{\rho_e U_e^2} \frac{\partial U_e}{\partial x}, \quad (5.1)$$

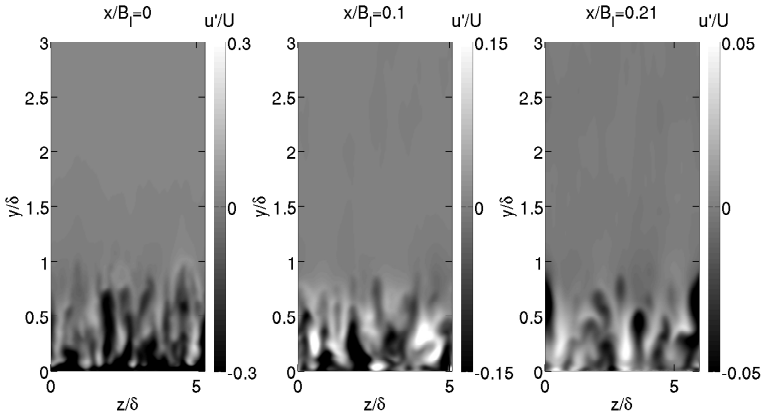


Figure 5.9.: yz -slices of streamwise velocity fluctuations at different streamwise locations on the upstream part of the bump.

see e.g. Jones and Launder in [44]. The subscript e denotes quantities evaluated at the edge of the boundary-layer. Values of $K > 3 \times 10^{-6}$ are regarded as sufficient for relaminarization of the flow. Although this is of course dependent on the streamwise extent for which such values are sustained. In the case investigated here, the evaluation of K indicates values large enough for potential relaminarization from $x/B_l = 0.04$ up to $x/B_l = 0.3$. This amounts to a distance of 6.6δ and spans the upstream side of the bump until just after the bump throat. This analysis is not conclusive but suggests that the flow begins to laminarize but the streamwise extent of the region with high enough acceleration is too short to reach a laminar state. Figure 5.9 depicts yz -slices of scaled streamwise velocity fluctuations, u'/U , in the region of accelerated flow. The pictures show that the general structure of the flow remains unchanged although the amplitude of the fluctuations decreases by a factor of 6. This is supported by figure 5.10 which depicts profiles of turbulence intensities at the same positions as well as a wall-normal plane of velocity fluctuations scaled by u_τ . The wall-normal slice of streamwise velocity shows that coherent structures with long streamwise extent prevail up to the point of the impinging shock although they do not retain the original shape of the boundary-layer streaks. The visualizations make it clear that the streamwise extent of the acceleration is too short to fully laminarize the flow and that it is in a transitional state. However, the overall shape of the shock-interaction

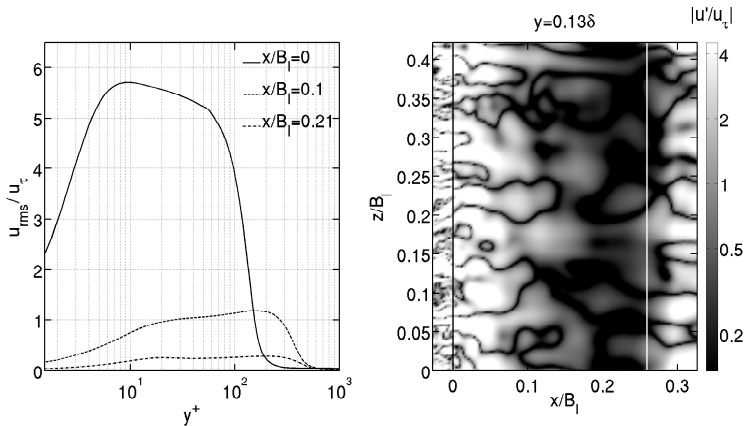


Figure 5.10.: left: u_{rms} profiles on the upstream part of the bump; right: a wall-normal plane of streamwise velocity fluctuations in logarithmic scaling.

and the occurring length and timescales suggest that the interaction must be considered in the context of turbulent shock-wave/boundary-layer interactions.

To characterize the structure of the turbulence throughout the SBLI, the invariants of the anisotropy stress tensor,

$$b_{ij} = \frac{\overline{u'_i u'_j}}{2k} - \frac{1}{3} \delta_{ij}, \quad (5.2)$$

are computed and depicted in figure 5.11. The Lumley triangle shown in addition to the invariants presents the realizable values of the anisotropy stress tensor invariants $-II$ and III . The edges of the triangle and their intersections mark special states of the turbulence. The top (blue) line marks a state of two component turbulence, the left (red) line is a zone of axisymmetric compression, the right (green) line marks axisymmetric expansion. The origin of the triangle marks a state of isotropic turbulence. The blue/red intersection characterizes an axisymmetric two component state of turbulence, while the blue/green corner demonstrates pure anisotropic, one-component turbulence. The state of turbulence in the upstream boundary-layer at $x = -0.54B_l$ shows the typical behavior for zero pressure gradient boundary-layers, see [80] or [76]. The maximum anisotropy is reached at $y^+ \approx 10$, while the flow in the outer layer returns to an isotropic state. In the acceleration region, at

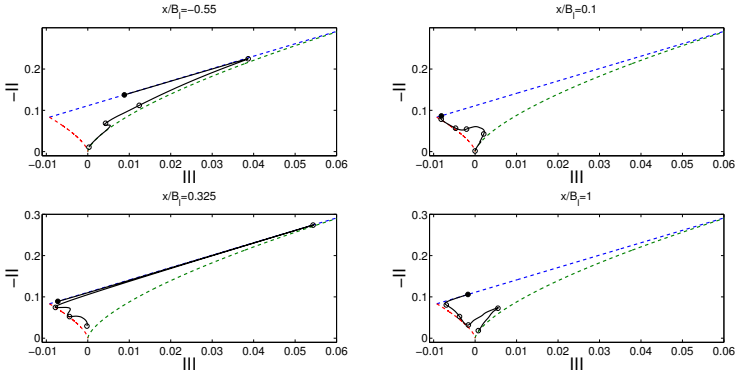


Figure 5.11.: Invariants of the anisotropy stress tensor; full black circle marks value at the wall, first empty circle marks point at $y^+ \approx 10$ except in the lower left where it marks the u_{rms} peak within the recirculation bubble.

$x = 0.1B_l$, the anisotropy is reduced. The flow is purely two-component at the wall. The forced upward curvature of the flow destroys the anisotropy by magnifying the ratio of wall-normal velocity fluctuations to streamwise fluctuations. The flow undergoes a phase of axisymmetric compression away from the wall before returning to isotropy in the freestream. The diagram at $x = 0.325B_l$ cuts through the small recirculation bubble forming behind the throat. Within the bubble, streamwise velocity fluctuations dominate all other parts of the tensor and a strong anisotropy is present. The axisymmetric compression above the recirculation zone is indicative for a turbulent mixing layer, e.g. [80], which develops at the sharp interface of the recirculation and the freestream flow, see fig. 5.5. Apart from the presence of the flow-reversal this behavior is repeated in the wake of the bump at $x = 1B_l$. In fact, the increased spanwise fluctuations due to the larger vortices being shed behind the shock system strengthen the axisymmetric compression of the fluid near the wall. The structure of the invariants resembles a mixing layer in the near wall region. In the outer layer of the boundary-layer, anisotropy is strengthened and assumes values comparable to those of the upstream boundary-layer before returning to isotropy in the freestream.

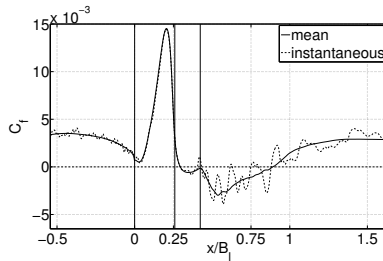


Figure 5.12.: Streamwise evolution of mean and instantaneous skin friction coefficient C_f .

5.2.3. Flow Separation

Flow separation is a common feature in shock-wave/boundary-layer interaction. The strong adverse pressure gradient introduced by the shock impinging on the boundary-layer serves to detach the flow from the wall. In general, a shock Mach number of about $Ma_s = 1.3$ leads to the formation of a recirculation bubble. This behavior can however be changed e.g. by the specific geometry studied. As the peak Mach number in the situation detailed in section 5.2.1 is $Ma_s = 1.26$ one would generally not expect a strong recirculation zone. The presence of recirculation is most commonly characterized by the wall friction coefficient $C_f = \tau_w / (\rho_0 u_0^2)$. A C_f value of zero marks a region on incipient separation while negative values indicate fully separated flow. Figure 5.12 shows the evolution of C_f throughout the interaction zone. When viewing the mean skin friction, a large separated region can be identified that ranges from just behind the bump throat at $x = 0.28B_l$, where the leading shock impinges on the boundary-layer to almost the end of the bump at $x = 0.89B_l$. This region is far larger than expected for the shock Mach number encountered here. However, looking at the depiction of C_f in more detail, it can be seen that there is a region where the flow is almost reattached at $x = 0.423B_l$ and that the profile of skin friction is highly intermittent after that point. Figure 5.13 illustrates the flow field within the recirculation bubble. First of all, note that the wall-normal extension of the recirculation bubble is quite small, being of the order of $\delta_{in}/3$. Second of all, starting at about $x = 0.038B_l$ the shedding of vortices begins on the downward slope of the bump, certainly influenced by the introduction of strong shear forces in the mixing layer between main and recirculating flow. Therefore the large

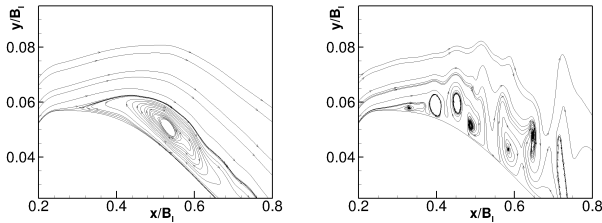


Figure 5.13.: left: Streamlines calculated from the mean flow; right: streamlines calculated from an instantaneous flow field; note the different scaling of x - and y -axis.

second part of the recirculation zone visible in fig. 5.12 is characterized by large vortices rolling down the slope of the bump until finally detaching from the wall at $x \approx 0.89B_l$. Another way to look at this is using tools of probability analysis, see fig. 5.14. The probability density function of C_f shows a region of very small variance for the skin friction up until $x = 0.38B_l$. With the onset of the vortex shedding there is a huge increase in variance of C_f and the region of intermittent detachment begins. Also displayed is the probability for the flow to be detached. The segmentation of the recirculation region into two distinct entities is visible as well. The very small recirculation bubble between the impinging shock and the beginning of the vortex shedding will be referred to as the region of stable recirculation. In the second, much larger region with mean $C_f < 0$, the recirculation is due to the presence of intermittently generated vortices. This region will be referred to as the region of intermittent separation. It has to be noted that the onset region of the vortex shedding coincides with the position of the downstream leg of the λ -shock although the shock itself does not reach down to the wall, see figure 5.2. Not shown in the above depictions is a region of very infrequent separation at the onset of the bump at $x = 0$. Due to the strong adverse pressure gradient and the geometry change at that point, the flow displays $P(C_f < 0) = 0.25$ at $x = 0$. This serves to explain the high values of turbulence intensities visible in fig. 5.10.

5.2.4. Spectral Analysis

To begin the analysis of the shock motion, the temporal evolution of the streamwise pressure is investigated. In figure 5.15 the streamwise pressure

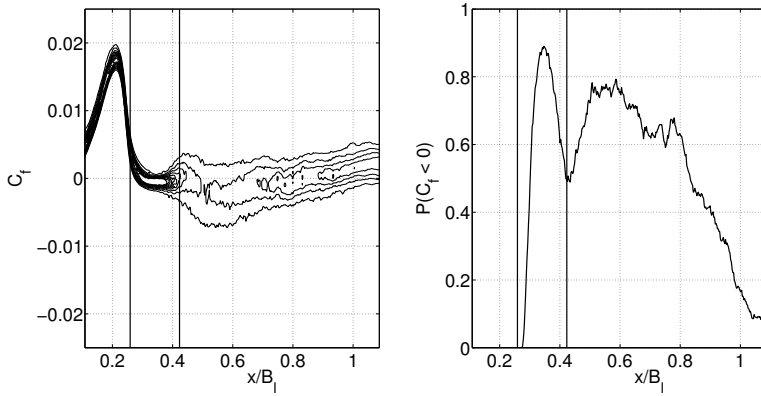


Figure 5.14.: left: PDF of C_f , 10 contour levels equidistant between 50 and 500; right: streamwise probability of detached flow.

signal is plotted over a time. In this figure all major flow phenomena that take place over the interaction zone can be observed. First of all the high frequency pressure oscillations typical for the upstream boundary-layer are visible where structures are transported along the wall with the bulk velocity of the turbulent boundary-layer. Beginning with the rise of the obstacle at $x = 0$, the transport of these structures is accelerated as the overall velocity of the flow rises. Roughly at the location of the bump throat there is a structural shift in the pressure signal. At this position the front leg of the λ -shock impinges on the wall and a low frequency oscillation of the pressure in time is visible. At the rear end of the stable recirculation zone, upstream traveling waves are generated that travel through the interaction zone until being absorbed by the shock at the bump throat. The end of the stable recirculation zone marks the point where the vortex shedding begins. Vortices are generated with a higher frequency in the interaction zone and begin to diffuse and merge further downstream in the wake of the bump. A notable absence in this depiction of pressure is the location of the rear leg of the shock system. When comparing with the mean pressure field in figure 5.2, it can be seen that the strong pressure gradient does not reach down to the wall and is obscured by the strong pressure fluctuations due to the vortex generation in the region of intermittent separation at $x \approx 0.43B_1$. A clear view of both shock feet and their movement can be gained by taking the instantaneous

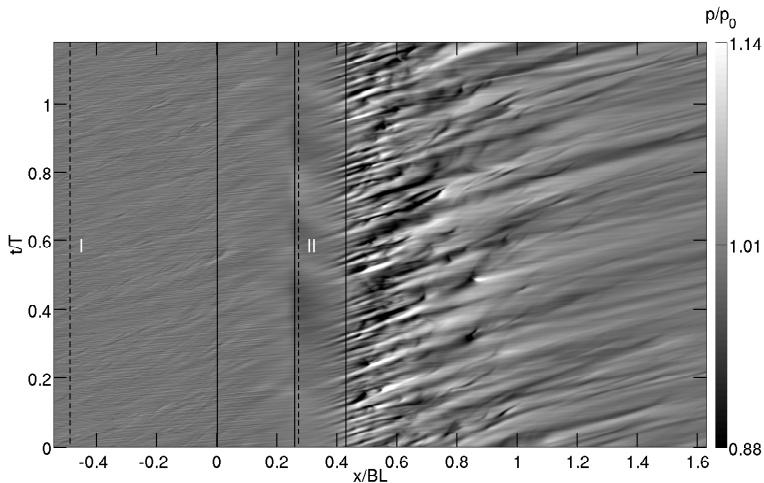


Figure 5.15.: Temporal evolution of instantaneous normalized wall pressure; solid lines from left to right: beginning of the bump - bump throat - end of the stable part of the recirculation bubble; I: upstream ZPG boundary-layer; II: location of the leading shock. T is the timescale associated with the lowest occurring frequency.

pressure signal away from the wall. Figure 5.16 depicts pressure away from the wall at $y = 0.16B_l$. Here the rear shock is clearly visible at $x = 0.51B_l$. The position of the front shock has shifted downstream as dictated by the λ form of the shock system. Also visible is the small shocklet behind the λ -system. Of interest here is that upstream traveling pressure waves are generated behind the shocklet and upstream communication is visible between the shocklet and the rear shock as well as between both λ -shocks. As the flow is supersonic in this region, this change in pressure is likely induced by pressure fluctuations traveling around the supersonic region that imprint the pressure modulation from above. The presence of such waves will be seen later once the behavior of pressure fluctuations is discussed. Although difficult to see in figure 5.16 these pressure waves continue to travel upstream into the upstream boundary-layer and will be investigated further in the following sections.

To identify the occurring frequencies, figures 5.15 and 5.16 are transformed into frequency space. The qualitative change of pressure oscillations over the course of the interaction zone is visible in figure 5.17. The premultiplied power

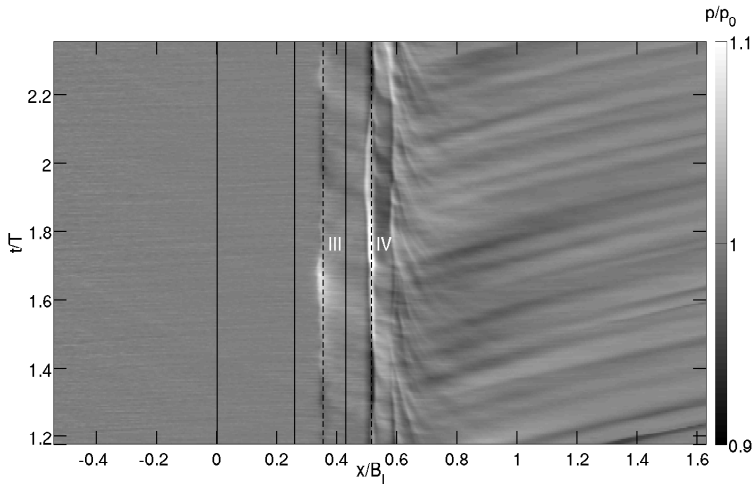


Figure 5.16.: Temporal evolution of instantaneous normalized pressure at $y = 0.163B_1$; solid lines as in fig 5.15; III: position of the leading shock; IV: position of the rear shock wave.

spectral density of the pressure signal is plotted over each streamwise location throughout the interaction zone. This allows the identifications of the frequencies containing the most energy. In the upstream boundary-layer the energy of the fluctuations is centered around Strouhal number $St = \frac{\delta_{99}^y f}{u_o} \approx 1$ as is typical for zero pressure gradient boundary-layers. The peak in Strouhal number is slightly larger than the typical value of 1. This may be attributed to the upstream influence of the bump which is felt as an adverse pressure gradient imposed on the boundary-layer. Starting with the rise of the obstacle the occurring frequencies shift downward until the lowest frequencies are encountered around the bump throat where the leading shock impinges on the boundary-layer. At this position the spectrum shows two distinct low frequency peaks at $St = 0.0078$ and $St = 0.029$, see figure 5.18 for a detailed view of the spectrum. Following the impingement point higher frequencies of order $\mathcal{O}(10^{-1})$ are contained within the recirculation region. Following the point of the vortex shedding, energy is distributed over a wide range of Strouhal numbers spanning the range from $\mathcal{O}(10^{-2})$ to $\mathcal{O}(10^{-1})$. In the wake, a peak frequency for the vortex shedding of $St \approx 0.077$ establishes itself. It is clear that the low frequency movements of the terminating λ -shock do not

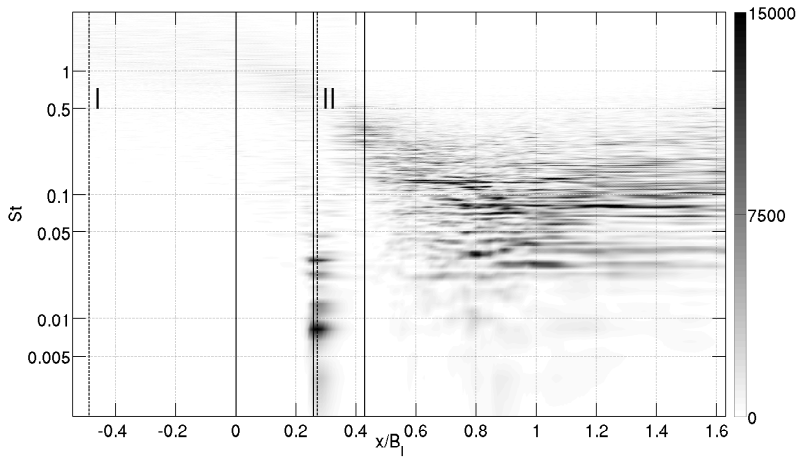


Figure 5.17.: Spatial evolution of premultiplied power spectral density of wall pressure fluctuations. PSD is normalized such that the integral over the spectrum is unity for all streamwise positions. ; lines as in figure 5.15

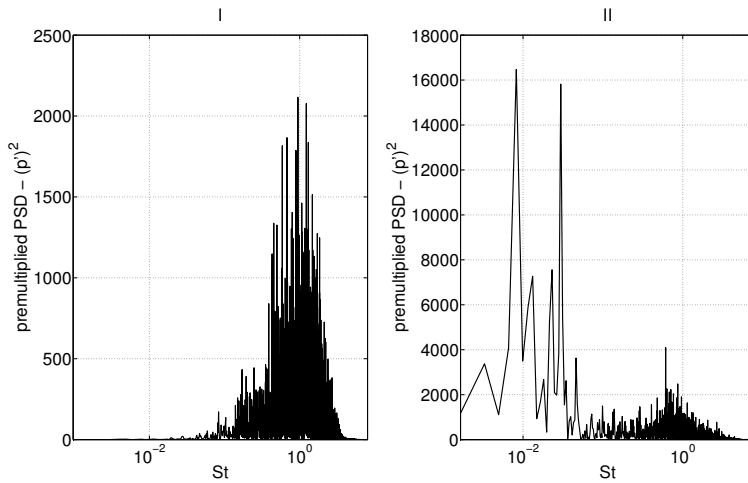


Figure 5.18.: Premultiplied PSD of wall pressure: I: upstream boundary-layer; II: leading shock wave.

reach down to the wall as there is no significant energy peak in the region below the shock itself. The movement of both shock feet is more pronounced in the premultiplied PSD of pressure away from the wall at $y = 0.163B_l$ in figure 5.19. The most important qualitative change in the spectra is the appearance of low frequency peaks at the positions both of the second shock as well as the shocklet trailing the interaction. The spectra at those positions contain two distinct peaks in the Strouhal number range of $\mathcal{O}(10^{-3})$, as displayed in fig. 5.20. The first one, located at $St = 0.0078$ matches the peak frequency of the leading shock while the second one, located at $St = 0.0039$, is of even lower frequency. While there is a small plateau in this regime at the location of the leading shock, it is not nearly as pronounced. However, figure 5.19 allows a clear interpretation of the peak at $St = 0.029$, which is approximately 8 times the low-frequency peak, in the wall pressure spectrum. This frequency is sustained throughout the whole region between both shockfeet with undiminished energy. Comparing with figure 5.16, it is reasonable to assume this marks the frequency of the upstream traveling disturbances. The range of Strouhal numbers encountered here is consistent with observations of Grilli et al., [31], and Dupont et al. in [22] who investigated SBLI with separation within supersonic compression ramps. Although these situations are different in a number of ways, notably the presence of just a single shock, the frequency behavior of the leading shock, situated just ahead of the separation bubble, matches that of those encountered in other types of SBLI. The diagrams of power spectral density also allow a convenient measurement of the range of the shock motion. At the wall, the leading shocks motion spans a range of approximately 2.5δ . Moving away from the wall, the range of motion naturally decreases as the λ -system narrows towards the triple point. At the top measuring station its range is 1.5δ while the terminating shocks oscillating range is roughly 1.2δ which matches the experimental observations of Bron, [9], in a similar configuration.

All spectra shown in this section have been computed without any spectral averaging methods. This is done to preserve the full range of observable Strouhal numbers. Welch averaging of the spectrum reduces the frequency range but provides a clearer picture of the resolved area. To conclude this section, figure 5.21 presents a look at the spectral density of wall pressure with applied Welch averaging. It provides a clearer picture of the dominant frequencies in the area of vortex shedding and in the upstream boundary-layer.

As said in chapter 4, the effect of the shock-wave/boundary-layer interaction on the general flow field is often likened to that of a low-pass filter. It

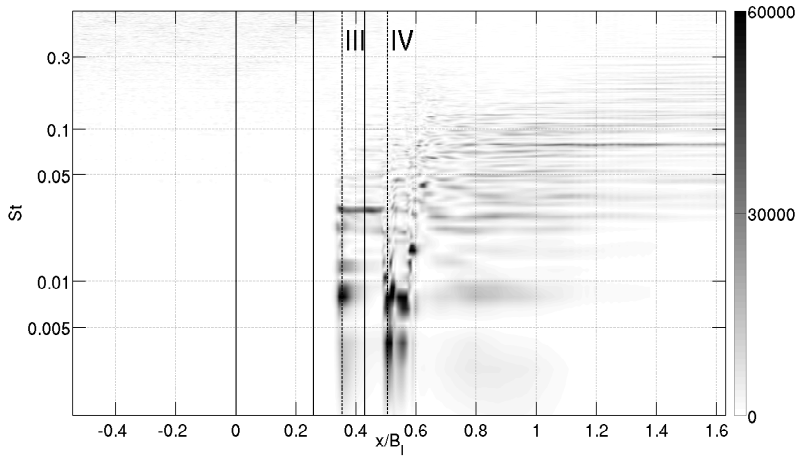


Figure 5.19.: Spatial evolution of premultiplied power spectral density of pressure fluctuations at $y = 0.163B_1$; lines as in fig 5.16;

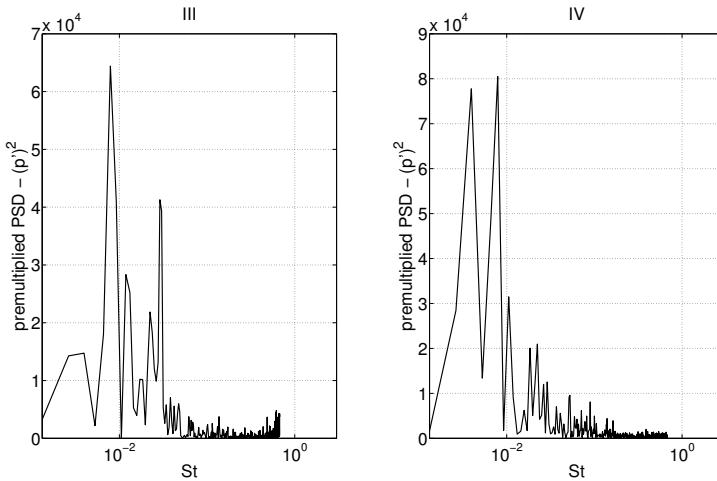


Figure 5.20.: Premultiplied PSD of pressure at $y = 0.03$: III: leading shock wave; IV: terminating shock.

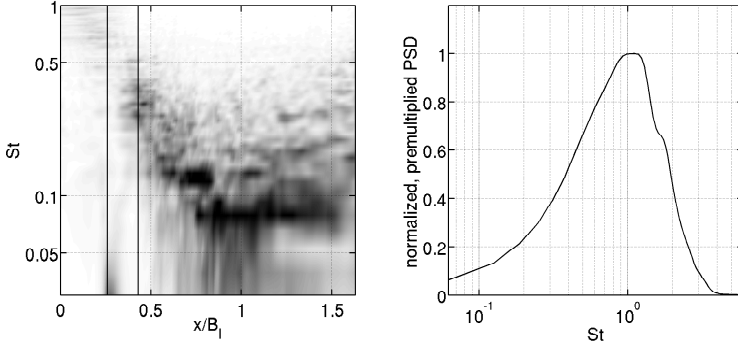


Figure 5.21.: left: Contourplots of normalized, premultiplied PSD of wall pressure; right: normalized, premultiplied PSD of wall pressure in the upstream boundary-layer.

amplifies the low-frequencies while damping the higher ones. This effect can be quantified by computing the transfer function of the SBLI system which is displayed in figure 5.22. It is computed by taking the pressure spectra at locations before and after the shock-system at $x/B_l = -0.6$ and $x/B_l = 2.3$. Although the specific shape of the transfer function is dependent on the location of the input and output spectrum, the general shape of the function

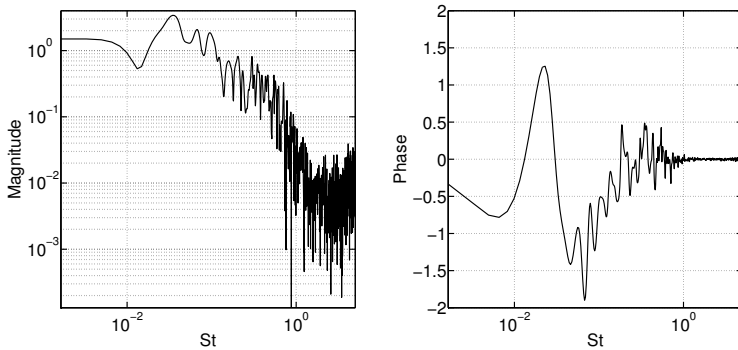


Figure 5.22.: Transfer function of the SBLI system computed from pressure signals at $x/B_l = -0.6$ and $x/B_l = 2.3$. left: amplitude; right: phase.

displayed here is representative of all transfer function derived from other stations. While the low-frequency shock movements are the dominant frequencies within the SBLI the influence of the interaction zone is not felt for very long streamwise distances. The shock frequencies retain their upstream amplitudes. The frequencies amplified the most through the SBLI are, corresponding to the first three peaks in the transfer function of amplitude: The frequency found within of the upstream traveling disturbances within the λ -shock at $St \approx 0.03$ and the two main Strouhal number peaks in the region of vortex shedding behind the bump at $St \approx 0.077$ and $St \approx 0.12$, see 5.21. These findings suggest that the frequency at $St \approx 0.03$ is not restricted to the upstream traveling disturbances observed in the timeseries of pressure. The peak in the transfer function indicates some downstream propagating mechanism connected to this frequency.

5.2.5. Connecting the Timescales

In the previous section the general behavior of the λ -shock system was discussed using the spectral behavior of pressure. The aim of this section is to identify all occurring timescales within the interaction zone and establish possible links between the viscous near-wall flow and the shock system. The relevant timescales at different regions within the interaction zone will be obtained via the autocorrelations of pressure R_{pp} and streamwise velocity R_{uu} . The correlations are taken at the foot of the leading shock (a), within the stable recirculation bubble, (b) as well as below the terminating shock, (c). These measurements are taken at a distance from the wall that corresponds to a distance of approximately $0.02\delta_{in}$. In addition, a probe is taken away from the wall within the terminating shock at $y = 0.163B_l$, (d). The position of these probes, as well as those of others used throughout section 5.2.5, are displayed in figure 5.23. Once the autocorrelations are computed, their power spectral density is taken to obtain the relevant timescales. Figure 5.24 presents this information. First of all, note that at the shock positions (a) and (d) the velocity and pressure spectra look almost identical. At these positions the low-frequency shock motions seem to dominate all features of the flow. The peaks in the spectra agree with those observed in the examination of the pressure signal in the previous section at $St = 0.0078$ and $St = 0.0039$ although the lowest frequency is not as dominant in the leading shock. In (b) and (c), away from the shocks themselves, pressure and velocity timescales decouple. The dominating velocity timescales within the recirculation bubble are located at $St = 0.017$ and $St = 0.025$. However, the timescales of pressure

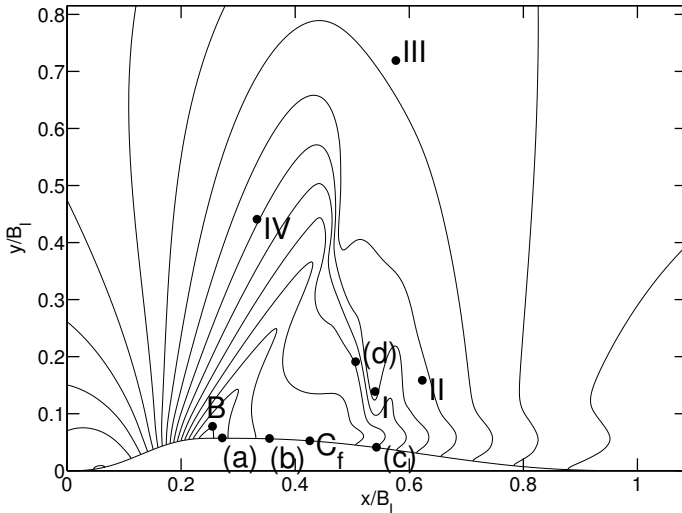


Figure 5.23.: Mean pressure contours and overview of measuring positions used for various correlations throughout section 5.2.5

show a main frequency of $St = 0.0079$ that corresponds to the movement of the leading shock signifying that the wall pressure is imprinted from above the bubble. The measuring station (c) sits within the region of vortex shedding. The pressure signal is evenly distributed in the range $St \approx 10^{-1}$ while the velocity displays significantly lower peaks corresponding to the characteristic timescales within the stable recirculation bubble and the upstream traveling pressure waves.

However there might be other mechanisms at play coupling or facilitating the movement of both shock feet. A prime suspect is the action of the recirculation bubble. The shedding of vortices by the recirculation bubble can be inferred by looking at the position of the local minimum for the probability of separated flow at $x = 0.43B_l$. Computing the spectrum of the indicator function

$$I_{C_f}(t) = \begin{cases} 1, & C_f(x = 0.43B_l, t) < 0, \\ 0 & \text{else,} \end{cases} \quad (5.3)$$

as in [124], shows a significant peak in frequency for the detachment of the recirculation bubble at $St = 0.029$, see fig. 5.25 (a). The rest of the spectrum is concentrated in higher frequencies. While the peak frequency is an order of magnitude larger than the frequencies of the oscillations of the terminating shockwave, both phenomena might still be connected. An upstream mechanism influencing the rear shock is easy to imagine. However, interaction in the other direction is possible as well. Elliptic leakage denotes information that travels upstream from the shock through the subsonic boundary-layer. An indication for the fast action of the recirculation bubble to influence or even cause the slow moving shock oscillations, whose autocorrelation spectrum can be seen in 5.25 (b), can be found within the crosscorrelation of both signals. Suppose the fast shedding of the recirculation bubble causes the shock movement then the spectrum of their crosscorrelation would display a peak at the frequency of the slow phenomenon. Figure 5.25 (c) displays this peak in the crosscorrelation of I_{C_f} and the rear shock position. While this is certainly no proof of causality, it is an indication of the coupling of both frequencies.

Interestingly, the crosscorrelation of I_{C_f} with the position of the leading shock in 5.25 (c) shows a different shape. Its peak is located at $St = 0.029$ with smaller plateaus at the shock frequencies themselves. This implies, that the faster frequency of the recirculation bubble is already contained within the signal of the shock movement, as is the case, see 5.25 (e), where the autocorrelation spectrum of the leading shocks movement is shown.

At this point, a natural question is that of the origin of the $St = 0.029$ frequency. A mechanism that is often discussed in the context of shock-wave/boundary-layer interaction is the bursting frequency of the upstream boundary-layer, e.g. [123, 125]. A burst being an event of significantly increased Mach number in the outer layer of the boundary-layer. Wu and Martin, [125], propose the following methodology to identify bursts. A probe measuring the local Mach number is placed upstream of the shock at a height of $0.5\delta_{99}$. From the Mach number timeseries an indicator function $B(t)$ is constructed via

$$B(t) = \begin{cases} +1, & Ma(t) > \overline{Ma} + \sigma/2; \\ -1, & Ma(t) < \overline{Ma} - \sigma/2; \\ 0 & \text{else,} \end{cases} \quad (5.4)$$

where \overline{Ma} is the mean Mach number and σ is the standard deviation. The probe is placed at $x = 0.25B_l$ and the spectrum of its autocorrelation is displayed in 5.25 (d). The peak bursting frequency is located at $St = 0.029$,

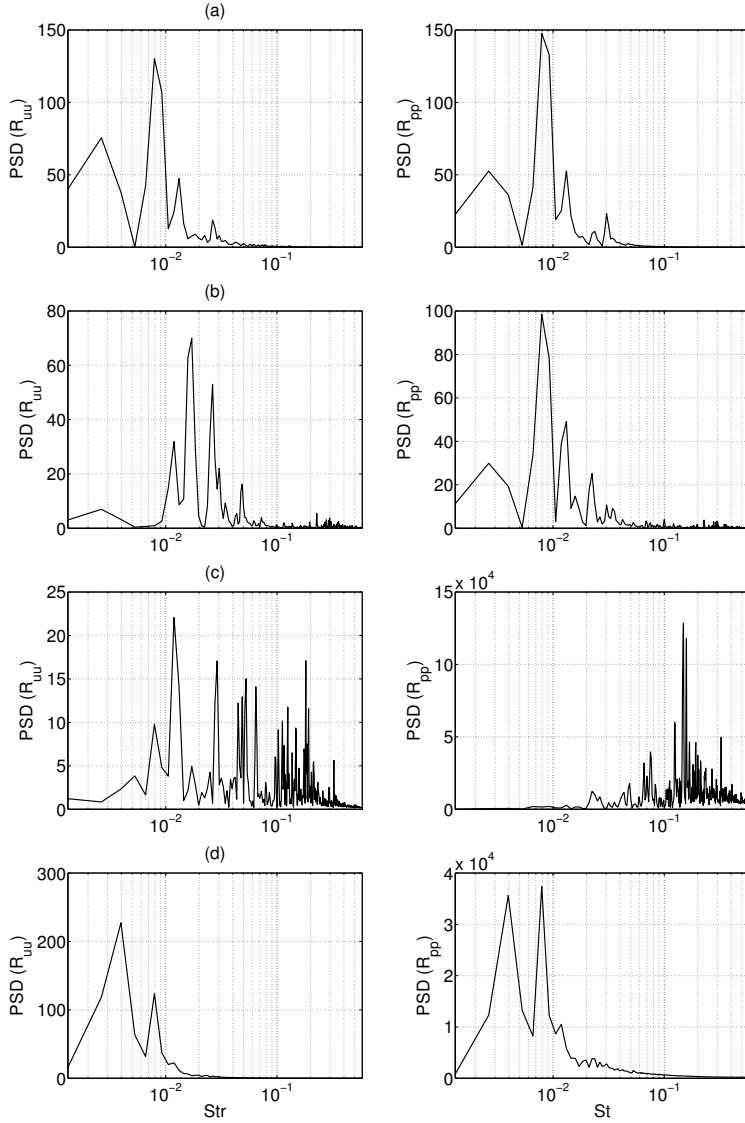


Figure 5.24.: Power spectral densities of velocity and pressure autocorrelations taken at positions (a) - (d) as detailed in fig. 5.23

which is exactly the frequency of interest in the previous observations. The crosscorrelation of the bursting frequency and the leading shock position in 5.25 (f) shows two distinct peaks at $St = 0.029$ and $St = 0.0079$, which correspond to the frequencies of the bursting and the shock movement respectively. This indicates that the low frequency of the shock movement might be already contained within the bursting frequency and that the leading shock displays small amplitude oscillations with the higher bursting frequency. These findings strengthen the thesis that bursting is responsible, or at least influencing, the low frequency shock movements in SBLI. A note of caution must be given here. There is a discrepancy of the peak bursting frequency of $St = 0.029$ with the typical value of $St \approx 0.14$ found in the literature, e.g. Wu & Martin in [125]. This can be explained with the position at which the frequency is taken. The boundary-layer at $x = 0.25B_l$ is very different from the normal flat plate boundary-layer. It has undergone acceleration, compression and laminarization through the bump and might be influenced by small scale fluctuations of the leading shock. The bursting frequency in the undisturbed upstream boundary-layer is of the expected magnitude.

The bursting frequency of $St = 0.029$ is very interesting. It is found at multiple points within the interaction zone. As discussed before, the bursting events might influence the movement of the leading shock. This frequency is also found within the action of the recirculation bubble. It is conceivable that the pockets of high Mach number being transported through the interaction zone trigger the reattachment or spilling of the recirculation bubble. However, as has been seen in the discussion of power spectral density of pressure in figures 5.16 and 5.19 it is also the frequency of the upstream traveling pressure disturbances. The auto- and crosscorrelations of pressure just before the terminating shock at $x = 0.43B_l$ and streamwise velocity at the position of the bursting sensor show clear peaks at the bursting frequency, see figures 5.25 (g)-(i). It therefore seems reasonable to assume that the impact of either the high Mach number packages or the shed vortices at the terminating shock generates flow structures which travel upstream around the λ -shock through the subsonic part of the flow. Figure 5.26 shows contours of instantaneous pressure fluctuations. The figure, paired with additional time-resolved visualizations of pressure fluctuations, shows pressure waves wrapping around the shock system being created in the region behind the rear λ -foot and surrounding the shocklet that terminates the supersonic tongue. On the upstream side of the shock, these waves invade the supersonic region. Their direction is perpendicular to the front shock and thus the waves are seen as upstream traveling disturbances within the interaction zone, see fig. 5.15 and

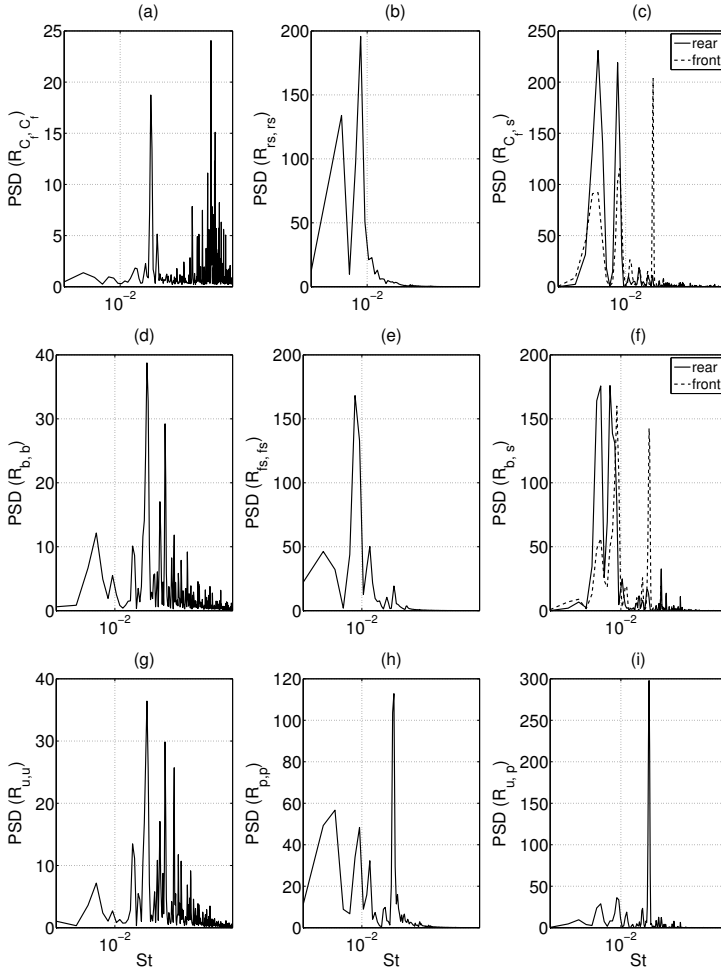


Figure 5.25.: Power spectral densities of auto- and crosscorrelations of recirculation bubble detachment [C_f] in graphs (a) and (c); both shock positions [f_s, r_s] in graphs (b)-(c) and (e)-(f); bursting frequency [b] in graphs (d) and (f), as well as pressure and velocity signals under the λ -foot, [u, p], graphs (g)-(i).

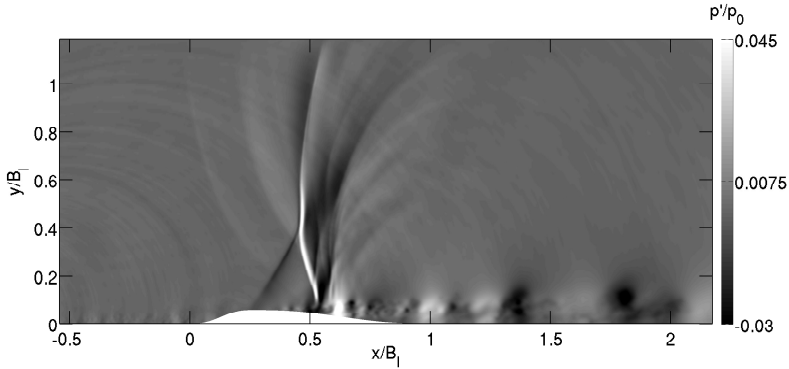


Figure 5.26.: Contours of normalized instantaneous pressure fluctuations.

5.16. In addition, pressure fluctuations can be seen originating from the inlet. These spurious waves are generated by the inlet conditions. Their amplitude however is much lower than that of the physical waves coming from the interaction region. Their frequency and amplitude does not figure significantly in any pressure spectra taken away from the inlet. Therefore, the influence of these waves on the main flow is neglected.

Analysis of the timescales of these vortices and their origin is carried out in the following. The pressure signal at the points *I* through *IV*, as shown in fig. 5.23, is carried out through the investigation of the spectral properties and their autocorrelations. As the waves move counterclockwise around the interaction zone, the analysis begins at the origin of the waves behind the terminating λ -leg. Figure 5.27 (a) shows the spectrum of the autocorrelation at station *I* which is situated within the supersonic tongue. As expected, the spectrum shows significant peaks at the shock frequencies. The only other frequency that contributes to the spectrum is the bursting frequency of $St = 0.029$. Although its amplitude is small compared to the low frequency oscillations, it is the only frequency that can correspond to pressure disturbances generated in this region that travel upwards through the funnel created between the rear shock and the shocklet. Upon leaving the supersonic tongue in point *II* the spectrum diversifies, see 5.27 (b). Apart from the shock and bursting frequencies peaks at $St = 0.017$ and $St = 0.034$

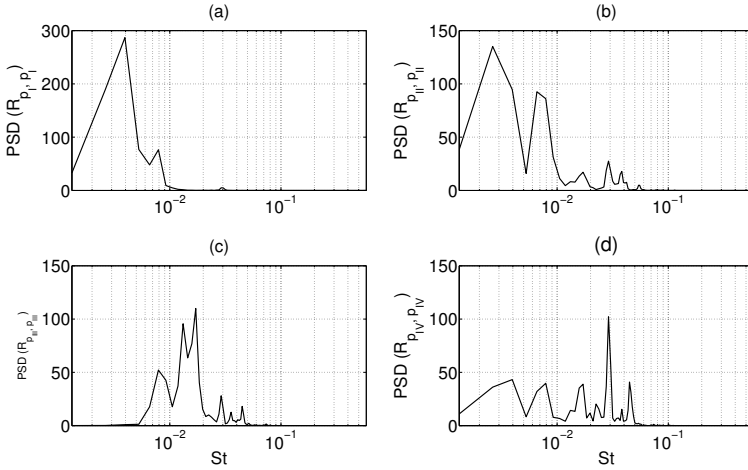


Figure 5.27.: Power spectral densities of pressure autocorrelations taken at positions *I-IV* as shown in fig. 5.26.

appear. The absence of these within the supersonic part of the wake might indicate that these either belong to the subsonic vortex street in the wake or are generated by the interaction with the shocklet. Indifferent from their origin the pressure fluctuations travel upwards and upstream where they are the major contributor to the power spectrum at station *III*. The shock fluctuations are less pronounced far from the wall and the lowest frequency of $St \approx 0.0039$ is missing altogether, 5.27 (c). On the upstream side of the shock at point *IV* and figure 5.27 (d) the dominating frequency has shifted to the bursting frequency.

5.3. Conclusion

Within this chapter, the flow of a transonic shock-wave/boundary-layer interaction has been studied. The mean flow revealed the existence of a λ -shock on top of the bump. The length of the interaction zone was found to be of the order of 7δ . A recirculation zone exists on top of the bump that can be divided into two parts. The first, smaller, part stretches from the impingement point of the leading shock at $x \approx 0.25B_l$ up to $x \approx 0.434B_l$. This

part of the recirculation bubble is almost always detached. Downstream of this point, the region of detached flow is made up out of vortices being shed from the stable part of the bubble. This inhomogeneity of the recirculation bubble is not apparent in the mean flow but becomes obvious once instantaneous visualizations are employed. The spectral behavior of the interaction has been quantified using pressure spectra. Low-frequency unsteadiness associated with the movement of the rear and leading shock has been identified at $St = 0.0039$ and $St = 0.0078$. The overall influence of the SBLI on the flow has been quantified via its transfer function, revealing that the shock-interaction acts as a low-pass filter on the flow. The analysis of the transonic shock-wave/boundary-layer interaction through various autocorrelations presented within this chapter shows a possible connection between the dominant structures of the λ -shock system. The shock-motion, upstream boundary-layer bursting, recirculation bubble and the upstream traveling pressure waves are connected by a single frequency which is about 8 times the frequency of the shock motions. This possible self-sustaining loop might generate the movement of the shock formation. The bursting events near the leading shock-wave trigger small scale movements of the shock. Which in turn can trigger the detachment of the recirculation bubble and thus the generation of vortices which can be shown to be connected to the low frequency shock movements through their crosscorrelation. Once the bursts and/or vortices exit the interaction zone and interact with the rear shock and the supersonic tongue, upstream traveling pressure waves are generated. These waves travel around the shock system, enter the supersonic region from above, appearing as traveling upstream due to their inclination. The impingement of these waves on the accelerated boundary-layer and leading shock foot could trigger the emergence of new bursting events. Although the exact nature of the interactions on this path is not apparent, this framework indicates a possible explanation of the frequency-locked oscillations of the λ -shock

Modal Analysis of a Transonic Shock-Wave/Boundary-Layer Interaction

In fluid mechanics, modal decomposition of the flow field is mainly used as a tool to gain insight into the dominant, coherent structures of the flow and the stability properties of its underlying evolution operator. The concept of modal decomposition is best explained using a linear, discrete dynamic system

$$u^{n+1} = F(u^n),$$

with

$$F(u) = Au, \quad u \in \mathcal{R}^m, A \in \mathcal{R}^{m \times m}, \xi^t A \xi > 0 \quad \forall \xi \in \mathcal{R}^m.$$

The operator A can be diagonalized, yielding

$$A = V\Lambda V^{-1}, \tag{6.1}$$

where $\Lambda = \text{diag}(\lambda_i)$ is a matrix made up from the eigenvalues λ_i of A and V is the matrix of eigenvectors v_i of A which are linearly independent and therefore form a basis of \mathbb{R}^m . Any given initial value u_0 can be decomposed as a linear combination of the eigenvectors or *eigenmodes* according to

$$u_0 = a_1 v_1 + a_2 v_2 + \cdots + a_m v_m,$$

where a_i are the amplitudes of the modes in the decomposition of u_0 . The linearity of the operator A dictates that $u^n = A^n u_0$ can be written as

$$\begin{aligned} A^n u_0 &= a_1 A^n v_1 + a_2 A^n v_2 + \dots a_m A^n v_m \\ &= a_1 \lambda_1^n v_1 + a_2 \lambda_2^n v_2 + \dots a_m \lambda_m^n v_m. \end{aligned}$$

The temporal evolution of the dynamic system is completely determined by the evolution of the eigenmodes v_i and their eigenvalues λ_i . Stability of a mode is determined by the modulus of its corresponding eigenvalue. A value of $|\lambda_i| > 1$ leads to an eigenmode that grows exponentially in time, while $|\lambda_i| < 1$ leads to exponential decay. The combination of multiple eigenmodes can cause growth that is not predicted by the eigenvalues. This so-called *non-modal* growth is neglected when performing linear stability analysis.

Modal decomposition works best for linear, finite-dimensional operators. In practice however, the underlying operator will be nonlinear. In addition it might be unknown, infinite dimensional or in the case of operators resulting from numerical discretizations of such dimensions that direct computation of the eigenvalues is not practical or downright impossible. Thus a number of approximate methods for stability analysis and eigenvalue decompositions have been developed. Two different kinds of methods can be distinguished. First, global, linear stability solvers try to approximate the the spectrum of the non-linear Navier-Stokes equations by linearizing the operator around a given baseflow and then employ iterative methods, such as the Arnoldi method described later, to approximate the spectrum of the high-dimensional linear operator. The nonlinearity of the flow is contained within the baseflow while small perturbations around it can be approximated as linear.

The second class of methods emerged due to the enormous dimension of the problem resulting from direct numerical simulations which is based in model order reduction. A small number of discrete snapshots of the flow is analyzed and used to construct an operator that gives a low-dimensional approximation of the flow field. The most popular method is the so-called *proper orthogonal decomposition* (POD) which decomposes the field into modes based on energy content, see Rowley, [87], for an overview. In recent years the so-called *dynamic mode decomposition* as introduced by Schmid and Sesterhenn, [98,100], has gained traction in the numerical and experimental fluid dynamics community. In contrast to the POD, the dynamic mode decomposition disassembles the flow field into temporal structures sharing the same frequency. It therefore identifies coherent structures with the same temporal frequency. As the this thesis is interested in the low-frequency temporal oscillations of a

shock-wave/boundary-layer interaction this type of modal decomposition is a natural fit to the needs of the present work.

Stability analysis has a long history in fluid mechanics and an appropriate overview is out of the scope of this work. However, the review of Theofilis, [113], gives a comprehensive overview of the topic in fluid mechanics. Global stability analysis has been applied to shock-wave/boundary-layer interactions in a comparatively small number of works. The first application of stability considerations to SBLI is due to Crouch et al. in 2007, [17]. The authors studied the transonic flow over an airfoil and found that the buffeting of the airfoil has its roots in the amplification of a low-frequency dominant eigenmode. Although their analysis was carried out in 2D and the baseflow derived with the use of turbulence modeling, their findings could be verified by accompanying experiments. The validity of the two-dimensional ansatz was bolstered by the work of Sandham & Touber in [115]. They conducted a stability analysis of an oblique impinging shock with a separation bubble based on a three-dimensional LES. They found the leading unstable mode, responsible for the separation bubble oscillations, to be two-dimensional. Different results were obtained by Robinet in [85]. Robinet studied laminar SBLI and found a leading three-dimensional mode which could not be directly linked to the low-frequency behavior. Grilli et al., in [31], applied the snapshot based dynamic mode decomposition to SBLI in a compression ramp. Using two-dimensional, spanwise averaged snapshots they were able to detect the dominant low-frequency structures of the flow. A low-order reconstruction of the flow based on the DMD modes recovered the major instability mechanics.

In this chapter, the snapshot based dynamic mode decomposition will be used to extract the dominant low-frequency behavior from the previous simulation of transonic SBLI. Afterwards, methods of global stability analysis will be employed to derive the sensitivity of the low-frequency oscillations. Due to the success of the two-dimensional work of Crouch and Grilli et al., as well as the results of Touber & Sandham, this will be done in two dimensions only.

6.1. Introduction to Dynamic Mode Decomposition

Take a series of temporally equidistant snapshots of the flow field $V^N = \{v_1, \dots, v_N\}$. The *dynamic mode decomposition* assumes a linear mapping A exists that connects the snapshots, $Av_{i-1} = v_i$, and then approximates the

dynamic behavior, eigenmodes and eigenvalues, of this mapping. Using A , the snapshot basis can be expressed as a Krylov sequence:

$$V_1^N = \{v_1, Av_1, A^2v_1, \dots, A^{N-1}v_1\}. \quad (6.2)$$

A further assumption is that given a sufficient number of snapshots the vectors in V_1^N become approximately linear dependent. Thus the last vector, v_N , can be expressed as a combination of the first $N - 1$:

$$v_N = a_1v_1 + a_2v_2 + \dots + a_{N-1}v_{N-1} + r \quad (6.3)$$

$$\iff V^N = V_1^{N-1}a + r, \quad (6.4)$$

where $a = (a_1, \dots, a_{N-1})^T$ and r is the vector of residuals. Defining $e_{N-1} \in \mathbb{R}^{N-1}$ as the unit vector and

$$V_1^{N-1} = \{v_1, v_3, \dots, v_{n-1}\}, \quad (6.5)$$

$$V_2^N = \{v_2, v_3, \dots, v_N\}, \quad (6.6)$$

one can write

$$AV_1^{N-1} = V_2^N = V_1^{N-1}S + re_{N-1}^T. \quad (6.7)$$

Here, the matrix S is of companion type,

$$S = \begin{pmatrix} 0 & & & a_1 \\ 1 & 0 & & a_2 \\ & \ddots & \ddots & \vdots \\ & & 1 & 0 \\ & & & 1 & a_{N-2} \\ & & & & 1 & a_{N-1} \end{pmatrix}. \quad (6.8)$$

It can be shown that its eigenvalues and eigenvectors approximate the eigenvalues of A once the eigenvectors are projected back onto the space spanned by the snapshots. The vector of unknowns a , and thus S , is determined by minimizing the residual r in a least square sense. This is equivalent to expressing the last snapshot v_n optimally as a linear combination of the first $n - 1$ snapshots. The solution of the minimization problem

$$S = \arg \min_S \|V_2^N - V_1^{N-1}S\| \quad (6.9)$$

is given via the QR decomposition of V_1^{N-1} . All in all, the application of the dynamic mode decomposition to a snapshot sequence V^N is given in procedure

Procedure 6.1: Dynamic Mode Decomposition of a Snapshot Sequence V^N

1. Split the snapshot sequence according to

$$V_1^{N-1} = \{v_1, \dots, v_{N-1}\} \quad (6.10)$$

$$V_2^N = \{v_2, \dots, v_N\} \quad (6.11)$$

2. Compute the QR decomposition of V_1^{N-1} :

$$V_1^{N-1} = QR \quad (6.12)$$

3. Compute the best linear mapping of V_N onto itself as

$$S = R^{-1}Q^H V_2^N \quad (6.13)$$

4. Compute the eigenvalues λ_i and eigenvectors ϕ_i of S .
5. Project the eigenvectors ϕ_i of S back unto the full-dimensional space according to

$$\Phi_i = V_1^{N-1} \phi_i \quad (6.14)$$

6.1. Algorithms, equivalent to procedure 6.1, that compute the *empirical Ritz values* λ_i and *vectors* Φ_i exist as described e.g. in [88] or [98], using the singular value decomposition (SVD) of the snapshot sequence to arrive at a numerically more stable algorithm. For all cases described within this thesis no discernible differences between different implementations were observed. The eigenvectors Φ_i are only determined up to a scalar factor, however, as e.g. Rowley et al. show in [88], there exists a unique, physical, scaling of Φ_i , such that

$$v_k = \sum_{j=1}^{N-1} \lambda_j^{k-1} \Phi_j, \quad k = 1, \dots, N-1. \quad (6.15)$$

In addition, it is easy to switch between the discrete time representation of the snapshot sequence and a continuous time representation via

$$v_k = \sum_{j=1}^{N-1} \lambda_j^{k-1} \Phi_j = \sum_{j=1}^{N-1} e^{(\sigma_j + i\omega_j)t_k} \Phi_j, \quad (6.16)$$

where Δt is the timestep between two neighboring snapshots, $t_k = (k-1)\Delta t$, and

$$\sigma_j = \frac{\log(|\lambda_j|)}{\Delta t}, \quad \omega_j = \frac{\arg(\lambda_j)}{\Delta t}. \quad (6.17)$$

The transformation of λ to continuous time will be denoted as $\tilde{\lambda}_j = \sigma_j + i\omega_j$. In summary, the dynamic mode decomposition approximates the eigenvalues of the best linear mapping of a given snapshot sequence V^N onto itself. While this mapping is linear, Rowley et al, [88], show that these eigenvalues and eigenvectors are approximations to the *Koopman* modes and eigenvalues. Eigenvalues and eigenvectors of the nonlinear *Koopmanoperator* that contains the nonlinear behavior of the original dynamical system. Therefore this linear analysis is suitable to describe the nonlinear SBLI. In [88], Rowley et al. also liken the decomposition to a Fourier analysis in time which is the key to the DMDs ability to identify coherent spatial structures tied to a single temporal frequency. In [14] this relationship is clarified further, Chen et al. show that the *mean subtracted* dynamic mode decomposition is equivalent to a harmonic averaged temporal discrete Fourier transform of the system. It can be shown that the eigenvalues of the reduced mapping are then predetermined by the number of snapshots used as the n complex roots of unity excluding 1 itself. This means that all modes are marginally stable and the algorithm can no longer detect growing or decaying modes. While the conventional DMD is able to detect modes with arbitrarily low frequency - the highest frequency is still restricted by the sampling rate - the fixation of the eigenvalues in the *mean subtracted* DMD means that the algorithm can only detect frequencies that have at least one full oscillation within the snapshot window.

In modal decomposition, it is often the goal to select a small number of modes which best describe the underlying flow. It is *a priori* not clear how to order the modes obtained from the dynamic mode decomposition for such a purpose. In other types of modal decompositions, like POD, the choice of dominant modes is clear because the modes are constructed based on e.g. energy level. Also due to the orthogonality of the modes, increasing their

number reduces the projection error,

$$\epsilon = \frac{\|x - P_v x\|}{\|x\|}, \quad (6.18)$$

where P_v is the projection of x onto the subspace spanned by a given set of modes and back onto the original space. In DMD, due to the non-orthogonality of the modes, this is not the case. The most used criterion to construct a mode ranking is the modal amplitude $\|\Phi_i\|^2$. This ranking by energy neglects the temporal evolution of the modes and is therefore not always the best choice. For example, a high amplitude mode with a corresponding eigenvalue $|\lambda_i| \ll 1$ might be ranked high although the strong temporal damping means that the mode only contributes to the flow for a very short time. Therefore, Tissot et al., see [114], propose the following temporally weighted energy norm for use in DMD reconstruction:

$$E_j = \frac{1}{T} \int_0^T \|\Phi_j \lambda_j^{t/\Delta t}\|^2 dt = \|\Phi_j\|^2 \frac{\exp(2\sigma_j T) - 1}{2\sigma_j T}. \quad (6.19)$$

In the case where all eigenvalues are marginally stable with $|\lambda_j| \approx 1$, $\forall j$ this norm does not differ from the simple amplitude computed without temporal weighting.

6.2. Dynamic Mode Decomposition of a Transonic SBLI

This section details the results of the dynamic mode decomposition applied to the previously described DNS of a transonic shock-wave/boundary-layer over a bump-shaped obstacle. The decomposition will be used to identify the dominant modes and structures of the flow. Reconstruction of the flow using the dominant modes is done to investigate the structural behavior of the interaction.

For the dynamic mode decomposition 768 snapshots of the instantaneous flow field are taken. They cover a timespan of $3T$, where T is the period of lowest frequency oscillations and allow the resolution of Strouhal numbers up to $St = 0.7$. Looking at the PSD of pressure in fig. 5.18 this window of Strouhal numbers is sufficient to resolve the low frequency shock oscillations. However, the high-frequency turbulent oscillations are underresolved.

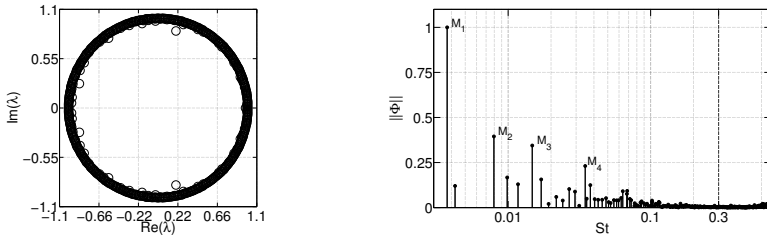


Figure 6.1.: Spectrum (left) and modal amplitude (right) distribution of the dynamic mode decomposition based on spanwise averaged snapshots of the transonic shock-wave/boundary-layer simulation.

Results from Grilli et al. [31], and further studies by the author show, that the enrichment of the DMD snapshots to resolve higher frequencies does not change the behavior of the low-frequency modes. This is expected, as the study of pressure and velocity spectra, see chapter 5, revealed no significant correlation between the low frequency shock dynamics and the turbulent flow structures with Strouhal number $St = \mathcal{O}(1)$. It must be noted, that the spanwise averaging of snapshots does change the shape of the modes containing structures that change rapidly in the spanwise direction. To confirm that the averaging does not change the form of the modes and the spectrum an additional decomposition using a sequence of instantaneous snapshots in the xy -plane was performed. It was confirmed, via an ancillary decomposition of a single wall-normal plane, that the only modes influenced by the averaging are those that contain spanwise intermittent structures. These include small-scale turbulence as well as local modulations of the shock positions that are small in amplitude and about one order of magnitude higher in frequency when compared to the base movement of the shock. After describing underlying structural features of the decomposed system, both decompositions will be used to visualize the difference between averaged and local flow field and dynamics.

6.2.1. Spectra

After simulating the shock-wave/boundary-layer interaction for multiple cycles it is save to assume that the interaction is described as a periodic oscillation around a mean state. This behavior is supported by the spectrum of the dynamic mode decomposition of the spanwise averaged and instantaneous

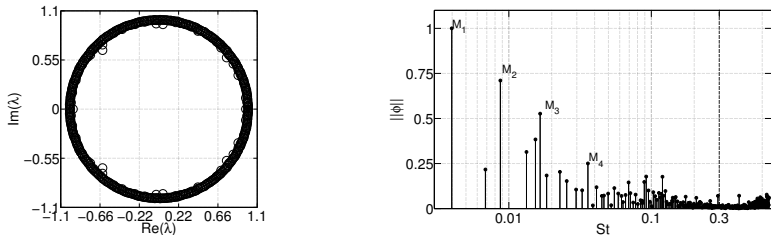


Figure 6.2.: Spectrum (left) and modal amplitude (right) distribution of the dynamic mode decomposition based on instantaneous snapshots of the transonic shock-wave/boundary-layer simulation.

flow field, see fig. 6.1 and 6.2 respectively. As is required for a periodic system, almost all eigenvalues are neutrally stable and lie on the unit circle. The temporally-weighted amplitude of the DMD modes is displayed over Strouhal number in the same figures. Since almost all eigenvalues are neutrally stable, the temporal weighting has little effect on the shape of the graph. The weighting has its main effect on a few modes describing turbulence that are marginally resolved by the sampling rate. As observed in [88], the magnitude of the modes corresponds very well to the spectral behavior of the actual field.

The general shape of the spanwise-averaged and the instantaneous decomposition agree. Therefore the following discussion is based upon the spanwise-averaged spectrum and its amplitude distribution in figure 6.1. Differences compared to the instantaneous decomposition will be covered subsequently. The most dominant mode is located at $St \approx 0.0039$ which corresponds to the lowest frequency of the shock system found in the statistical analysis in chapter 5 with only a very small difference in frequency. The four most dominant modes cover all frequency ranges identified as connected with the movement of the shock system. They contain the peak frequencies of the front and rear shock movement at $St = 0.0039$ and $St = 0.0078$, as well as the frequency associated with bursting within the boundary-layer and the shedding of the recirculation zone at $St \approx 0.032$. The first 4 modes form a phase locked system with their frequencies being 2, 4 and 8 times the main shock frequency with only a small margin of error. These modes will be referred to as M_1 , M_2 , M_3 and M_4 in order of decreasing amplitude and increasing frequency. In the regime of the actual vortex shedding, no single mode stands out as the energy is distributed over a wide range of Strouhal numbers in the wake. It is noteworthy that the energy of the low-frequency oscillations is about

2.5 times larger compared to the other modes. Comparing this to the amplitude distribution of the instantaneous flow field there are only minor changes. The Strouhal numbers of the dominant modes M_1 to M_2 change by a small amount, $\Delta St < 5\%$, but the relation between the frequencies stays the same. Two important differences remain however. In the instantaneous case, two modes emerge in the vicinity of M_3 whose amplitude is higher than that of M_4 . These modes belong to coherent structures with a high spanwise frequency. When averaging the field in the spanwise direction their contribution to the field is lost. In addition the amplitude of modes M_2 and M_3 is up to two times larger when compared to their spanwise-averaged analogues. This effect can again be explained through spanwise modulation and the averaging process. When the amplitude of an oscillating structure has a spanwise modulation the local and averaged amplitude of those structures, in this case modes M_2 and M_3 , can differ. This also indicates that modes M_1 and M_4 correspond to spatial structures without large spanwise modulation. The analysis of various autocorrelations in the previous chapter placed the bursting frequency at the lower value of $St \approx 0.029$ compared to $St = 0.032$ found in the DMD. Despite this mismatch, it can be assumed that both frequencies are related to the same physical phenomenon. First, both frequencies are derived in different fashions. While the construction of the power spectral density of the various quantities in figures 5.17 and 5.24 restricts the realizable Strouhal numbers, the DMD algorithm can extract arbitrary frequencies. Therefore, it should not come as a surprise that DMD and FFT provide slightly differing frequencies. As discussed before, the spilling of the recirculation bubble, associated with the frequency in question, is highly varied in spanwise direction, see figure 5.8. Therefore, the extracted frequency might be dependent on the specific spanwise slice used for the analysis. Lastly, the fact that the Modes M_1 to M_4 present a phase-locked system lends confidence to the frequencies derived by the DMD.

6.2.2. Classification of Modes

The decomposition of the flow field in coherent spatial structures can be used to gain a better understanding of inherent dynamics and structures that make up the flow field in the transonic shock-wave/boundary-layer interaction. Therefore, the pressure fields of the 4 dominant modes are shown in fig. 6.3, note that all modes are arbitrarily scaled as to just show their spatial structure. Mode M_1 has the typical λ -shape associated with shock-wave/boundary-layer interactions and resembles the shock positions observed

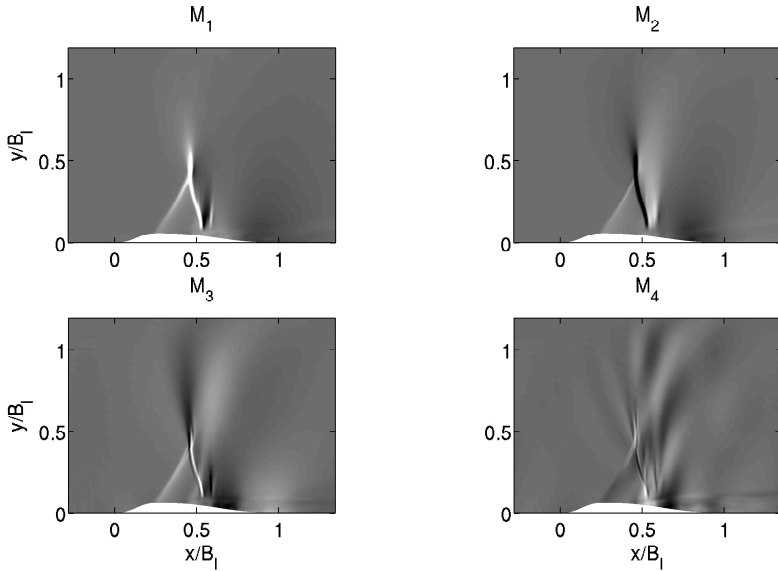


Figure 6.3.: Contour plots of the real normalized pressure field for modes M_1 - M_4 . Arbitrary colorscale used for best visibility.

within the flow. The movement of both shock feet seems to be roughly in phase. The next dominant mode M_2 has the same general shape, but a distinct phase shift between leading and terminating shock is visible. The mode M_3 is the first where a new structure is introduced. While its influence on the shock system is in a narrower spatial region, it is the first mode to have a distinct structure in the wake behind the bump which is of comparable amplitude to the λ -part of the mode. The mode M_4 looks markedly different. Its frequency of $St \approx 0.032$ was found connecting different phenomena within the interaction zone. It marks the frequency of bursting events in the incoming boundary-layer at the top of the bump. The frequency of attachment at the separation point between the stable and intermittent part of the recirculation bubble was found to be in this regime. In addition, the dominant frequency of the upstream traveling waves, visible in 5.26, also fell within this Strouhal number range. The representation of M_4 in figure 6.3 reflects these connections. Contrary to the lower frequency modes, it shows modulation within the recirculation zone, specifically at the end of the sta-

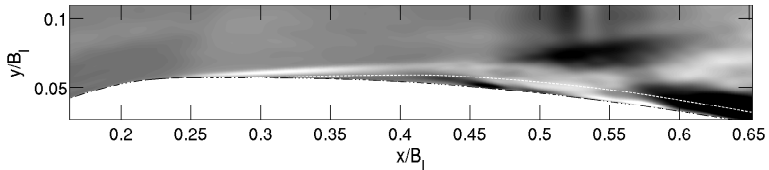


Figure 6.4.: Streamwise velocity field of mode M_4 . The mean recirculation zone is marked by the dotted line. Arbitrary colorscale used for best visibility.

ble regime of the recirculation bubble. While the mode itself has structure within the shock, it is of smaller scale and amplitude when compared to the other modes. However, the shape of the pressure field clearly shows the waves traveling counterclockwise around the shock system.

Figure 6.4 focuses on the shape of mode M_4 in the vicinity of the recirculation bubble. Streamwise velocity is shown. As the DMD naturally decomposes the field into a steady mean state and fluctuations around said state, the velocity modes correspond to velocity fluctuations. The shape of the mode reveals distinct information about the structure of the recirculation zone. The mean recirculation zone extends far downstream, extending from $x = 0.25B_l$ up until the end of the bump. The shape of the mode reveals the separation of the bubble into two distinct parts. Up until $x \approx 0.43B_l$, the mode represents a steady breathing motion of the bubble. Beginning at that point, the steady, wall parallel structure of the mode changes towards intermittent vortex structures. The location $x \approx 0.43B_l$ marks the end of the always detached part of the recirculation bubble, as found in the previous chapter 5, there the bubble periodically bursts open and vortices are generated. In addition, upstream of the separation point, at the leading edge of the bump, an oscillating structure can be seen in the velocity fluctuations that could correspond to the bursting events detected in this region.

As can be seen in the power spectral density of pressure fluctuations, see fig. 5.17, no clear peak is visible in the wake where the vortices are shed. The amplitude distribution in figures 6.1 and 6.2 reflects this. No clear dominant mode in the $St \approx 0.1$ regime emerges. Rather, energy is distributed over a broad span of modes. Figure 6.5 shows two typical representative of these modes. The vortices in the wake are clearly visible. In addition, upstream traveling waves of shorter wavelength seem to emanate from the shed vortices. These waves show a direction of propagation that adheres to the shape of the

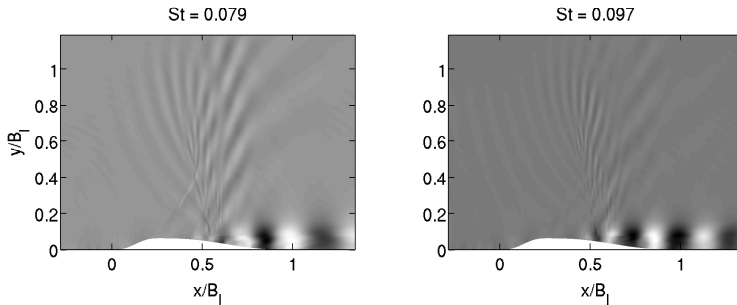


Figure 6.5.: Contour plots of the normalized pressure field for two different modes associated with the vortex shedding behind the bump. Arbitrary colorscale used for best visibility.

terminating shock-wave, traveling away from the wall before curving counter-clockwise around the λ -shock. Note also the streamwise position where the vortex structures form. Their point of origin lies at $x \approx 0.54B_l$, the vortices interact with the supersonic tongue and its terminating shocklet.

Another way to classify and distinguish the different modes is by their contribution to the pressure signal at the wall. Pirozzoli et. al. propose the use of the wall pressure energy $|p_w|^2$ of each mode as a measurement of their contribution to the pressure signal at a specific streamwise location, see [71]. Figure 6.6 depicts $|p_w|^2$ normalized by its mean value in the upstream turbulent boundary-layer for three distinct modes: one representant of the low-frequency shock modes, M_1 , the burst and recirculation mode M_4 and a typical high frequency mode with Strouhal number $St = 0.61$. The pressure amplitude of M_1 has a distinct peak where its strength is up to 2 orders of magnitude larger compared to its upstream values. The peak at $x \approx 0.255B_l$ corresponds to the location where the leading shock impinges on the wall. The strength decreases throughout the rest of the interaction zone below the λ -shock. Following the end of the stable recirculation zone, the energy reaches a plateau that extends through the whole domain. Showing that the shock oscillations have influence that is felt far downstream of the shock system itself. The pressure amplitude of mode M_4 has a steady plateau within the stable part of the recirculation zone, the detachment point at $x = 0.43B_l$ is visible as significant peak in pressure amplitude. In addition, energy is

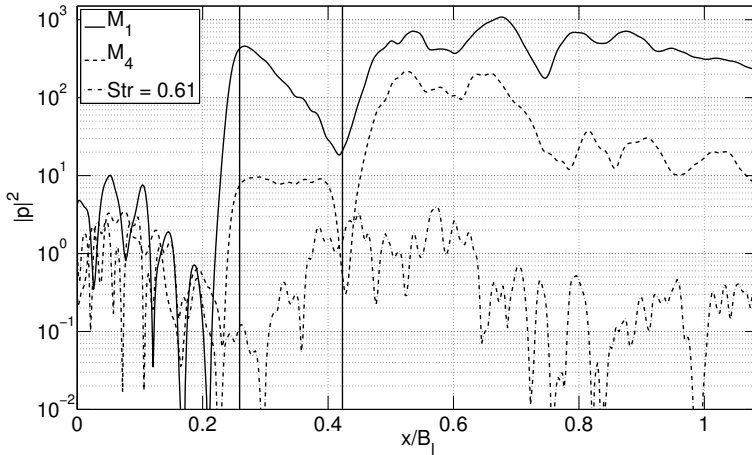


Figure 6.6.: Wall pressure energy $|p_w|^2$ of different modes throughout the interaction zone. The horizontal lines denote the location of the bump throat and the end of the stable recirculation zone.

high within the wake. Figure 6.6 suggests that mode M_1 does not contribute to the formation of a stable recirculation bubble on the bump. As stated in chapter 4, the separated flow cannot sustain strong pressure gradients and the wall-pressure pressure profile of mode M_1 displays such gradient in the region of the recirculation bubble. This plateau is found in mode M_4 , mirroring the structure visible in the velocity fluctuations in fig. 6.4.

In contrast to the low-frequency modes, the energy of the turbulent mode at $St = 0.61$ descends before reaching the first shock, as is expected due to the acceleration of the flow leading to a reduction of turbulence intensities. It reaches its upstream level within the recirculation bubble but then settles at 1 to 2 orders of magnitude lower in the wake.

All in all, graph 6.6 emphasizes, that the SBLI amplifies the contribution to the wall-pressure spectrum of the lower frequencies while damping the turbulent energy contained in higher frequencies. The results are in good agreement with the transfer function computed in the previous chapter, see 5.22. Thus, the SBLI seems to feed energy from the turbulent, small scale frequency range into the low-frequency unsteadiness of the system. This behavior mirrors suggestions on the nature of the unsteadiness made by Pirozzoli et al.

i	M_1	M_2	M_3	M_4
$E_r(i)$	0.9476	0.31	0.24	0.12

Table 6.1.: Error norm $E_r(i)$ of subsequent DMD reconstructions of the transonic SBLI.

and Sandham et al. in [71, 116]. Their suggestion, going back to Plotkin, [78] is, that the energy needed to sustain the low-frequency oscillations is provided by the high-frequency structures being fed into the SBLI.

6.2.3. Reconstruction of the Flow

After describing the different types of modes resulting from the dynamic mode decomposition of the flow field, this section studies the reconstruction of the flow using the most dominant modes. The reconstruction of the flow is done using the formula

$$u(x, t) = \sum_i e^{\lambda_i t} \Phi_i(x). \quad (6.20)$$

As an indicator for how many modes, in addition to the mode describing the mean field, should be used for the reconstruction, Grilli et al, [31], propose the use of the error norm

$$E_r(i) = \int_0^{2T} \frac{\|S^{i+1}(t) - S^i(t)\|}{\|S^i(t) - S^1(t)\|} dt. \quad (6.21)$$

Here, i is the number of modes considered for the reconstruction while S^i is the reconstruction using i modes. The value of E_r is a weighted residual of the reconstruction. It can be interpreted a measure of the additional information introduced by considering the $(i + 1)$ -th mode. The order by which modes are added to the reconstruction is based on their magnitude as displayed in fig. 6.1. Thus the reconstruction starts with the mean mode, following which the low-frequency modes M_1 and M_2 responsible for the shock oscillations are added.

The residual decreases very quickly, see 6.1, confirming the mode ranking based on weighted amplitude as a fitting choice. After adding mode M_4 to the reconstruction, the residual is down to 12%. Considering the trade-off

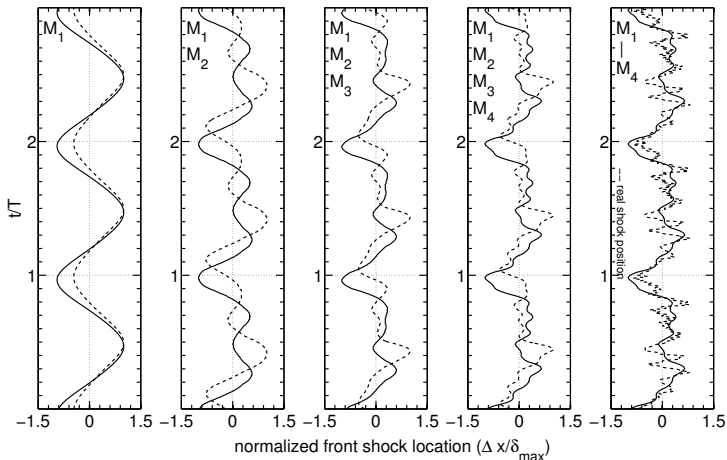


Figure 6.7.: Reconstruction of the leading shock position at $y = 0.1B_l$ done using modes M_1 - M_4 added to the base flow. Solid line: reconstruction using spanwise averaged snapshots; dotted line: reconstruction using instantaneous snapshots.

between a lower residual and a small number of modes used for the reconstruction, the four most dominant dynamical modes are used for the reconstruction of the field from now on.

Shock Movement The key feature of the flow configuration studied here is the low-frequency movement of both shock-feet. In figures 6.7 and 6.8 the shock positions are depicted as derived from the reconstruction with a varying number of modes. The shock position is obtained from the position of the largest pressure and density gradients of the reconstructed flow at a wall-normal position of $y = 0.1B_l$. This is done to obtain a sharper picture of the shock position, as the pressure and density gradients smooth out close the wall. However, the extend of the shock motion varies with distance from the wall. Therefore the maximum range of the shock motion differs from the range reported beforehand in section 5.

In figure 6.7 the location of the leading shock over a timespan of $3T$ is displayed for a reconstruction with up to four modes, (M_1, M_2, M_3, M_4), in addition to the base flow. Reconstructions are shown using spanwise-

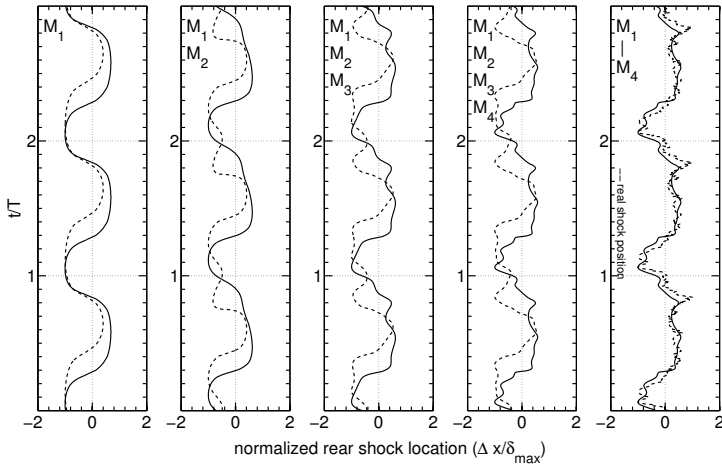


Figure 6.8.: Reconstruction of the rear shock position at $y = 0.1B_l$ done using modes M_1 - M_4 added to the base flow. Solid line: reconstruction using spanwise averaged snapshots; dotted line: reconstruction using instantaneous snapshots.

averaged decomposition (solid line) and the instantaneous decomposition (dotted line). The shock displacement is computed in relation to the mean, spanwise-averaged shock location. The reconstruction using only mode M_1 shows a sinusoidal movement where the backwards movement of the shock is slightly faster than the forward movement. There is a very light phase delay between the instantaneous and averaged shock position. When adding mode M_2 the difference between the forward and backward movement of the shock becomes more pronounced. The backward phase of the shock motion has two distinct maxima. As expected from the amplitude distribution of the modes in figure 6.2, the range of shock motion is larger in the instantaneous case. In addition the phase shift between both reconstructions has grown. The reconstruction using three modes presents a comprehensive view of the shock motion. The cycle is started with a rapid backwards movement of the shock up to its furthest downstream position. It then moves forward up to the mean position before remaining stationary for a time and finally rapidly moving upstream and starting the cycle again. It is noteworthy that the shock spends almost two thirds of a cycle downstream of its mean position. Mode M_4 adds

small amplitude oscillations to the shock position but does not influence the overall behavior of the flow. The bursting events thus do not directly govern the low-frequency/large-amplitude modulations of the system but introduce small perturbations to the position of the front shock.

The rear shock motion, as seen in figure 6.8, follows a very similar pattern. The first reconstruction, using just mode M_1 again depicts a sinusoidal motion. Compared with figure 6.7, a phase shift between front and rear shock is observed. The phase shift between both reconstructions is more pronounced in the rear shock motion when compared to the front shock motion. Adding more modes to the reconstruction emphasizes the general behavior. Looking at the spanwise-averaged reconstruction the addition of more modes leads to a sharp downstream movement of the shock followed by very slow upstream movement that is terminated with a sudden upstream displacement. Once all four modes are used, the emergence of two distinct downstream peaks, although not as pronounced as in the front shock movement, can be observed. For the instantaneous reconstruction the first upstream motion of the shock after reaching its downstream peak has a higher amplitude, as predicted by the modal amplitude distribution in fig. 6.2. Concluding, the motion of both front and rear shock can be characterized by a sudden downstream displacement followed by a slower upstream movement. This large scale-motion is superimposed with low-amplitude modulations introduced by mode M_4 which is connected to the upstream bursting events.

It is interesting to note that the mean position of the shock in the different reconstructions do not match when just mode M_1 is considered. The difference is reduced when more modes are added. Despite this it could still be an indication that the overall timespan of the simulation is too short as the mean value of all fluctuations around the mean state must be zero in the long run.

Recirculation Bubble Dynamics In figure 6.9 the temporal evolution of the mass within the recirculation bubble is plotted as predicted by the reconstruction with up to four modes. The mass of is computed by considering the fluid in regions with negative streamwise velocity. The graphs in fig 6.9 show the relative deviation from the mean, spanwise-averaged, recirculated mass over time. Again, both the instantaneous (dotted line) and the spanwise averaged (solid line) reconstructions are contrasted against each other. The reconstruction using just mode M_1 shows two things. First of all, upstream movement of the leading shock and the filling of the recirculation bubble happen simultaneously. This is expected, as the bubble originates right at the

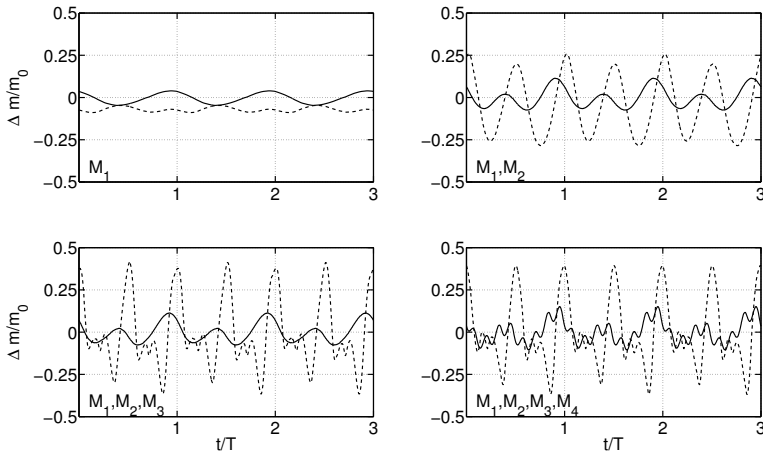


Figure 6.9.: Reconstruction of the recirculating mass computed from modes M_1 - M_4 added to the base flow.

impingement point of the leading shock on the wall. Therefore a upstream movement of the shock also enlarges the area in which the bubble can form or vice versa. However, the influence of the low-frequency modes is almost negligible with the displaced mass only making up around 5% of the mean bubble mass. This is even more clear in the instantaneous reconstruction where the mass contained within mode M_1 is lower than the mean mass at all times. Considering the wall pressure induced by M_1 , as seen in figure 6.6, this is not surprising. The wall pressure does not show a plateau region that would be necessary to sustain a region of separated flow. Adding mode M_2 introduces much larger fluctuations to the bubble size. The comparison of instantaneous and averaged reconstruction shows a much higher amplitude in the instantaneous reconstruction bubble oscillations. During the previous excursion on the recirculation bubble dynamics in section 5.2.3 it was shown, that only a very small *stable* part of the recirculation zone is always detached, while the largest part is made up out of intermittently detached vortices with a small spanwise lengthscale. Therefore instantaneous modulations of bubble size must be larger than their spanwise averaged counterparts. Using the remaining modes the general behavior of the bubble emerges. The bubble mass modulations remain based on the main frequency of mode M_2

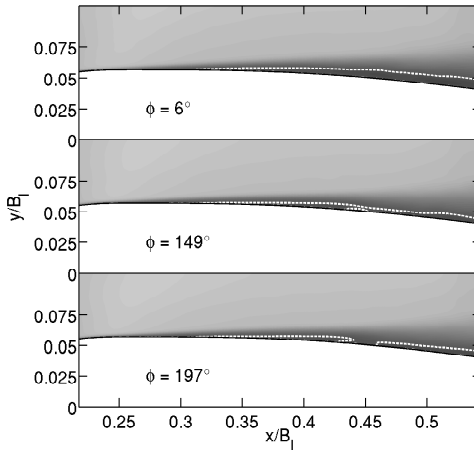


Figure 6.10.: Reconstruction of the recirculation bubble using modes M_1 - M_4 obtained from instantaneous snapshots. Contours of streamwise velocity are displayed. The recirculation zone is marked by the dotted line. Reconstruction plotted at different phase angles of mode M_4 .

which indicates that there is no direct connection between the low-frequency shock-movement, mode M_1 , and the recirculation bubble. For the spanwise averaged case, the higher frequency case modulations only introduce small amplitude modulations that do not change the overall behavior. In the instantaneous case, the bubble fills up much faster than it is emptied. The overall behavior of the recirculation bubble obtained from the instantaneous reconstruction matches the behavior observed by Grilli et. al. , see [30, 31], in supersonic SBLI on a compression ramp, although on a faster timescale. Whereas in the compression ramp case the filling and emptying of the bubble was directly related to the low frequency shock motions - this is not the case here. This apparent disconnect of the bubble dynamics and the lowest frequency oscillations is noteworthy. In the compression ramp case, where the bubble is trapped between the shock and the ramp, the bubbles direct influence on the shock system is much higher. Still the general behavior of the bubble is similar in both cases.

The addition of mode M_4 to the reconstruction has very little influence on the overall mass of the recirculation bubble. However, the visualization of the

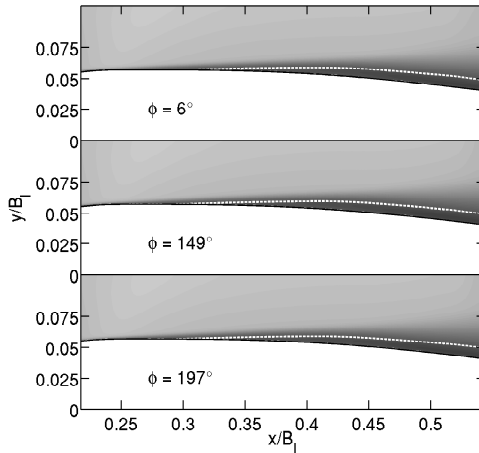


Figure 6.11.: Reconstruction of the recirculation bubble using modes M_1 - M_4 obtained from spanwise averaged snapshots. Contours of streamwise velocity are displayed. The recirculation zone is marked by the dotted line. Reconstruction plotted at different phase angles of mode M_4 .

reconstructed velocity field in figure 6.10 and 6.11 highlights the influence of that mode. In fig. 6.10, the reconstruction using modes M_1 to M_4 obtained from the instantaneous snapshots is depicted at different phase angles of mode M_4 . With increasing angle, the recirculation bubble grows slowly before it suddenly rips apart at $x = 0.423$. Thus marking the shedding of vortices from the stable part of the recirculation bubble. As a contrast figure 6.11 shows the flow field at the same phase angles when reconstructed from spanwise averaged snapshots. No bursting is observable. The reconstruction only shows a steady breathing of the bubble, obscuring the highly intermittent behavior of the instantaneous flow in this region. The same is true for all reconstruction using the instantaneous snapshots but missing mode M_4 . Comparing figures 6.7 and 6.9 a common theme emerges with the addition of M_4 to the reconstruction. The bursting frequency does not effect the overall behavior of the system but introduces small scale fluctuations. Small-scale shock movements could trigger small-scale fluctuations in the bubble dynamics which ultimately lead to the detachment of vortices from the separated flow, as seen in 6.10.

6.2.4. Conclusions

The dynamic mode decomposition of the transonic SBLI revealed a system governed by four phase-locked modes which cover timescales from the lowest shock oscillations at $St = 0.0039$ to the bursting frequency found in the previous statistical analysis connecting the different phenomena in the interaction zone. Reconstructions based on instantaneous and spanwise averaged snapshots revealed insight into the dynamics of shock movement and recirculation bubble filling and spilling. Investigation of wall-pressure energy of the dynamic modes emphasizes that the shock-system acts as a low-pass filter and amplifies low frequencies while damping the high ones. Shock-movement is governed by the low-frequency mode M_1 . The dynamics of the recirculation bubble on the other hand are dominated by the higher frequency of mode M_2 . This disconnect is supported by the wall pressure energy of the modes. The wall pressure induced by shock-mode M_1 features a gradient which would not support the recirculation zone. Comparing these results to the supersonic compression ramp case of Grilli et al., [31], is interesting. In their case, where the bubble is fixed between the compression corner and the leading shock, bubble movement and shock-oscillations coincide. This begs the question if an indirect mechanism exists within the transonic SBLI that connects recirculation bubble and rear shock movements. The mode M_4 could conceivably be part of a feedback mechanism responsible for this coupling. Remotely related to the results of Pirozzoli and Grasso, [77], who found an acoustic feedback-loop within the separation zone in supersonic SBLI, the mode triggers acoustics that travel upstream and interact with the leading shock and recirculation bubble.

The bursting mode M_4 appears in both the shock reconstruction and the bubble dynamics as a source of low-amplitude oscillations. These oscillations can be linked to the rupture of the recirculation bubble at $x \approx 0.0434B_l$ and the subsequent generation of vortices in the interaction zone. These vortices emit upstream traveling waves which in turn could lead to bursting events on the upstream side of the bump. The results of this section strengthen the results proposed through the use of regular statistical analysis in chapter 5.

It can be concluded that the reconstruction using only spanwise averaged snapshots captures the main features of the shock system very well. However it is unable to reconstruct the higher frequency oscillations and intermittent flow structures within the recirculation bubble that are believed to be connected to the movement of the shocks. It is therefore advised to not solely rely on spanwise averaged snapshots when the flow field contains features

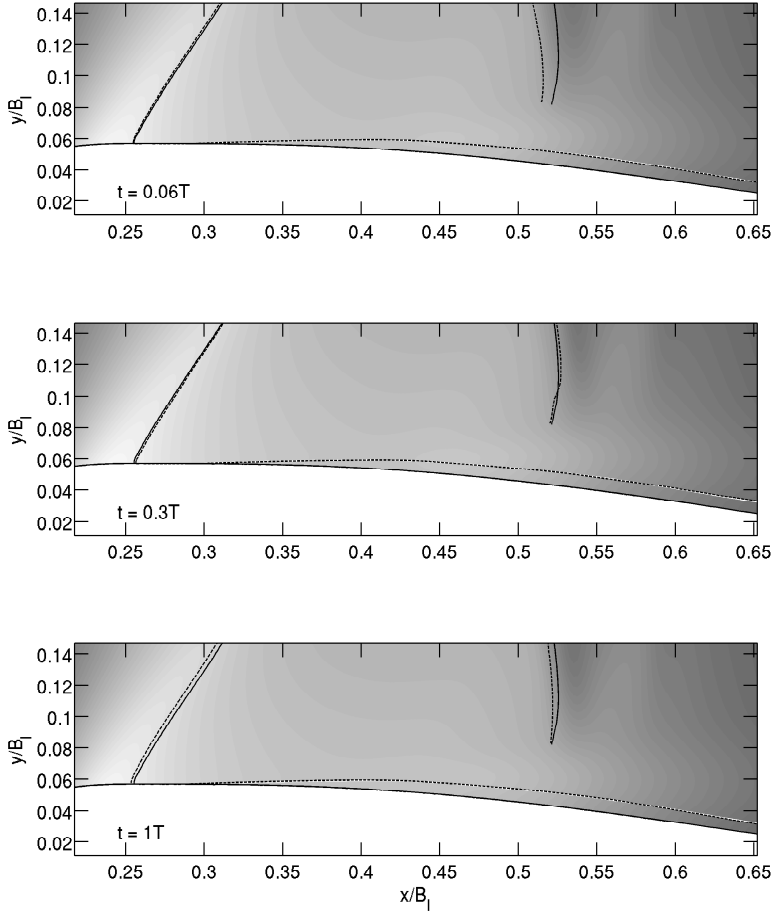


Figure 6.12.: Pressure field of the dynamic mode reconstruction using modes M_1 - M_4 obtained from spanwise averaged snapshots plotted at different times within one oscillation period T . Dotted lines mark the instantaneous shock positions and recirculation bubble extend; solid lines their mean values.

with smaller spanwise lengthscale or high spanwise modulation.

6.3. Theory of Sensitivity Analysis

The results of the previous section have shown that modal decomposition is suitable for the use in SBLI analysis. The snapshot based approach of the dynamic mode decomposition lends itself beautifully for the phenomenologic description of the SBLI and an analysis of the dominant structures within the flow. Being snapshot based, the DMD is an computationally inexpensive way to extract approximate modal and stability information from a dynamic flow field in lieu of more expensive and complicated methods. However, a decomposition of the actual Navier-Stokes operator can be used to not only extract eigenmodes and eigenvectors of the specific flow, but also to gain information on how to influence the flow with specific goals in mind. This *sensitivity analysis* is based on linear stability analysis of the Navier-Stokes equations and their adjoint formulation. The following section is organized as follows. The basic principle of linear stability theory will be explained. The adjoint Navier-Stokes equations and their relation to sensitivity analysis will be introduced. Afterwards, a brief overview of the matrix-free Arnoldi algorithm used to compute the eigenvalues and eigenvectors is given. This is done with the sole aim to find an ansatz as to how the low-frequency shock oscillations of the SBLI system might be damped or otherwise influenced. Although this derivation of sensitivity of the shock oscillations is not dependent on knowledge of the physics of the system, the results may yet be used to gain an understanding of the underlying system in a way that is similar to reverse-engineering. The insight how to influence the oscillations can be used to find the cause of the oscillations in the first place.

The linear stability analysis, which forms the basis of all things discussed here, is dependent on the assumption that all nonlinearities are contained within the baseflow around which the equations are linearized. The stationary mean field is the baseflow of choice for the analysis carried out here. The results of the analysis therefore depend critically on the mean flow. This might present a problem for highly turbulent flows. The mean state is never realized within the flow and is therefore not physical in a sense. Therefore, the results of stability analysis for turbulent flows should always very critically examined. A formally correct approach to the stability analysis would have to be based on the so-called Reynold's triple decomposition, see [83]. This approach takes the nonstationarity of the oscillating flow into account.

However, both approaches should yield the same eigenmodes, only with slight differences in damping rate. In addition, it must be pointed out, that this section will contain some simplifications of and assumptions on both the underlying flow and mathematical theory that could lead to a corruption of the results. This study is therefore not meant as a definite answer to the problem of sensitivity analysis in SBLI. Rather it will be argued that this rough analysis presents a good starting point for further, more sophisticated studies, in this direction and that sensitivity analysis can present a valuable tool in further understanding the complex interactions in transonic SBLI. The results obtained here aim to present a valid starting point when designing methods to control the low-frequency unsteadiness in SBLI.

6.3.1. Linear Stability Analysis

In general terms, linear stability theory is the study of a systems response to infinitesimal perturbations. If such perturbations are damped or do not grow without bounds in space and time, the flow is called stable, while perturbations that grow without bounds are the definition of an unstable flow. The decomposition of the flow used for the stability analysis is

$$q(x, y, z, t) = \bar{q}(x, y, z, t) + \epsilon q'(x, y, z, t), \quad (6.22)$$

where $\bar{q}(x, y, z, t)$ denotes the time-dependent base flow and $q'(x, y, z, t)$ the infinitesimal perturbations. This most general decomposition can be simplified by assuming a steady base flow $\bar{q} = \bar{q}(x, y, z)$. Remembering the results of the dynamic mode decomposition, this assumption is supported. The DMD decomposition of SBLI system revealed a steady base flow with superimposed periodic oscillations. The temporal behavior of the perturbations can then be captured in the parameter λ which appears as an eigenvalue in the linearized governing equations:

$$\lambda q' = LNS(\bar{q})q', \quad (6.23)$$

where $LNS(\bar{q})$ are the linearized Navier-Stokes equations linearized around \bar{q} . Thus leading to the decomposition of the flow as:

$$q(x, y, z, t) = \bar{q}(x, y, z) + \epsilon q'(x, y, z)e^{-\lambda t}, \quad (6.24)$$

where the eigenvalue λ governs the temporal growth rate and frequency of the perturbations. The full stability information is therefore given by the

solution to the eigenvalue problem (6.23). The growth rate is given by λ , while the shape of the modal structures is determined by the eigenfunctions q' . The governing eigenvalue equation is written in the familiar linear algebra notation as

$$\lambda x = Ax, \quad \lambda \in \mathbb{C}, \quad x \in \mathbb{C}^n, \quad A \in \mathbb{C}^{n \times n}. \quad (6.25)$$

As before, the eigenvalues of the matrix A have to be computed. The standard technique for this problem is the QR method which demands $\mathcal{O}(n^3)$ operations. The dimension of the of the system matrix in the dynamic mode decomposition was $m \ll n$, implying that this direct method for the eigenvalue computation can no longer be applied. Instead, approximate, iterative methods have to be applied. The most commonly used of such methods is the Arnoldi algorithm, whose most basic form will be described here.

6.3.2. The Arnoldi Method

The Arnoldi method goes back the work of W.E. Arnoldi in 1951, see [3]. Many different variations and modifications of the method exist. The basic methodology will be described and the most commonly used extensions and problems mentioned.

The direct QR method for the computation of eigenvalues works by decomposing the matrix A into upper Hessenberg form via a unitary matrix V through the modified Gram-Schmidt algorithm:

$$AV = VH, \quad H, V \in \mathbb{C}^{n \times n}. \quad (6.26)$$

The matrix H being the upper Hessenberg matrix with only zero entries below the first subdiagonal. Afterwards, QR iterations are used to eliminate the subdiagonal entries of H and write A as

$$AQ = QU, \quad Q, U \in \mathbb{C}^{n \times n}. \quad (6.27)$$

Here Q again is unitary while U is a upper triangular matrix with the eigenvalues of A being $\text{diag}(U)$.

The Arnoldi ansatz is to stop the reduction to Hessenberg form after m iterations, $m \ll n$. The resulting partial reduction takes the form:

$$AV_m = V_m H_m + f_m e_m^T, \quad V_m, H_m \in \mathbb{C}^{m \times m}, \quad f_m \in \mathbb{C}^{n \times 1}. \quad (6.28)$$

Here $V_m = [v_1, \dots, v_m]$ is the m -dimensional orthonormal basis, H_m the upper Hessenberg matrix, $f_m = h_{m+1} v_{m+1}$ is the residual orthogonal to V_m

and finally e_m is the m -th canonical basis vector. The eigenvalues σ_j of H_m , called Ritz-values, are approximations to the real eigenvalues λ_j of A if h_{m+1} is small. The associated eigenvectors \tilde{x}_j of A are called Ritz-vectors and are calculated as

$$\tilde{x}_j = V_m y_j. \quad (6.29)$$

That is, they are the projections of the eigenvalue $y_j \in \mathbb{C}^{m \times 1}$ of H_m onto the full space spanned by V_m . In general, some Ritzpairs are good approximations to real eigenpairs (x_j, λ_j) of A while other pairs do not constitute a reasonable approximation at all. The accuracy is measured by the residual

$$\|A\tilde{x}_j - \sigma_j \tilde{x}_j\| = |\beta_m e_m^T y_j|, \quad (6.30)$$

where $\beta_m = \|f_m\|$. The Arnoldi method, based on the Gram-Schmid decomposition, constructs a orthonormal basis V_m from the Krylov subspace

$$\mathcal{K}_m(A, v_1) = \text{span}\{v_1, Av_1, A^2v_1, \dots, A^{m-1}v_1\}. \quad (6.31)$$

Afterwards the basis V_m is used to perform the partial reduction to Hessenberg form. The application of the Arnoldi method results in a projection of the full stability problem given by A onto the m -dimensional space

$$V_m^H A V_m = H_m, \quad (6.32)$$

where the basis V_m decides which eigenpairs (x_j, λ_j) of A are approximated. V^H marks the complex conjugate transpose of V . The method then performs QR iterations on the small Hessenberg matrix H_m which leads to the partial Schur decomposition of A :

$$A Q_m = Q_m U_m, \quad Q_m \in \mathbb{C}^{n \times n}, \quad U_m \in \mathbb{C}^{n \times n}. \quad (6.33)$$

It can be shown that this decomposition always exists and the diagonal elements of U_m represent a specific subset of eigenvalues of the full QR decomposition. Thus the Arnoldi method produces an approximation of a specific subset of the eigenvalues of A .

Matrix-Free Implementation In addition to the significant reduction in problem dimension, another important element of the Arnoldi algorithm is its ability to be implemented *matrix-free*. This means, that the linearized

system matrix A never has to be explicitly constructed. Upon closer inspection, the algorithm only needs the results of matrix-vector products of the form Ax . These matrix vector products can be computed by the same, unmodified numerical code used for the direct numerical simulations of the nonlinear Navier-Stokes equations. The Fréchet derivative of the nonlinear Navier-Stokes operator $N(q(x, y, z, t))$ in the direction of v_i is approximated by, see [104],

$$Av_i = \frac{N(\bar{q} + \epsilon v_i) - N(\bar{q})}{\epsilon}, \quad (6.34)$$

where ϵ needs to be specified by the user. This first order approximation of the linearized operator allows the application of the Arnoldi method without an explicit calculation of the linearized Navier-Stokes equations using the framework of an existing DNS solver. Schulze et. al, [104], showed that a higher order approximation of the derivative does not improve the accuracy of the stability computation. The choice of the specific parameter ϵ is not trivial however. A choice of ϵ that is too large implies a bad approximation of the derivative, while a small ϵ can generate round-off errors. This work follows Schulze by choosing ϵ as:

$$\epsilon = \|\bar{q}\|_2 \sqrt{\epsilon_0}, \quad (6.35)$$

where ϵ_0 corresponds to the machine precision.

Modifications Numerous modifications to the basic Arnoldi method exist. Usually the quality of the approximations improves with the dimension of the Krylov subspace \mathcal{K}_m . However, in the actual application of the method, the subspace dimension is limited by the available memory. To limit the subspace dimension m , the Arnoldi decomposition can be periodically restarted. An example of such a technique is the IRAM, or *implicitly restarted arnoldi method*. Developed by Sorensen, see [107], the IRAM computes a new starting vector in such a way, that k desired Ritz vectors are favored, while the remaining $m - k$ vectors are damped. Besides reducing the number of subspaces needed, this implicit restarting can be used as a simple method of convergence control. While the basic Arnoldi method converges, much like the Power iteration, to eigenvalues with large modulus, the restarting procedure can be used to favor eigenvalues with, e.g., the largest real part, see [51]. Mack, see [56], states that the Arnoldi algorithm restarted in such a way converges towards unstable, $Re(\lambda > 0)$, or marginally stable, $Re(\lambda) \approx 0$, eigenvalues. This is a very

favorable property of the algorithm as the spectrum, as approximated by the snapshot based DMD, of the SBFI system consists of almost all marginally stable eigenvalues in the relevant frequency range.

The Arnoldi method used in the following sections has been implemented and used within the NSF fluid solver framework of the FG Numerische Fluidodynamik for numerous years and in multiple contexts, including, but not limited to: stability analysis of the flow over a swept wing, [56, 58, 59]; analysis of compressible mixing layers, [57], and exponential time-integration using Krylov subspaces, [104]. It has therefore proven to be a reliable and robust framework for stability analysis. The current form of the algorithm is described in [35], its matrix-free implementation is based on the characteristic-type formulation of the direct and adjoint Navier-Stokes equations described e.g. in [105].

6.3.3. Adjoint Navier-Stokes Equations and Sensitivity Analysis - Theory

The adjoint Navier-Stokes equation play an increasingly prominent role in fluid dynamics. In fluid dynamics, their use dates back to Jameson in 1988 in optimal control and aerodynamic shape design, see [39], and Hill, in [36], applied to passive control of cylinder flow. Since then, adjoint methods have become more wide-spread in their application to fluid dynamic problems. The most frequent applications are adjoint-based optimization methods, e.g. [52, 102, 103, 105], and stability and sensitivity analysis of complex flows. In adjoint-based optimization, the use of the adjoint greatly reduces the computational effort of gradient-based optimization methods where the gradient can be computed via the solution to the adjoint Navier-Stokes equation. In stability theory, the eigenmodes of the adjoint operator play an integral part in solving the eigenvalue perturbation problem. That is, how does an eigenvalue λ change when the operator A is changed by a small perturbation?

The following section will introduce the basic concept of the adjoint operator, its relation to eigenvalue sensitivity as well as an overview of how these theories apply, and how their results can be interpreted, in the context of fluid flow.

The Adjoint Operator Given a scalar product (\cdot, \cdot) on the space K , an operator $A : K \rightarrow K$ and $u, v \in K$, the adjoint operator A^* is defined by the

relation:

$$(Au, v) = (u, A^*v). \quad (6.36)$$

In the case of $K = \mathbb{C}^n$ and $A \in \mathbb{C}^{n \times n}$, $A^* = A^H$, where A^H is the complex conjugate transpose of A .

The Perturbed Eigenvalue Problem The most simple example of eigenvalue sensitivity analysis is the following matrix perturbation problem. Given an eigenvalue problem

$$\lambda v = Av, \quad (6.37)$$

how does λ change if A is perturbed? This can be written in a simple expansion of the above equation as

$$(\lambda + \delta\lambda)(v + \delta v) = (A + \delta A)(v + \delta v). \quad (6.38)$$

Here δA is the given, small matrix perturbation and δv and $\delta\lambda$ are the resulting perturbations of the eigenpair. Equation (6.38) is left-multiplied with the unknown vector v^* and rearranged to yield

$$v^{*H}(A - \lambda I)\delta v = v^{*H}(\delta A - \delta\lambda I)v, \quad (6.39)$$

where I is the identity matrix. The left-hand side is required to be identically zero for all possible perturbations δv . This leads to an equation for the as-of-yet unknown vector v^* :

$$v^{*H}(A - \lambda I) = 0 \quad (6.40)$$

$$\Rightarrow (A^H - \bar{\lambda}I)v^* = 0 \quad (6.41)$$

$$\Rightarrow \bar{\lambda}v^* = A^H v^*. \quad (6.42)$$

Therefore v^* is the eigenvector of the adjoint operator $A^H = A^*$ with the eigenvalue $\bar{\lambda}$, which is just the complex conjugate of λ . The eigenvector v^* is often referred to as the left eigenvector of A . Now equation (6.39) can be written in the desired form

$$\delta\lambda = \frac{v^{*H}\delta Av}{v^{*H}v}. \quad (6.43)$$

The change in the eigenvalue λ is therefore intrinsically dependent on the solution to the adjoint eigenvalue problem (6.42).

Bi-Orthogonality There exists another relation between the direct and adjoint eigenvalue problem apart from the relation $\lambda_i = \bar{\lambda}_i$, which dictates that the adjoint, or left, eigenvalues are complex conjugates of the direct, or right, eigenvalues. Starting from

$$((\bar{\lambda}_j - A^H)v_j^*, v_j) = 0, \quad (6.44)$$

one can arrive at the so-called bi-orthogonality condition

$$(v_j^*, v_i) = \delta_{ij}. \quad (6.45)$$

In sensitivity analysis, this relation is heavily used to project initial conditions or external forcing onto the systems eigenvectors. See Schmid, [99], for a comprehensive overview.

The Adjoint Navier-Stokes Equations As has been demonstrated, the solution to the eigenvalue sensitivity problem depends critically on the adjoint operator. In the matrix case, the adjoint can be easily constructed via the application of the matrix transpose. In principle, the discretized linearized Navier-Stokes equations can be expressed as an explicit matrix operator. However, due to the presence of complex boundary conditions or the implicit construction of the linearization via Frechet derivatives, see section 6.3.2, this is not always possible. In those cases, the adjoint operator of the continuous linearized Navier-Stokes equations has to be constructed. There exists the question whether it is advisable to first discretize the equations and then construct the adjoint operator or vice versa. Jameson et al., [69], provide an overview of the advantages and disadvantages of both techniques. As the eigenvalue solver used for this work operates matrix-free, and therefore the explicit system matrix A is not known, the continuous adjoint approach is used here.

In principle, the construction of the continuous adjoint is not different from the discrete case. The underlying scalar product is based on the \mathcal{L}^2 norm as $(u, v) = \int_{\Omega} u \cdot v d\Omega$. The adjoint equations can then be formed by multiplication with a test function and integration by parts. The reader is redirected to Schulze, in [105], for the complete extensive derivation and validation of the adjoint Navier-Stokes equations employed here.

6.3.4. Applications to Fluid Mechanics - Physical Interpretation

The above notions introduce the basic concepts and motivations of sensitivity analysis and their dependence on the adjoint equations and its eigenpairs. In the following, the application of these concepts to the context of fluid mechanics is discussed. A physical interpretation of the adjoint eigenmodes is given. In addition the concepts of structural sensitivity - the wave maker region - and the concept of sensitivity to baseflow modifications are introduced. In this process no mathematical derivations will be presented but explanatory references will be provided.

Adjoint Modes and Receptivity The adjoint global mode v^* with the eigenvalue $\bar{\lambda}$ represents the field which projects maximally onto the appropriate direct mode with eigenvalue λ . As Schmid et al. discuss in [99], the adjoint mode is a direct representative of the receptivity of the associated direct mode. This means that the maxima of the adjoint mode are the regions of the base flow, where forcing is most effective in exciting the direct mode. Barone and Lele provide a more detailed discussion of receptivity in compressible flows in [5].

The Wave-Maker Giannetti et al. introduced the concept of structural sensitivity - also called the *wave-maker* - in [29]. The pointwise product of direct and adjoint velocity modes uu^* can be interpreted as follows: Regions with a large modulus of uu^* represent areas where forcing proportional to the local velocity has the highest influence on the shift in eigenvalue. Therefore these regions are assumed to be the core of the corresponding instabilities since small perturbations there have the largest influence on the development of the instability. An interesting note follows: As the product uu^* is a complex number, it can be divided into its real and complex part. Where the real part of the sensitivity corresponds to shifts in eigenvalue growth rate, the complex part corresponds to changes in eigenvalue frequency.

Sensitivity to Baseflow Modifications Since the aim of the global stability analysis in the SBLI case was to assess methods to control or dampen the low-frequency oscillations, the sensitivity to base-flow modifications is the most interesting application of adjoint sensitivity analysis for this case. This sensitivity shows how an eigenvalue changes when the underlying base-flow is changed. Such a base-flow change could correspond to passive flow

Procedure 6.2: Computation of Sensitivity to Baseflow Modifications

1. Solve the direct eigenvalue problem for the linearized Navier-Stokes equations and select an eigenpair (λ_i, v_i) .
2. Solve the adjoint eigenvalue problem for the corresponding adjoint eigenpair $(\bar{\lambda}_i, v_i^*)$
3. Normalize the adjoint mode such that $(v_i, v_i^*) = 1$
4. Compute the sensitivity to base-flow modifications as

$$\Delta_U \lambda = -(\nabla u^H) \cdot u^* + \nabla u^* \cdot \bar{u}. \quad (6.46)$$

control mechanisms such as blowing or suction in a boundary-layer, simple obstacles placed in the flow or small changes of the geometry that effect the base-flow. The framework used for this sensitivity study in SBLLI follows Marquet, Sipp and Jacquin, [60]. There, the authors compute the sensitivity to base-flow modifications for the incompressible Navier-Stokes equations via a Lagrangian approach. To compute the sensitivity, four steps are required. These steps, given in procedure 6.2, conveniently yield all information necessary to extract the aforementioned sensitivity information.

As in the previous case of the wave-maker, the sensitivity can be split into a real and an imaginary part, representing sensitivity of the damping rate and frequency respectively. It must be noted that this approach and the specific form of the sensitivity depend on the incompressibility assumption which is clearly violated in the case of transonic, shock-laden flow. It is used because the author is not aware of a similar method developed for compressible flow. All results generated this way therefore have to be examined very critically taking into account the results of the receptivity and wave-maker approach which are equally valid for the compressible case. As such, they represent a first guess at the correct sensitivity of the low-frequency unsteadiness. Further studies and simulations with implemented modifications are necessary to fully assess the validity of the sensitivity calculations.

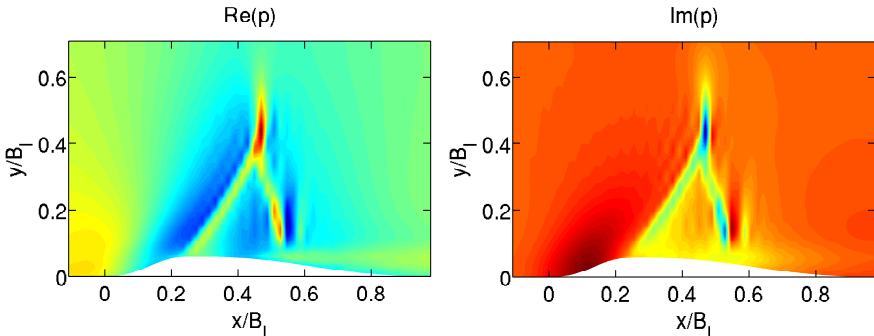


Figure 6.13.: Real (left) and imaginary (right) pressure component of the shock-mode corresponding to $St = 0.0039$. Colorscale is chosen for best visibility.

6.4. Sensitivity Analysis of a Transonic SBLI

The previous section gave an overview of sensitivity theory. This part of the chapter describes the results of said theory applied to the case of transonic SBLI. Linear stability analysis will be applied to extract the direct and corresponding adjoint modes associated with the low-frequency shock-motions. These modes will then be used to compute the receptivity of the flow, extract the wave-maker region and finally the sensitivity to base-flow modifications. The results of these derivations will be interpreted as to provide insight into the physical mechanisms governing the low-frequency oscillations.

6.4.1. Direct Modes

For the computation of the eigenmodes, the original three-dimensional flow field is reduced in two steps. First, the field is reduced by spanwise averaging of the mean flow field. This reduction to a two-dimensional field for the modal decomposition has been verified to yield suitable results in the DMD analysis in the previous section and the results of Crouch et al. in [17]. In an additional step, the now two-dimensional field is reduced by omitting every second point. This is done to reduce the memory needed for eigenvalue computation. In addition, as can be seen from the DMD results, the modes of interest contain no small scale turbulent structures and therefore the coarser resolution of the field will not affect the shape of the low-frequency modes. The base flow around which the flow is linearized is the spanwise and

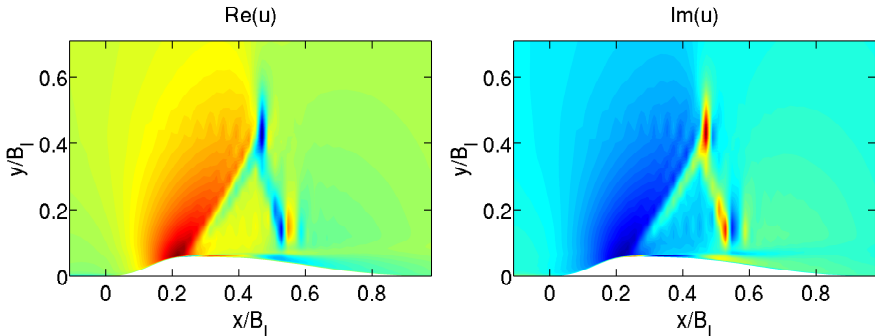


Figure 6.14.: Real (left) and imaginary (right) streamwise velocity component of the shock-mode corresponding to $St = 0.0039$. Colorscale is chosen for best visibility.

temporally averaged mean field. The spatial window which is used for the stability analysis is the same as for the DMD decomposition. The resulting eigensystem is solved using the Arnoldi algorithm described within [35] with up to $p = 10.000$ subspaces. The Ritzvectors corresponding to the eigenvalue approximations in the Strouhalregion of interest have been checked to be true approximations to the original eigensystem by checking the residual $\lambda_i v - Av \ll \|v\|$, and all vectors not matching this criterion have been discarded. In figures 6.13-6.14 both real and imaginary parts of pressure and streamwise velocity of the eigenmode with $St = 0.0039$ are depicted. The magnitude of the corresponding eigenvalue λ_s is $|\lambda_s| \approx 1$, with the temporal growth rate being very slightly damping. The shape of the mode agrees very well with mode M_1 obtained from the dynamic mode decomposition in 6.3. This similarity furthers confirms the accuracy of the eigenvalue computation. The streamwise velocity depicted in figures 6.14 reveals the contribution of the low-frequency mode to the recirculation bubble as well as the presence of the λ -foot in the velocity profile.

The computation of these direct modes does not offer relevant new information when compared to the results of the previous section on the DMD. This is expected as the dynamical decomposition is in itself an approximation of the global stability information of the transonic SBLI system. Therefore the good agreement of both approaches to the same problem helps validate the results further. In addition it lends confidence to the following results obtained for the adjoint system, where comparisons with other methods can not be obtained.

Source	Adjoint expression for receptivity
Point mass source at x_0	$\rho^*(x_0)$
Point velocity source at x_0	$u_i^*(x_0)$
Point pressure source at x_0	$p^*(x_0)$
Surface normal blowing at x_0	$v^*(p^*(x_0) + \frac{M}{Re} T_{ii}^*(x_0))$

Table 6.2.: Adjoint expressions for receptivity as given by Barone and Lele, [5]

6.4.2. Adjoint Modes

The adjoint Eigenproblem is constructed around the same baseflow and the Arnoldi algorithm with the same parameters as before is used to solve it. The bi-orthogonality condition was successfully checked for all modes detected within the low-frequency Strouhalregion that were confirmed to be true solutions of the adjoint eigensystem by the same method as in the direct case. The adjoint mode corresponding to the main direct low-frequency mode is depicted in pressure and streamwise velocity in the figures 6.15 and 6.16. As described in section 6.3.4, the shape of the mode allows a qualitative measurement of where the direct mode can be influenced. The depictions of pressure and velocity show three main regions of interest. These are the ascending part of the bump where the fluid is accelerated, the impingement point of the leading shock as well as the recirculation and vortex shedding zone beneath the λ -shock. The adjoint variable connected to pressure shows an oscillation structure centered at $x = 0.255B_l$, the impingement point of the leading shock. The structure emanates from the boundary-layer at the bump and is advected upstream, as expected for the adjoint equations. The second concentration region of the pressure mode is region between both λ -feet. No significant low frequency activity is detected downstream of $x = 0.54B_l$. The velocity field of the adjoint mode, see fig 6.16, shows a larger emphasis the region of accelerated flow on the upstream side of the bump. While adjoint velocity fluctuations are not as pronounced at the front shock, the stable region of the recirculation zone is clearly visible in adjoint velocity.

Receptivity In Barone et al, [5], the authors introduce and expand the concept of receptivity of a mode to compressible flows. In basic terms, the receptivity of a mode is the process by which external disturbances excite instabilities within a flow. Regions of high receptivity can therefore be interpreted as regions where disturbances have large influence on the qualitative

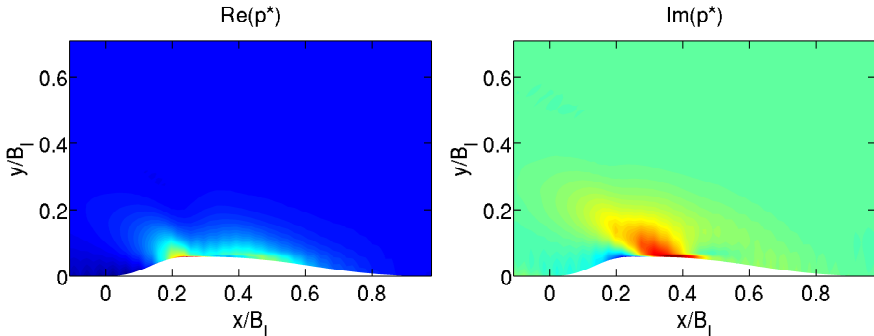


Figure 6.15.: Real (left) and imaginary (right) pressure component of the adjoint mode corresponding to the low-frequency shock oscillations, $St = 0.0039$. Colorscale is chosen for best visibility.

behavior of the original mode. Barone and Lele derive expressions for the receptivity of point sources which are reported in table 6.2. In qualitative terms, the influence of a pressure or velocity point source is given by the pressure and velocity of the adjoint modes, respectively.

Figure 6.17 displays the receptivity to pressure and streamwise velocity disturbances measured through the amplitude of adjoint pressure and velocity. The adjoint pressure modulus reveals that the impingement point of the leading shock is a prime candidate for influencing the low-frequency shock motions. In addition, disturbances in the stable part of the recirculation bubble can excite the dynamics of the flow significantly. Receptivity to streamwise velocity disturbances is situated slightly different. While the leading shock foot is still a local maxima of receptivity, the region of receptivity in the recirculation region has shifted downstream. It is now situated in the vortex shedding region below the rear leg of the λ -system. Most significantly, the most receptive part of the flow is the upstream region of the bump where the flow is accelerated before the bump throat. Velocity sources here have the ability to change the nature of the shock movements significantly.

The Wave-Maker The wave-maker region, identified by extrema in the pointwise product of the direct and adjoint modes, allows the identification of the *core* of the corresponding instability. Applied to the low-frequency oscillations of interest, the regions where these shock-movements are amplified can be found. Figure 6.18 shows both the real and imaginary part of the streamwise velocity wavemaker uu^* . The real part of the wavemaker shows

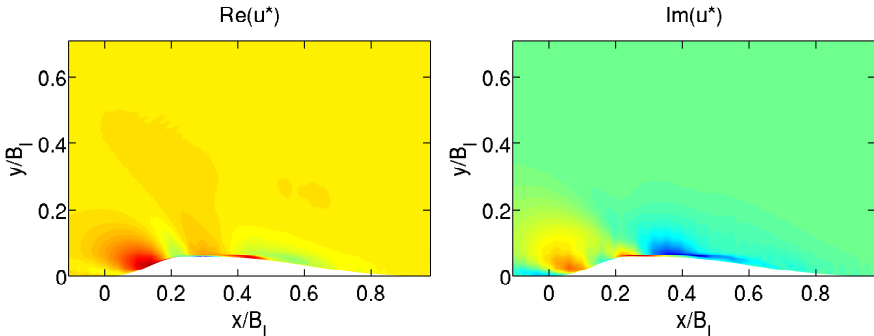


Figure 6.16.: Real (left) and imaginary (right) streamwise velocity component of the adjoint mode corresponding to the low-frequency shock oscillations, $St = 0.0039$. Colorscale is chosen for best visibility.

the origin of the development of the instability at the leading shock impingement point and the beginning of the recirculation bubble. Here, the high gradients of the flow and the developing mixing layer between the freestream and the recirculation bubble can amplify occurring disturbances significantly. In addition, the upstream side of the bump features a larger maximum region. Disturbances introduced here will be transported towards the leading shock where their arrival may facilitate the movement of the shock. Lastly, the region of vortex detachment below the rear shock features levels of uu^* that are significantly larger than their surroundings. The imaginary part of the structural sensitivity mirrors the structure of the real part with one exception. The sensitive region on the upwards slope of the bump is missing. However, the frequency is more responsive to perturbations introduced just upstream of the leading shock impingement point.

It is noteworthy how well these results match up with the feedback loop cautiously identified in chapter 5. The instability seems to originate in the spatial regions where the connecting, intermediate frequency of $St = 0.032$ has been found within the flow. The bursting frequency associated with this Strouhal number has been found on the upwards slope of the bump, left of the leading shock, the vortex detachment with $St = 0.032$ takes place within the recirculation bubble while the upstream traveling pressure waves are generated in the vortex wake.

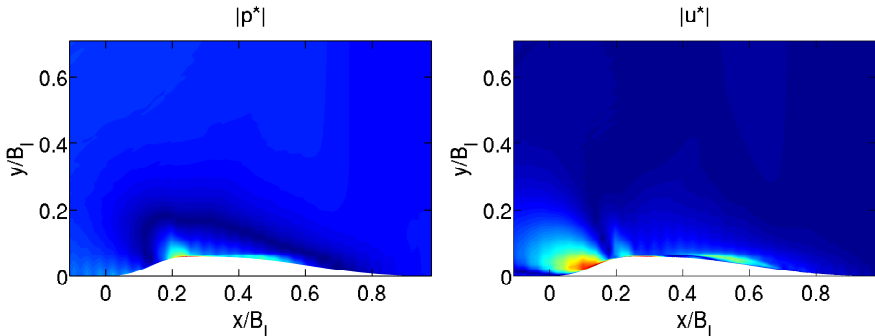


Figure 6.17.: Amplitude of adjoint pressure (left) and streamwise velocity (right) of the adjoint mode corresponding to the low-frequency shock oscillations, $St = 0.0039$. Colorscale is chosen for best visibility.

6.4.3. Sensitivity to Baseflow Modifications

As laid out before, the sensitivity of eigenvalues to baseflow modifications can be computed from a combination of the corresponding direct and adjoint eigenmodes. Although the specific ansatz used here was developed for incompressible flows, information can still be obtained from applying it to the compressible shock-laden SBLI flow. As will be seen, the results match up very well with the previous compressible analysis on receptivity but offer additional information on the flows response to external modifications. This sensitivity can be split up into the sensitivity of the damping rate, $Re(\lambda)$, and the frequency, $Im(\lambda)$. As the flow is two-dimensional for the stability analysis, this approach yields a two-dimensional vector field for each respective sensitivity. Figure 6.19 depicts both sensitivities. Apart from two additions, the highly sensitive regions coincide with those detected in 6.17. In addition to the upstream part of the bump, the shock impingement point and the recirculation bubble, the front shock-leg as well as the region surrounding the supersonic tongue, where the upstream traveling waves are generated, are regions of high sensitivity. An interesting dichotomy arises between the sensitivity of the damping rate and the frequency. While the damping rate is most susceptible to baseflow modifications in the acceleration region upstream of the shock, the frequency can be influenced most effectively at the shock impingement point. The amplitude indicates regions of large sensitivity, however, more information can be gained by considering the two-dimensional vector field. In principle, $\delta Re(\lambda)$ and $\delta Im(\lambda)$ are gradients. Therefore changes

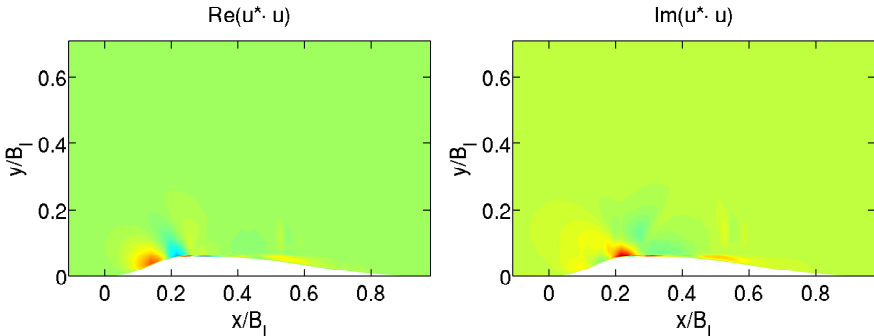


Figure 6.18.: Real (left) and imaginary (right) component of the streamwise velocity wavenumber corresponding to the low-frequency shock oscillations, $St = 0.0039$. Colorscale is chosen for best visibility.

in line with the gradient will result in an increase of the considered quantity, while changes in the opposite direction result in a decrease. Figure 6.19 contains streamlines of the gradients which allow more detailed analysis of the results.

As the main interest of this study is the prevention of shock oscillation in the first place, the following discussion begins with an analysis of the damping rate.

Damping Rate The sensitivity of the damping rate reaches its maximum values at a streamwise position of $x \approx 0.16B_l$, right at the upstream ascend of the bump. Here the flow is accelerated before the leading shock impinges on the wall at $x = 0.255B_l$. In most basic terms, changes in the baseflow velocity at this position would change the Mach number of the flow in front of the leading shock. Thereby the position of shock formation and the shock Mach number would change. The vectorfield of the gradient indicates that a baseflow change adverse to the flow direction would lead to the damping of the low-frequency motions of the SBLI system. Such a change of the baseflow decreases the Mach number of the flow which generally reduces the strength of shock-oscillations as described in section 4. In the extreme case, the flow would become subsonic, preventing a shock to occur at all. In front of the impingement point, the streamlines point in upstream direction. Just behind the shock, where the recirculation bubble starts, the sensitivity streamlines point in wall normal direction. Interpreted as velocity modifications this means that an acceleration of the flow just before the leading shock leads to a damping of

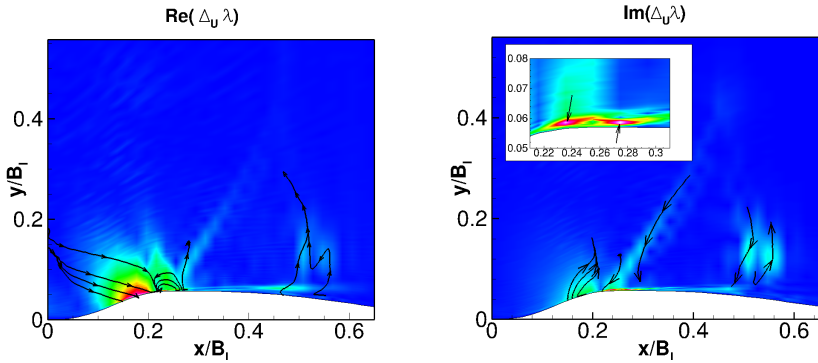


Figure 6.19.: Real(left) and imaginary (right) component of sensitivity to baseflow modifications. The colorscale represent amplitude of $\text{Re}(\Delta_U \lambda)$ and $\text{Im}(\Delta_U \lambda)$ while the streamlines depict the slope of the gradient.

the oscillatory mode. Flow acceleration just in front of the separation point would push the bubble, and in turn the leading shock, downstream. The same holds true for a suction applied at the onset of the recirculation bubble. The flow stays attached longer and in turn bubble development is delayed. On the other hand, wall-normal blowing in this region would lead to a larger separation with a stronger onset, creating a stronger leading shock. The next regions of interest are the vortex wake following the end of the stable recirculation zone at $x = 0.434B_l$, as well as the region surrounding the supersonic tongue at $x = 0.543B_l$. The sensitivity streamlines again suggest that suction of the fluid in the wake region suppresses the vortex generation and in turn the low-frequency oscillations. The influence of velocity modifications in the supersonic tongue is less clear. However, previously this region was identified as an origin of the upstream traveling pressure waves. Therefore, baseflow modifications here would modify the upstream path of information going counterclockwise around the shock system. In chapter 5, these upstream traveling waves were identified as part of a feedback loop that might be connected with the formation of the low-frequency unsteadiness. In the dynamic mode decomposition, it was found that they belong to the phase-locked system of dominant four modes of the flow. It is therefore conceivable that suppression of the vortices breaks the feedback loop and inhibits the low-frequency oscillations.

Frequency The sensitivity of the frequency to baseflow modifications is concentrated in the same regions as the sensitivity of the damping rate. However, the position of its extrema, the streamlines and their physical interpretations differ. In the upstream region of the bump, the gradient streamlines indicate that an acceleration of the flow would increase the frequency of the shock movements. In contrast to the damping rate, frequency sensitivity reaches its maxima in the direct vicinity of the leading shock impingement point. Wall-normal blowing on the inside of the λ -foot, at $x = 0.27B_l$, would strengthen and enlarge the recirculation bubble which in turn seems to increase shock motion frequency. The larger separation bubble might lead to a stronger direct coupling of recirculation frequency and front shock movement. Since the DMD found the recirculation dynamics to be of higher frequency than the shock-motions, this could lead to an increased shock motion frequency.

According to 6.19, baseflow modifications in the regions between the terminating shock and the shocklet have a high influence on the frequency of shock mode. The sensitivity of the frequencies to modifications in the supersonic tongue is more emphasized than that of the damping rate in the same region. This suggests that the flow features originating here, the upstream traveling waves, are more important for setting the specific frequency of the oscillations than for triggering their onset. This could be explained by the phase-locked system of modes dominating the shock motions found in section 6.2. If frequency of the bursting and vortices, associated with mode M_4 changes, the frequency of shock oscillations, associated with mode M_1 , would need to change in order to preserve the phase relationship.

6.4.4. Conclusion

All the insight gained in this section emphasizes the importance of regions connected to the phase-locked system of bursting events, detachment of the recirculation zone and the upstream traveling waves identified in the time-series analysis and DMD of the SBLI system. All regions of high sensitivity of the low-frequency unsteadiness directly correspond to one of these phenomena. The adjoint shock mode only contains near-wall structures. So, while the shock itself is in its nature inviscid, its oscillation is dominated by viscous effects originating in the near-wall boundary-layer. Small disturbances of the flow field in the region below the shock-system, which is dominated by viscous effects, have large implications on the overall flow structure. This emphasizes the crucial fact that the boundary-layer has to be accurately resolved in the simulation of shock-wave/boundary-layer interaction. Any modeling assump-

tions arising in coarser simulations using turbulence models will have a large influence on the overall behavior of the system.

Besides the incoming Mach number of the flow, it seems that the actions of the recirculation bubble and its connected mechanisms have the greatest influence on the behavior of the shock motion. Therefore controlling this feature of the flow seems a promising ansatz for suppressing the low-frequency shock motions. The sensitivity to baseflow modifications suggests that inhibiting the formation of the recirculation bubble and suppressing the vortex shedding below the terminating shock and in the supersonic tongue provide the best ansatz to suppress the oscillations. The dynamic mode decomposition in section 6.2 revealed that the lowest frequency mode has no significant part in these two flow features. Therefore the receptivity and sensitivity results affirm the existence of a connection between different timescales. The feedback loop described both in chapters 5 and 6 could represent the driving force in this case of transonic SBLI.

The importance of downstream influences within the SBLI system is interesting. As can be seen, the structure of the SBLI flow can be changed by introducing baseflow modifications in regions that lie downstream of the actual λ -shock system, in the region where the upstream traveling waves are generated. This is a stark difference when compared to purely supersonic interactions. In those kind of SBLI, upstream influence can only happen through elliptic leakage in the subsonic part of the boundary-layer, placing even more importance on the recirculation bubble as the only path of upstream traveling information. In the transonic case, information can move around the shock and opens up a potential new feedback loop.

The sensitivity to baseflow modifications was obtained through an approach that neglects the compressibility of the fluid. Therefore its results in the vicinity of the shocks should be examined critically with this fact in mind. However, the similarities between receptivity and structural sensitivity on the one hand, and the sensitivity to baseflow modifications on the other hand lend plausibility to the results of the sensitivity analysis, prompting further studies to verify the results.

Conclusion and Outlook

Turbulent shock-wave/boundary-layer interactions present contain flow features which place competing demands on the numerics used for their computation. Within the first part of this thesis, a fully conservative, finite-difference discretization of the skew-symmetric Navier-Stokes equations has been presented and validated. While such methods have been known for some time, they have been restricted to limited order of accuracy in time and/or space. The method presented here is of arbitrary order in space and time while being comparably easy to implement in existing finite-difference solvers. Additionally, and critically important for complex physical simulations, boundary conditions and curvilinear grids could be implemented without changing the structure and underlying properties of the method. This conservative, skew-symmetric finite-difference methods has been validated for turbulent, shock-laden flow via simulations of inviscid shock test cases, forced and decaying isotropic turbulence at high Mach numbers as well as turbulent boundary-layer flow.

In the second part of this work, a direct numerical simulation of a transonic shock-wave/boundary-layer interaction has been performed using the previously described method. A subsonic, turbulent boundary-layer impinges on a bump-shaped obstacle and a λ -shock system forms. Analysis of the pressure spectra found low-frequency oscillations associated with shock-movement at a Strouhal number of $St = f\delta/u_0 = 0.0039$. This Strouhal number is matched in different simulations and experiments in supersonic interactions.

Almost exact matches exist with simulations of compression ramps by Grilli et al., [31], and impinging oblique shocks by Hadjadj, [33]. This similarity over a vast range of geometries, Reynolds- and Mach numbers confirms that underlying mechanism must exist that are common to all kinds of SBLI.

Statistical analysis of the flow within the interaction zone found indications of a possible loop connecting the low-frequency shock motions with a higher frequency connected to a) bursting events in the incoming boundary-layer, b) the shedding of vortices from the recirculation zone and c) the presence of pressure waves traveling upstream around the λ -system down to the leading shock impingement point. A dynamic mode decomposition of the flow-field was performed to identify the dynamical behavior of the system. Results of the DMD match almost perfectly with the previous results from the various timeseries discussed in the statistical analysis of the flow. The DMD identified a phase-locked set of 4 dominant modes governing the SBLI. The first two modes, M_1 and M_2 , describe the low-frequency movements of the shock-system. Mode M_3 contains small modulations of this movement while mode M_4 could be identified with the higher frequency of the loop identified in the previous discussion. Reconstructions of the flow show that this mode does not influence shock position or overall mass of the recirculation bubble significantly. However it is responsible for the existence of vortex shedding from the bubble and contains structures reminiscent of upstream traveling pressure waves and high Mach number events in the TBL just before the leading shock. A noteworthy result of the flow reconstruction is the apparent disconnect of the low-frequency shock oscillations and the dynamics of the recirculation bubble. A dynamic mode decomposition of a supersonic compression ramp performed by Grilli et al., in [31], found clear agreement between bubble expansion and contraction and the dominant shock movements. A possible connection between both features could be found in the existence of mode M_4 associated with the feedback loop. In summary, the DMD provides an excellent overview of the dominant flow features and supports the existence and importance of the cautiously identified feedback loop.

Following the dynamic mode decomposition, linear stability analysis of the direct and adjoint Navier-Stokes equations has been performed for the transonic SBLI case in order to derive information on the sensitivity of the shock-oscillations. The receptivity and structural sensitivity of the low-frequency oscillations has been derived. In addition, the sensitivity to baseflow modifications has been computed using an ansatz derived for the incompressible Navier-Stokes equations. While the results of the sensitivity have to be taken with caution, they agree very well with the receptivity computations. All

these results show that the low-frequency shock motions could be best influenced or damped using modifications that would inhibit or alter the aforementioned high-frequency phenomena.

Combining the results of the statistical analysis, the dynamic mode decomposition and the sensitivity analysis presents a good case for the existence of the proposed feedback loop: Small scale fluctuations of the leading shock trigger the shedding of vortices from the recirculation bubble. Those vortices travel downstream and interact with the terminating shock and the supersonic tongue. The vortices emit pressure waves that travel upstream around the shock system. They impinge on the leading shock where the loop starts anew.

These findings fit into the context of current research into the mechanisms of supersonic SBLI. Going back to Plotkin, both Pirozzoli et. al. and Toubert & Sandham explain the occurrence SBLI through the existence of a slightly damped oscillating mode that is fed energy through upstream, high-frequency turbulence. The dynamic mode decomposition confirmed that, in the transonic case, the SBLI extracts energy from the high-frequency modes dominating the incoming boundary-layer and amplifies the energy within the modes associated with the low-frequency unsteadiness. The incoming boundary-layer turbulence feeds energy into the small scale-shock oscillations associated with the bursting frequency which in turn lead to the formation of the feedback loop. While this path of action is plausible, the results of this work are not conclusive as to whether the feedback loop could be sustained without energy supplied from higher frequencies.

In summary, the fully conservative finite-difference method has proven to be an accurate and reliable way to treat shock-laden turbulent flow. In particular, the extension to arbitrary order and curvilinear grids facilitate the use of the method in large-scale physical problems. The simulation of a transonic shock-wave/boundary-layer interaction has identified a potential feedback loop that could govern the low-frequency oscillations. Both the dynamic mode decomposition and the sensitivity analysis provided valuable insight into the nature of the interaction that support the existence of the coupling of different the different timescales.

Future work could be used to extend and validate the results presented above. The DNS conducted here featured 3 full cycles of the low-frequency unsteadiness. Simulations over longer timeframes would improve the statistical analysis of the situation and grant higher confidence to the results. A larger spanwise extent of the domain would eliminate another potential source of error. The method for sensitivity analysis used within this work should be

extended to the compressible Navier-Stokes equations and the linear stability analysis could be applied to the three-dimensional flow field. Apart from these technical improvements on the methods employed within this work, some findings lend themselves for further research. More sophisticated stability analysis could be carried out in order to capture the modes associated with the bursting frequency. Insight into their damping rate would reveal whether the feedback loop is self-contained or needs to be fed with energy or actively feeds energy into the low-frequency unsteadiness. In general, the sensitivity analysis presents a compelling case for the use of adjoint-based methods in the analysis of SBLI. Using adjoint-based optimization methods with a target functional that minimizes the shock-oscillations could lead to new insight into the origin of the unsteadiness by looking into the algorithmically derived solutions.

Appendix A

The discrete, 3-dimensional Navier-Stokes Equations on Arbitrarily Distorted Grids

This appendix details the full three-dimensional semi-discrete Navier-Stokes equations on arbitrarily distorted grids. This formulation of the equations is used for all the simulations conducted within this thesis. It is assumed that the equations describe a Newtonian fluid and the ideal gas law is observed. The physical quantities are (x_1, x_2, x_3) , while the computational space is (ξ_1, ξ_2, ξ_3) . The local base vectors are

$$e_i = \partial_{\xi_i} r, \quad r = (x_1, x_2, x_3) \quad (\text{A.1})$$

and

$$J = (e_1 \times e_2) \cdot e_3 \quad (\text{A.2})$$

is the Jacobian of the grid transformation. In addition the following abbreviations are used:

$$m_{il} = (e_j \times e_k)_l, \quad (\text{A.3})$$

$$\tilde{U}_i = \sum_{j=1}^3 m_{ij} U_j, \quad (\text{A.4})$$

$$D_{x_i} = \sum_{j=1}^3 D_{\xi_j} m_{ji} \quad (\text{A.5})$$

This way, m_{il} is the l -th component of $(e_j \times e_k)$. \tilde{U} is the *representation* of velocity in the physical space and D_{x_i} is the derivative in physical space. Using these quantities, the equations are:

$$J\sqrt{R}(\sqrt{\rho})_t = -\frac{1}{2}D_{\xi_i}R\tilde{U}_i \quad (\text{A.6})$$

$$J\sqrt{R}(\sqrt{\rho}u_i)_t = -\frac{1}{2}\left(D_{\xi_j}R\tilde{U}_j + R\tilde{U}_jD_{\xi_j}\right)u_i - D_{x_i}p + D_{\xi_j}\tilde{\tau}_{ij} \quad (\text{A.7})$$

$$\begin{aligned} Jp_t = & -\gamma D_{\xi_i}\tilde{U}_ip + (\gamma - 1)U_iD_{x_i}p \\ & + (\gamma - 1)\left(D_{\xi_j}U_i\tilde{\tau}_{ij} - U_jD_{\xi_i}\tilde{\tau}_{ji} - D_{\xi_j}m_{ji}\bar{\Phi}_i\right). \end{aligned} \quad (\text{A.8})$$

The stresses, $\tilde{\tau}_{ij}$, and heat conduction, $\bar{\Phi}$, in physical space are:

$$J\tau_{ij} = \mu\bar{S}_{ij} + \delta_{ij}\left(\mu_d - \frac{2}{3}\mu\right)D_{\xi_k}\tilde{U}_k, \quad (\text{A.9})$$

$$\bar{S}_{ij} = (m_{kj}D_{\xi_k}u_i + m_{ki}D_{\xi_k}u_j), \quad (\text{A.10})$$

$$J\bar{\Phi}_i = -\lambda m_{ji}D_{\xi_j}T. \quad (\text{A.11})$$

The stress tensor τ_{ij} is then elevated to the physical domain in the same way as the velocity:

$$\tilde{\tau}_{ij} = \sum_k^3 m_{jk}\tau_{ik}. \quad (\text{A.12})$$

The equations (A.6)-(A.8) have the same conservative, skew-symmetric structure as the equations on uniform grids, (2.43)-(2.45). Therefore the results of theorems 1-4 apply.

Appendix B

Finite-Difference Schemes with the SBP Property

Within this section, the finite difference schemes with the summation by part property of order 2,4,6 and 8 are given. Strand, see [109] shows that the schemes order at the boundary is halved. The structure of scheme is

$$D = WQ \tag{B.1}$$

with $W = \text{diag}(w)$ being a diagonal weight matrix. The vector of weights w is symmetric in the sense that $w_{N-i} = w_i$ and all but the boundary elements are zero. The differentiation matrix Q is made up out off an interior stencil which has the classic central difference form

$$u'_i = \sum_{k=1}^m \alpha_k (u_{j+k} - u_{j-k}), \tag{B.2}$$

whose matrix form is denoted as D_{int} and a boundary stencil B such that

$$Q = \begin{pmatrix} B & 0 & 0 \\ 0 & D_{int} & 0 \\ 0 & 0 & -B \end{pmatrix} \tag{B.3}$$

2nd order interior, 1st order boundary

$$\alpha_1 = \frac{1}{2}$$

$$w_1 = \frac{1}{2}, \quad w_2 = 1$$

$$B = \begin{pmatrix} -1 & 1 & 0 \\ -\frac{1}{2} & 0 & \frac{1}{2} \end{pmatrix}$$

4th order interior, 2nd order boundary

$$\alpha_1 = \frac{8}{12}, \quad \alpha_2 = -\frac{1}{12}$$

$$w_1 = \frac{1}{2}$$

$$B = \begin{pmatrix} -\frac{7}{12} & \frac{8}{12} & -\frac{1}{12} & 0 \\ -\frac{6}{12} & -\frac{1}{12} & \frac{8}{12} & -\frac{1}{12} \end{pmatrix}$$

6th order interior, 3rd order boundary

$$\alpha_1 = \frac{3}{4}, \quad \alpha_2 = -\frac{3}{20}, \quad \alpha_3 = -\frac{1}{60}$$

$$\begin{aligned} w_1 &= \frac{13649}{43200}, & w_2 &= \frac{12013}{8640}, & w_3 &= \frac{2711}{4320}, \\ w_4 &= \frac{5359}{4320}, & w_5 &= \frac{7877}{8640}, & w_6 &= \frac{43801}{43200} \end{aligned}$$

$$B = \begin{pmatrix} -\frac{21600}{13649} & \frac{81763}{40947} & \frac{131}{27298} & -\frac{9143}{13649} & \frac{20539}{81894} & \dots \\ -\frac{81763}{180195} & 0 & \frac{7357}{36039} & \frac{30637}{72078} & -\frac{2328}{12013} & \dots \\ -\frac{131}{54220} & -\frac{7357}{16266} & 0 & \frac{645}{2711} & \frac{11237}{32532} & \dots \\ \frac{9143}{53590} & -\frac{30637}{64308} & -\frac{645}{5359} & 0 & \frac{13733}{32154} & \dots \\ -\frac{20539}{236310} & \frac{2328}{7877} & -\frac{11237}{47262} & -\frac{13733}{23631} & 0 & \dots \\ 0 & -\frac{6611}{262806} & \frac{3487}{43801} & \frac{1541}{87602} & -\frac{89387}{131403} & \dots \\ \dots & 0 & 0 & 0 & 0 & \dots \\ \dots & \frac{6611}{360390} & 0 & 0 & 0 & \dots \\ \dots & -\frac{3487}{27110} & 0 & 0 & 0 & \dots \\ \dots & -\frac{67}{4660} & \frac{72}{5359} & 0 & 0 & \dots \\ \dots & \frac{89387}{118155} & -\frac{1296}{7877} & \frac{144}{7877} & 0 & \dots \\ \dots & 0 & \frac{32400}{43801} & -\frac{6480}{43801} & \frac{720}{43801} & \dots \end{pmatrix}$$

8th order interior, 4th order boundary

$$\alpha_1 = \frac{4}{5}, \quad \alpha_2 = -\frac{1}{5}, \quad \alpha_3 = \frac{4}{105}, \quad \alpha_4 = -\frac{1}{280}$$

$$w_1 = \frac{1498139}{5080320}, \quad w_2 = \frac{1107307}{725760}, \quad w_3 = \frac{1304999}{725760}, \quad w_4 = \frac{299527}{725760},$$

$$w_5 = \frac{103097}{80640}, \quad w_6 = \frac{670091}{725760}, \quad w_7 = \frac{5127739}{5080320}$$

$$B = \begin{pmatrix}
 \begin{array}{cccccc}
 \frac{-2540160}{1498139} & \frac{37052897}{17977668} & \frac{7891273}{8988834} & \frac{-7624221}{2996278} & \frac{15181679}{8988834} & \frac{-6971555}{17977668} & \dots \\
 \frac{5293271}{13287684} & 0 & \frac{-2931787}{6643842} & \frac{12616429}{6643842} & \frac{-697088}{4429228} & \frac{4026475}{6643842} & \dots \\
 \frac{607021}{603666} & \frac{2931787}{1121094} & 0 & \frac{-23428253}{2242188} & \frac{9447614}{560547} & \frac{-217571}{20761} & \dots \\
 \frac{7624221}{18269986} & \frac{-12616429}{7829994} & \frac{23428253}{15659988} & 0 & \frac{-2184329}{1304999} & \frac{7700062}{3914997} & \dots \\
 \frac{-15181679}{12580134} & \frac{6970881}{1198108} & \frac{-9447614}{898581} & \frac{2184329}{299527} & 0 & \frac{-10921405}{3594324} & \dots \\
 \frac{6971555}{77941332} & \frac{-4026475}{5567238} & \frac{217571}{103097} & \frac{-7700062}{2783619} & \frac{10921405}{11134476} & 0 & \dots \\
 0 & \frac{101360}{670091} & \frac{-2847947}{4020546} & \frac{3371361}{2680364} & \frac{-3604685}{4020546} & \frac{-1714837}{4020546} & \dots \\
 0 & 0 & \frac{1185475}{61532868} & \frac{-2783695}{30766434} & \frac{1462269}{10255478} & \frac{1022551}{30766434} & \dots \\
 \dots & 0 & 0 & 0 & 0 & 0 & \dots \\
 \dots & \frac{-101360}{1107307} & 0 & 0 & 0 & 0 & \dots \\
 \dots & \frac{2847947}{1121094} & \frac{-1185475}{15695316} & 0 & 0 & 0 & \dots \\
 \dots & \frac{-3371361}{5219996} & \frac{2783695}{54809958} & 0 & 0 & 0 & \dots \\
 \dots & \frac{3604685}{1797162} & \frac{-1462269}{4193378} & \frac{-2592}{299527} & 0 & 0 & \dots \\
 \dots & \frac{1714837}{5567238} & \frac{-1022551}{38970666} & \frac{3075}{103097} & \frac{-288}{103097} & 0 & \dots \\
 \dots & 0 & \frac{6445687}{8041092} & \frac{-145152}{670091} & \frac{27648}{670091} & \frac{-2592}{670091} & 0 \\
 \dots & \frac{-45119809}{61532868} & 0 & \frac{4064256}{5127739} & \frac{-1016064}{5127739} & \frac{193536}{5127736} & \frac{-18144}{5127739}
 \end{array}
 \end{pmatrix}$$

Bibliography

- [1] Nikolaus A Adams. Direct simulation of the turbulent boundary layer along a compression ramp at $m=3$ and $re_{\theta}=1685$. *Journal of Fluid Mechanics*, 420:47–83, 2000.
- [2] JA Andreopoulos and KC Muck. Some new aspects of the shock-wave/boundary-layer interaction in compression-ramp flows. *Journal of Fluid Mechanics*, 180(1):405–428, 1987.
- [3] Walter Edwin Arnoldi. The principle of minimized iterations in the solution of the matrix eigenvalue problem. *Quarterly of Applied Mathematics*, 9(1):17–29, 1951.
- [4] Holger Babinsky. *Shock wave-boundary-layer interactions*. Cambridge University Press, Cambridge New York, 2011.
- [5] Matthew F Barone and Sanjiva K Lele. Receptivity of the compressible mixing layer. *Journal of Fluid Mechanics*, 540:301–335, 2005.
- [6] GA Blaisdell, NN Mansour, and WC Reynolds. Compressibility effects on the growth and structure of homogeneous turbulent shear flow. *Journal of Fluid Mechanics*, 256:443–485, 1993.
- [7] GA Blaisdell, ET Spyropoulos, and JH Qin. The effect of the formulation of nonlinear terms on aliasing errors in spectral methods. *Applied Numerical Mathematics*, 21(3):207–219, 1996.
- [8] Christophe Bogey, Nicolas De Cacqueray, and Christophe Bailly. A shock-capturing methodology based on adaptative spatial filtering for high-order non-linear computations. *Journal of Computational Physics*, 228(5):1447–1465, 2009.

- [9] Olivier Bron. *Numerical and Experimental study of shock boundary layer interaction in unsteady transonic flow*. PhD thesis, KTH, 2003.
- [10] Jens Brouwer, Julius Reiss, and Jörn Sesterhenn. Fully conservative finite-difference schemes of arbitrary order for compressible flow. *AIP Conference Proceedings*, 1479(1):2290–2293, 2012.
- [11] Jens Brouwer, Julius Reiss, and Jörn Sesterhenn. Conservative finite differences as an alternative to finite volume for compressible flows. In Jürgen Fuhrmann, Mario Ohlberger, and Christian Rohde, editors, *Finite Volumes for Complex Applications VII-Methods and Theoretical Aspects*, volume 77 of *Springer Proceedings in Mathematics & Statistics*, pages 169–176. Springer International Publishing, 2014.
- [12] Jens Brouwer, Julius Reiss, and Jörn Sesterhenn. Conservative time integrators of arbitrary order for skew-symmetric finite-difference discretizations of compressible flow. *Computers & Fluids*, 100(0):1 – 12, 2014.
- [13] John C Butcher. Implicit runge-kutta processes. *Mathematics of Computation*, 18(85):50–64, 1964.
- [14] Kevin K Chen, Jonathan H Tu, and Clarence W Rowley. Variants of dynamic mode decomposition: boundary condition, koopman, and fourier analyses. *Journal of nonlinear science*, 22(6):887–915, 2012.
- [15] Noel T Clemens and Venkateswaran Narayanaswamy. Low-frequency unsteadiness of shock wave/turbulent boundary layer interactions. *Annu. Rev. Fluid Mech*, 46:469–92, 2014.
- [16] GJ Cooper. Stability of runge-kutta methods for trajectory problems. *IMA journal of numerical analysis*, 7(1):1–13, 1987.
- [17] JD Crouch, A Garbaruk, and D Magidov. Predicting the onset of flow unsteadiness based on global instability. *Journal of Computational Physics*, 224(2):924–940, 2007.
- [18] Lars Davidson. Reynolds stress transport modelling of shock-induced separated flow. *Computers & fluids*, 24(3):253–268, 1995.
- [19] Jean Détery, John G Marvin, and E Reshotko. Shock-wave boundary layer interactions. Technical report, DTIC Document, 1986.

-
- [20] David S Dolling. 50 years of shock wave/boundary layer interaction — what next? *AIAA*, 2000.
- [21] F Ducros, F Laporte, T Souleres, V Guinot, P Moinat, and B Caruelle. High-order fluxes for conservative skew-symmetric-like schemes in structured meshes: application to compressible flows. *Journal of Computational Physics*, 161(1):114–139, 2000.
- [22] P Dupont, C Haddad, and JF Debiève. Space and time organization in a shock-induced separated boundary layer. *Journal of Fluid Mechanics*, 559:255–277, 2006.
- [23] T. M. Eidson and G. Erlebacher. Implementation of a fully balanced periodic tridiagonal solver on a parallel distributed memory architecture. *Concurrency: Practice and Experience*, 7(4):273–302, 1995.
- [24] W. J. Feiereisen, W. C. Reynolds, and J. H. Ferziger. Numerical simulation of a compressible homogeneous, turbulent shear flow, nasa-cr-164953; su-tf-13. Technical Report NASA-CR-164953; SU-TF-13, NASA, 1981.
- [25] K. Finke. *Stoßschwingungen in schallnahen Strömungen*. VDI Verlag, 1977. VDI-Forschungsheft 580.
- [26] Travis C Fisher, Mark H Carpenter, Jan Nordström, Nail K Yamaleev, and Charles Swanson. Discretely conservative finite-difference formulations for nonlinear conservation laws in split form: Theory and boundary conditions. *Journal of Computational Physics*, 234:353–375, 2013.
- [27] B Ganapathisubramani, NT Clemens, and DS Dolling. Low-frequency dynamics of shock-induced separation in a compression ramp interaction. *Journal of Fluid Mechanics*, 636:397–425, 2009.
- [28] Gregor J Gassner. A skew-symmetric discontinuous galerkin spectral element discretization and its relation to sbp-sat finite difference methods. *SIAM Journal on Scientific Computing*, 35(3):A1233–A1253, 2013.
- [29] Flavio Giannetti and Paolo Luchini. Structural sensitivity of the first instability of the cylinder wake. *Journal of Fluid Mechanics*, 581:167–197, 2007.

- [30] Muzio Grilli. *Analysis of the unsteady behavior in shockwave turbulent boundary layer interaction*. PhD thesis, Technische Universität München, 2013.
- [31] Muzio Grilli, Peter J Schmid, Stefan Hickel, and Nikolaus A Adams. Analysis of unsteady behaviour in shockwave turbulent boundary layer interaction. *Journal of Fluid Mechanics*, 700:16–28, 2012.
- [32] Stephen E Guarini, Robert D Moser, Karim Shariff, and Alan Wray. Direct numerical simulation of a supersonic turbulent boundary layer at mach 2.5. *Journal of Fluid Mechanics*, 414:1–33, 2000.
- [33] Abdellah Hadjadj. Large-eddy simulation of shock/boundary-layer interaction. *AIAA journal*, 50(12):2919–2927, 2012.
- [34] Ernst Hairer, Christian Lubich, and Gerhard Wanner. *Geometric numerical integration: structure-preserving algorithms for ordinary differential equations*, volume 31. Springer, 2006.
- [35] O. Henze, M. Lemke, and J. Sesterhenn. A parallel and matrix free framework for global stability analysis of compressible flows. Technical report, Institut für Strömungsmechanik und Technische Akustik, Technische Universität Berlin, 2015. arXiv:1502.03701 [physics.flu-dyn].
- [36] D. C. Hill. A theoretical approach for analyzing the restabilization of wakes. *NASA STI/Recon Technical Report N*, 92:1 – 10, April 1992.
- [37] Charles Hirsch. *Numerical Computation of internal and external flows: Fundamentals of Numerical Discretization*, volume 1. John Wiley & Sons, 1988.
- [38] Charles Hirsch. *Numerical Computation of internal and external flows: Computational Methods for Inviscid and Viscous Flows*, volume 2. John Wiley & Sons, 1990.
- [39] A. Jameson. Aerodynamic design via control theory. *Journal of Scientific Computing*, 3:233–260, 1988.
- [40] Antony Jameson. The construction of discretely conservative finite volume schemes that also globally conserve energy or entropy. *Journal of Scientific Computing*, 34(2):152–187, 2008.

- [41] Antony Jameson. Formulation of kinetic energy preserving conservative schemes for gas dynamics and direct numerical simulation of one-dimensional viscous compressible flow in a shock tube using entropy and kinetic energy preserving schemes. *Journal of Scientific Computing*, 34(2):188–208, 2008.
- [42] Antony Jameson, Wolfgang Schmidt, Eli Turkel, et al. Numerical solutions of the euler equations by finite volume methods using runge-kutta time-stepping schemes. *AIAA paper*, 1259:1981, 1981.
- [43] CW Mastin Joe Thompson, Z Warsi. *Numerical Grid Generation*. Elsevier, Amsterdam, 1985.
- [44] WP Jones and BE Launder. The prediction of laminarization with a two-equation model of turbulence. *International journal of heat and mass transfer*, 15(2):301–314, 1972.
- [45] M. Klein, A. Sadiki, and J. Janicka. A digital filter based generation of inflow data for spatially developing direct numerical or large eddy simulations. *Journal of Computational Physics*, 186:652 – 665, 2003.
- [46] JC Kok. A symmetry and dispersion-relation preserving high-order scheme for aeroacoustics and aerodynamics. European Conference on Computational Fluid Dynamics ECCOMAS CFD 2006, 2006.
- [47] JC Kok. A high-order low-dispersion symmetry-preserving finite-volume method for compressible flow on curvilinear grids. *Journal of Computational Physics*, 228(18):6811 – 6832, 2009.
- [48] Maher Lagha, John Kim, JD Eldredge, and Xiaolin Zhong. A numerical study of compressible turbulent boundary layers. *Physics of Fluids*, 23(1):015106, 2011.
- [49] Peter D. Lax and Xu-Dong Liu. Solution of two-dimensional riemann problems of gas dynamics by positive schemes. *SIAM J. Sci. Comput.*, 19(2):319–340, March 1998.
- [50] BHK Lee. Self-sustained shock oscillations on airfoils at transonic speeds. *Progress in Aerospace Sciences*, 37(2):147–196, 2001.
- [51] R. B. Lehoucq. *Analysis and Implementation of an Implicitly Restarted Arnoldi Iteration*. PhD thesis, Rice University, Houston, 1995.

- [52] Mathias Lemke, Jan Schulze, and Joern Sesterhenn. Adjoint-based reconstruction of an entropy source by discrete temperature measurements. *Int. J. Computational Science and Engineering*, 9(5/6):526–537, 2014.
- [53] Lionel L Levy Jr. Experimental and computational steady and unsteady transonic flows about a thick airfoil. *AIAA Journal*, 16(6):564–572, 1978.
- [54] Hans Wolfgang Liepmann. The interaction between boundary layer and shock waves in transonic flow. *Journal of the Aeronautical Sciences (Institute of the Aeronautical Sciences)*, 13(12), 2012.
- [55] Thomas S Lund, Xiaohua Wu, and Kyle D Squires. Generation of turbulent inflow data for spatially-developing boundary layer simulations. *Journal of Computational Physics*, 140(2):233–258, 1998.
- [56] Christoph Mack. *Global stability of compressible flow about a swept parabolic body*. PhD thesis, Ecole Doctorale de L’Ecole Polytechnique, 2009.
- [57] Christoph J Mack and Peter J Schmid. A preconditioned krylov technique for global hydrodynamic stability analysis of large-scale compressible flows. *Journal of Computational Physics*, 229(3):541–560, 2010.
- [58] Christoph J Mack and Peter J Schmid. Global stability of swept flow around a parabolic body: features of the global spectrum. *Journal of Fluid Mechanics*, 669:375–396, 2011.
- [59] Christoph J Mack, Peter J Schmid, and Joern L Sesterhenn. Global stability of swept flow around a parabolic body: connecting attachment-line and crossflow modes. *Journal of Fluid Mechanics*, 611:205–214, 2008.
- [60] O. Marquet, D. Sipp, and L. Jacquin. Sensitivity analysis and passive control of cylinder flow. *Journal of Fluid Mechanics*, 615:221ff, November 2008.
- [61] M Pino Martin. DNS of hypersonic turbulent boundary layers. *AIAA paper*, 2337:2004, 2004.

-
- [62] Y. Morinishi. Forms of convection and quadratic conservative finite difference schemes for low mach number compressible flow simulations. *Trans. Jap. Soc. Mech. Engin. B*, pages 451–458, 2007.
- [63] Y. Morinishi. Skew-symmetric form of convective terms and fully conservative finite difference schemes for variable density low-mach number flows. *JCP*, 229(2):276–300, 2010.
- [64] Y. Morinishi and Kazuki Koga. Skew-symmetric convection form and secondary conservative finite difference methods for moving grids. *Journal of Computational Physics*, 257, Part B(0):1081 – 1112, 2014. Physics-compatible numerical methods.
- [65] Y. Morinishi, T.S. Lund, O.V. Vasilyev, and P. Moin. Fully conservative higher order finite difference schemes for incompressible flow. *Journal of Computational Physics*, 143(1):90 – 124, 1998.
- [66] Y. Morinishi, O. V. Vasilyev, and T. Ogi. Fully conservative finite difference scheme in cylindrical coordinates for incompressible flow simulations. *Journal of Comp. Phys.*, 197(2):686 – 710, 2004.
- [67] Mark V Morkovin. Effects of compressibility on turbulent flows. *Mécanique de la Turbulence*, pages 367–380, 1962.
- [68] ARG Mundell and DG Mabey. Pressure fluctuations caused by transonic shock/boundary-layer interaction. *Aeronautical Journal*, 90(897):274–282, 1986.
- [69] Siva Nadarajah and Antony Jameson. A comparison of the continuous and discrete adjoint approach to automatic aerodynamic optimization. *AIAA paper*, 667:1–20, 2000.
- [70] S Piponniau, JP Dussauge, JF Debieve, and P Dupont. A simple model for low-frequency unsteadiness in shock-induced separation. *Journal of Fluid Mechanics*, 629:87–108, 2009.
- [71] S. Pirozzoli, J. Larsson, J.W. Nichols, M. Bernardini, B.E. Morgan, and S.K. Lele. Analysis of unsteady effects in shock/boundary layer interactions. In *Proceedings of the Summer Program*, pages 153–164, 2010.

- [72] Sergio Pirozzoli. Generalized conservative approximations of split convective derivative operators. *Journal of Computational Physics*, 229(19):7180–7190, 2010.
- [73] Sergio Pirozzoli. Stabilized non-dissipative approximations of euler equations in generalized curvilinear coordinates. *Journal of Computational Physics*, 230(8):2997 – 3014, 2011.
- [74] Sergio Pirozzoli and Matteo Bernardini. Turbulence in supersonic boundary layers at moderate reynolds number. *Journal of Fluid Mechanics*, 688:120, 2011.
- [75] Sergio Pirozzoli, Matteo Bernardini, and Francesco Grasso. Characterization of coherent vortical structures in a supersonic turbulent boundary layer. *Journal of Fluid Mechanics*, 613:205, 2008.
- [76] Sergio Pirozzoli, Matteo Bernardini, and Francesco Grasso. Direct numerical simulation of transonic shock/boundary layer interaction under conditions of incipient separation. *Journal of Fluid Mechanics*, 657:361–393, 7 2010.
- [77] Sergio Pirozzoli and Francesco Grasso. Direct numerical simulation of impinging shock wave/turbulent boundary layer interaction at $Ma=2.25$. *Physics of Fluids (1994-present)*, 18(6):-, 2006.
- [78] Kenneth J Plotkin. Shock wave oscillation driven by turbulent boundary-layer fluctuations. *AIAA Journal*, 13(8):1036–1040, 1975.
- [79] T.J. Poinso and S.K. Lele. Boundary conditions for direct simulations of compressible viscous flows. *Journal Computational Physics*, 101:104–129, 1992.
- [80] Stephen B Pope. *Turbulent flows*. Cambridge university press, 2000.
- [81] J. Reiss and J. Sesterhenn. Fully conservative, skew symmetric and compact finite difference schemes. *AIP Conference Proceedings*, 1168(1):290–292, 2009.
- [82] Julius Reiss and Jörn Sesterhenn. A conservative, skew-symmetric finite difference scheme for the compressible navier–stokes equations. *Computers & Fluids*, 101(0):208 – 219, 2014. see also [arXiv:1308.6672].

-
- [83] WC Reynolds and AKMF Hussain. The mechanics of an organized wave in turbulent shear flow. part 3. theoretical models and comparisons with experiments. *Journal of Fluid Mechanics*, 54(02):263–288, 1972.
- [84] Matthew J Ringuette, Minwei Wu, and M Martin. Coherent structures in direct numerical simulation of turbulent boundary layers at mach 3. *Journal of Fluid Mechanics*, 594:59–69, 2008.
- [85] JC Robinet. Bifurcations in shock-wave/laminar-boundary-layer interaction: global instability approach. *Journal of Fluid Mechanics*, 579:85–112, 2007.
- [86] Robert Sugden Rogallo. *Numerical experiments in homogeneous turbulence*, volume 81315. National Aeronautics and Space Administration, 1981.
- [87] C W Rowley. Model reduction for fluids, using balanced proper orthogonal decomposition. *Aerospace Engineering*, 15(3):997–1013, 2005.
- [88] Clarence W Rowley, Igor Mezić, Shervin Bagheri, Philipp Schlatter, and Dan S Henningson. Spectral analysis of nonlinear flows. *Journal of Fluid Mechanics*, 641:115–127, 2009.
- [89] W Rozema, JC Kok, RWCP Verstappen, and AEP Veldman. A symmetry-preserving discretisation and regularisation model for compressible flow with application to turbulent channel flow. *Journal of Turbulence*, 15(6):386–410, 2014.
- [90] Pierre Sagaut, Eric Garnier, Eric Tromeur, Lionel Larcheveque, and Emmanuel Labourasse. Turbulent inflow conditions for large-eddy-simulation of compressible wall-bounded flows. *AIAA journal*, 42(3):469–477, 2004.
- [91] Ravi Samtaney, DI Pullin, and Branko Kosović. Direct numerical simulation of decaying compressible turbulence and shocklet statistics. *Physics of Fluids*, 13:1415, 2001.
- [92] B. Sande. Energy-conserving runge–kutta methods for the incompressible navier–stokes equations. *Journal of Computational Physics*, 233(0):100 – 131, 2013.

- [93] ND Sandham, YF Yao, and AA Lawal. Large-eddy simulation of transonic turbulent flow over a bump. *International Journal of Heat and Fluid Flow*, 24(4):584–595, 2003.
- [94] Philipp Schlatter and Ramis Örlü. Assessment of direct numerical simulation data of turbulent boundary layers. *Journal of Fluid Mechanics*, 659:116–126, 9 2010.
- [95] Philipp Schlatter and Ramis Örlü. Quantifying the interaction between large and small scales in wall-bounded turbulent flows: A note of caution. *Physics of Fluids (1994-present)*, 22(5):-, 2010.
- [96] Philipp Schlatter and Ramis Örlü. Turbulent boundary layers at moderate reynolds numbers: inflow length and tripping effects. *Journal of Fluid Mechanics*, 710:5–34, 11 2012.
- [97] Hermann Schlichting. *Grenzschicht-Theorie*. Verlag G. Braun, Karlsruhe, 1982.
- [98] Peter J Schmid. Dynamic mode decomposition of numerical and experimental data. *Journal of Fluid Mechanics*, 656:5–28, 2010.
- [99] Peter J Schmid and Luca Brandt. Analysis of fluid systems: Stability, receptivity, sensitivity lecture notes from the flow-nordita summer school on advanced instability methods for complex flows, stockholm, sweden, 2013. *Applied Mechanics Reviews*, 66(2):024803, 2014.
- [100] PJ Schmid, L Li, MP Juniper, and O Pust. Applications of the dynamic mode decomposition. *Theoretical and Computational Fluid Dynamics*, 25(1-4):249–259, 2011.
- [101] W Schröder, M Meinke, R Ewert, and WA El-Askary. LES of a turbulent flow around a sharp trailing edge. In *Direct and large-eddy simulation IV*, pages 353–362. Springer, 2001.
- [102] J. Schulze, P. Schmid, and J. Sesterhenn. Iterative optimization based on an objective functional in frequency-space with application to jet-noise cancellation. *Journal of Computational Physics*, 230(15):6075 – 6098, 2011.
- [103] J. Schulze and J. Sesterhenn. Optimal distribution of porous media to reduce trailing edge noise. *Computers & Fluids*, 78(0):41 – 53, 2013. LES of turbulence aeroacoustics and combustion.

-
- [104] J. C. Schulze, P. J. Schmid, and J. L. Sesterhenn. Exponential time integration using krylov subspaces. *International Journal for Numerical Methods in Fluids*, 60(6):591–609, 2009.
- [105] Jan Schulze. *Adjoint based jet-noise minimization*. PhD thesis, Technische Universitaet Berlin, 2013.
- [106] AJ Smits, N Matheson, and PN Joubert. Low-reynolds-number turbulent boundary layers in zero and favorable pressure gradients. *Journal of ship research*, 27(3):147–157, 1983.
- [107] D. C. Sorensen. Newton’s method with a model trust region modification. *SIAM Journal on Numerical Analysis*, 19:409–426, April 1982.
- [108] S Stolz and NA Adams. Large-eddy simulation of high-reynolds-number supersonic boundary layers using the approximate deconvolution model and a rescaling and recycling technique. *Physics of fluids*, 15:2398, 2003.
- [109] Bo Strand. Summation by parts for finite difference approximations for d/dx . *Journal of Computational Physics*, 110(1):47 – 67, 1994.
- [110] Pramod K. Subbareddy and Graham V. Candler. A fully discrete, kinetic energy consistent finite-volume scheme for compressible flows. *Journal of Computational Physics*, 228(5):1347 – 1364, 2009.
- [111] E. Tadmor. Skew-self adjoint form for systems of conservation laws. *J. Math. Ana. Appl.*, 103:428, 1984.
- [112] Christopher K.W. Tam and Jay C. Webb. Dispersion-relation-preserving finite difference schemes for computational acoustics. *Journal of Computational Physics*, 107(2):262 – 281, 1993.
- [113] Vassilios Theofilis. Global linear instability. *Annual Review of Fluid Mechanics*, 43:319–352, 2011.
- [114] Gilles Tissot, Laurent Cordier, Nicolas Benard, and Bernd R Noack. Model reduction using dynamic mode decomposition. *Comptes Rendus Mécanique*, 342(6):410–416, 2014.
- [115] Emile Toubert and Neil D Sandham. Large-eddy simulation of low-frequency unsteadiness in a turbulent shock-induced separation bubble. *Theoretical and Computational Fluid Dynamics*, 23(2):79–107, 2009.

- [116] Emile Touber and Neil D Sandham. Low-order stochastic modelling of low-frequency motions in reflected shock-wave/boundary-layer interactions. *Journal of Fluid Mechanics*, 671:417–465, 2011.
- [117] F.X. Trias, O. Lehmkuhl, A. Oliva, C.D. Pérez-Segarra, and R.W.C.P. Verstappen. Symmetry-preserving discretization of navier–stokes equations on collocated unstructured grids. *Journal of Computational Physics*, 258(0):246 – 267, 2014.
- [118] ER Van Driest. On turbulent flow near a wall. *J. Aerospace Sci.*, 23:1007–1011, 1956.
- [119] ER Van Driest. Turbulent boundary layer in compressible fluids. *Journal of spacecraft and rockets*, 40(6):1012–1028, 2003.
- [120] RWCP Verstappen and A. E. P. Veldman. Symmetry-preserving discretization of turbulent flow. *JCP*, 187(1):343, 2003.
- [121] J Wang, L-P Wang, Z Xiao, Y Shi, and S Chen. A hybrid numerical simulation of isotropic compressible turbulence. *Journal of Computational Physics*, 229(13):5257–5279, 2010.
- [122] Frank M White and Isla Corfield. *Viscous fluid flow*, volume 3. McGraw-Hill New York, 2006.
- [123] Christian Wollblad, Lars Davidson, and Lars-Erik Eriksson. Large eddy simulation of transonic flow with shock wave/turbulent boundary layer interaction. *AIAA journal*, 44(10):2340–2353, 2006.
- [124] Christian Wollblad, Lars Davidson, and Lars-Erik Eriksson. Investigation of large scale shock movement in transonic flow. *International Journal of Heat and Fluid Flow*, 31(4):528–535, 2010.
- [125] Minwei Wu and M Pino Martin. Direct numerical simulation of supersonic turbulent boundary layer over a compression ramp. *AIAA journal*, 45(4):879–889, 2007.
- [126] Zheng-Tong Xie and Ian P Castro. Efficient generation of inflow conditions for large eddy simulation of street-scale flows. *Flow, turbulence and combustion*, 81(3):449–470, 2008.

- [127] Sheng Xu and M Pino Martin. Assessment of inflow boundary conditions for compressible turbulent boundary layers. *Physics of Fluids (1994-present)*, 16(7):2623–2639, 2004.